

# Computational study of perovskite redox materials for solar thermal ammonia synthesis

**Author:**

Si, Qianli

**Publication Date:**

2021

**DOI:**

<https://doi.org/10.26190/unsworks/23888>

**License:**

<https://creativecommons.org/licenses/by/4.0/>

Link to license to see what you are allowed to do with this resource.

Downloaded from <http://hdl.handle.net/1959.4/100197> in <https://unsworks.unsw.edu.au> on 2024-03-28



**UNSW**  
THE UNIVERSITY OF NEW SOUTH WALES

The University of New South Wales

Faculty of Science

School of Materials Science and Engineering

**Computational study of perovskite redox materials  
for solar thermal ammonia synthesis**

Submitted in Fulfillment  
of the Requirements for  
the Degree of

*Master of Engineering*

Supervisor: Prof. Sean Li

Joint supervisor: Dr. Jack Yang

Name: Qianli Si

November 2021

## **Originality statement**

‘I hereby declare that this submission is my own work and to the best of my knowledge it contains no materials previously published or written by another person, or substantial proportions of material which have been accepted for the award of any other degree or diploma at UNSW or any other educational institution, except where due acknowledgement is made in the thesis. Any contribution made to the research by others, with whom I have worked at UNSW or elsewhere, is explicitly acknowledged in the thesis. I also declare that the intellectual content of this thesis is the product of my own work, except to the extent that assistance from others in the project’s design and conception or in style, presentation and linguistic expression is acknowledged.’

## **Copyright statement**

‘I hereby grant the University of New South Wales or its agents the right to archive and to make available my thesis or dissertation in whole or part in the University libraries in all forms of media, now or here after known, subject to the provisions of the Copyright Act 1968. I retain all proprietary rights, such as patent rights. I also retain the right to use in future works (such as articles or books) all or part of this thesis or dissertation. I also authorize University Microfilms to use the 350 words abstract of my thesis in Dissertation Abstract International (this is applicable to doctoral these only). I have either used no substantial portions of copyright material in my thesis or I have obtained permission to use copyright material; where permission has not been granted, I have applied/will apply for a partial restriction of the digital copy of my thesis or dissertation.’

## **Authenticity statement**

‘I certify that the library deposit digital copy is a direct equivalent of the final officially approved version of my thesis. No emendation of content has occurred and if there are any minor variations in formatting, they are the result of the conversion to digital format.’

## INCLUSION OF PUBLICATIONS STATEMENT

UNSW is supportive of candidates publishing their research results during their candidature as detailed in the UNSW Thesis Examination Procedure.

**Publications can be used in their thesis in lieu of a Chapter if:**

- The candidate contributed greater than 50% of the content in the publication and is the “primary author”, ie. the candidate was responsible primarily for the planning, execution and preparation of the work for publication
- The candidate has approval to include the publication in their thesis in lieu of a Chapter from their supervisor and Postgraduate Coordinator.
- The publication is not subject to any obligations or contractual agreements with a third party that would constrain its inclusion in the thesis

Please indicate whether this thesis contains published material or not:

- ☐ This thesis contains no publications, either published or submitted for publication  
*(if this box is checked, you may delete all the material on page 2)*
- ☒ Some of the work described in this thesis has been published and it has been documented in the relevant Chapters with acknowledgement  
*(if this box is checked, you may delete all the material on page 2)*
- ☐ This thesis has publications (either published or submitted for publication) incorporated into it in lieu of a chapter and the details are presented below

### CANDIDATE’S DECLARATION

I declare that:

- I have complied with the UNSW Thesis Examination Procedure
- where I have used a publication in lieu of a Chapter, the listed publication(s) below meet(s) the requirements to be included in the thesis.

Candidate’s Name	Signature	Date (dd/mm/yy)

## Acknowledgement

My master study started on Sep 2019 and will finish when I submit this thesis. Here, I would like to express my most heartfelt thanks to those who have helped and supported me in the past two years.

I would first like to thank my supervisor, Prof. Sean Li. Without his support, I would not finish this master study. Thanks for his guidance, encouragement, and valuable suggestions about my research.

I would like to thank my joint-supervisor, Dr. Jack Yang. With his guidance and training, I came into contact with computational materials science. Thanks for his patience and kindness.

Besides, I am appreciated about my group members, especially Jiaxin Fan and Qi Lei. Thanks for their help both in study and daily life. I will also thank my good friends Jayden Wang, Kobe Zhou, Ni Yang, Selvin Meng and Zane Sun who play very important roles during this 2-year exotic experience.

Last but not least, I want to thank my parents and girlfriend Doudou Wu. Without the supporting of my parents, I would not have the opportunity to study in UNSW, they always respect my decisions and support me unconditionally, thanks to their kindness and encouragement. Thanks for my girlfriend being the treasure of my life, I love you more than 3000 times.

Qianli

November 2021

## Abstract

Ammonia is one of the most important precursors used in chemical engineering to manufacture products that we use every day. However, to help tackle the deepening global energy crisis, it is important to find new, alternative methods for ammonia synthesis, particularly those that utilise renewable energies, to replace the century-old, energy-intensive Haber–Bosch ammonia synthesis process. Among the new approaches that have been studied, solar thermal ammonia synthesis (STAS), which uses solar energy, water, and redox materials to produce ammonia in a chemical-looping process, has attracted the attention of researchers as an economical and environmentally friendly process for the production of ammonia. However, finding the right redox materials that can efficiently catalyse the STAS reactions through trial-and-error experiments are extremely difficult and time-consuming. Recently, with the help of Density Functional Theory-based calculations and high-performance computers, high-throughput computational screening of promising redox materials for STAS has provided the community with an important tool to expedite the development of STAS technology. According to the literature, previous research has focused on binary redox materials – yet these compounds only occupy 10 % of the larger material space. As such, more complex materials are worthy of further study. In this thesis, we theoretically analysed the thermodynamics of perovskite oxide/oxy-nitride pairs and their potential as active materials for STAS.

First, we investigated the metal-alloyed perovskite redox materials for STAS. It is believed that metal intermixing alters the bonding states of the thermodynamically stable perovskite oxides. This can potentially activate a highly stable material for use as a thermal catalyst. Combining random structural sampling, high-throughput DFT calculations, and a machine-learning Gibbs free energy descriptor, we found that, compared to the pristine perovskite  $\text{SrTiO}_3/\text{YTiO}_3$ , A-site-alloyed perovskite  $\text{Sr}_{0.875}\text{Y}_{0.125}\text{TiO}_3/\text{Sr}_{0.875}\text{Y}_{0.125}\text{TiO}_{2.875}\text{N}_{0.125}$  is mostly activated via cooperative

enhancement; i.e., its limiting reaction energy is more negative than that of the pristine perovskite redox pairs. This insight may aid the future design of redox materials via compositional engineering.

Consequently, we found that perovskite oxynitrides are compounds that possess intriguing properties that are yet to be investigated, and we further proceeded to assess the thermodynamics of pristine perovskite oxide/oxynitride. The results show that lattice strains affect the formation enthalpies of perovskite oxides/oxynitrides. Complete relaxation, which has a greater influence on lattice strains, will make some of the perovskite oxynitrides reach the true local minimum. The formation enthalpies of some perovskite oxynitrides, mostly structures that contain transition metals as the A-site cation, will change accordingly. The electronic interaction between the nitrogen dopant and the B-site cation is one of the most important factors affecting the difference in the formation energies between the perovskite oxynitrides and their oxide counterparts.

This work establishes a thermodynamic database of 430 perovskite oxide/oxynitride pairs, which paves the way for further research on their potential as redox pairs for STAS. In the final part of this study, we calculated the Gibbs formation energies of these candidates at different reaction temperatures. This enabled us to perform further reaction thermodynamic analysis. We found that  $\text{BeTiO}_3/\text{BeTiO}_{2.875}\text{N}_{0.125}$  is the most promising redox pair for use in STAS. In addition, using this set of cubic perovskites, we benchmarked the accuracies of the Gibbs free energies calculated using the machine-learning descriptor against those obtained from quasiharmonic phonon calculations. Although many perovskite oxides are known to exhibit strong vibrational anharmonicity, our benchmark shows that, within the temperature range for thermal catalytic reactions, the free energies calculated using these two approaches agree well with each other.

The results from this research suggest that STAS using suitable redox materials has potential as a process for small-scale ammonia production. As such, the identification



of promising active materials for STAS will be the focus of future research. The methodology proposed in this work can also be used in the design of novel functional materials for energy storage and solid-state solar thermal chemical processes.

## Table of content

<b>Originality statement .....</b>	<b>I</b>
<b>Copyright statement .....</b>	<b>II</b>
<b>Authenticity statement.....</b>	<b>II</b>
<b>INCLUSION OF PUBLICATIONS STATEMENT.....</b>	<b>III</b>
<b>Acknowledgement .....</b>	<b>IV</b>
<b>Abstract.....</b>	<b>V</b>
<b>Chapter 1 Introduction .....</b>	<b>1</b>
<b>Chapter 2 Literature review .....</b>	<b>4</b>
<b>2.1 Introduction to perovskites .....</b>	<b>4</b>
<b>2.1.1 Structures and properties of perovskites.....</b>	<b>4</b>
<b>2.1.2 Application of perovskites.....</b>	<b>5</b>
<b>2.1.3 Introduction of several common perovskites .....</b>	<b>6</b>
<b>2.2 Ammonia synthesis .....</b>	<b>9</b>
<b>2.2.1 The traditional method of ammonia synthesis.....</b>	<b>9</b>
<b>2.2.2 Solar thermal ammonia synthesis.....</b>	<b>11</b>
<b>2.3 Gibbs free energy .....</b>	<b>16</b>
<b>2.3.1 The definition of Gibbs free energy.....</b>	<b>16</b>
<b>2.3.2 Features of the Gibbs free energy.....</b>	<b>16</b>
<b>2.3.3 The isothermal formula.....</b>	<b>17</b>
<b>2.4 Data science and machine learning .....</b>	<b>18</b>
<b>2.4.1 The relationship between data science and materials science .....</b>	<b>18</b>
<b>2.5 Physical descriptor for the Gibbs energy of inorganic crystalline solids.....</b>	<b>20</b>
<b>Chapter 3 Theoretical understanding of Density Functional Theory (DFT) .....</b>	<b>23</b>
<b>3.1 The Schrödinger equation.....</b>	<b>23</b>
<b>3.2 The Hohenberg–Kohn Theorems: Origin of DFT .....</b>	<b>24</b>
<b>3.3 The Kohn-Sham approach.....</b>	<b>25</b>
<b>3.4 The exchange-correlation functional.....</b>	<b>25</b>
<b>3.5 Application of DFT: Vienna Ab initio Simulation Package.....</b>	<b>27</b>

<b>Chapter 4 Can Metal Intermixing Cooperatively Improve Perovskites as Redox Materials for Thermochemical Ammonia Synthesis? A Case Study on (Sr,Y)(Ti,Ru)O<sub>3</sub></b>	<b>29</b>
4.1 Introduction	29
4.2 Methodologies	33
4.3 Results and Discussions	37
4.4 Conclusions	52
<b>Chapter 5 Reaction thermodynamic screening for the formation of perovskite oxynitrides</b>	<b>55</b>
5.1 Introduction	55
5.2 Methodologies	57
5.3 Results and discussion	59
5.4 Conclusion	68
<b>Chapter 6 High-throughput screening of perovskites as active materials for solar thermal ammonia synthesis</b>	<b>70</b>
6.1 Introduction	70
6.2 Methodologies	72
6.3 Results and discussions	74
6.4 Conclusion	85
<b>Chapter 7 Conclusion and Outlook</b>	<b>86</b>
7.1 Conclusions	86
7.2 Outlook	88
<b>Bibliography</b>	<b>91</b>

## Chapter 1 Introduction

Traditionally, materials discovery based on trial-and-error experiments are both time consuming and costly. With the development of the high-performance computations (HPC) clusters in recent years, computation and simulation have become pivotal methods to discover and investigate new functional materials. By using the computer-aided computational methods such as density functional theory (DFT), materials prediction and design can be conducted before they are synthesized and characterization. The most critical feat of HPC is large sets of candidate materials can be computationally screened in relatively short time, by high-throughput screening, several materials databases have been established like Materials Project which makes it possible for researchers to obtain the information of the structures they want to investigate accurately and effectively, from thermoelectric, photovoltaic to electrodes and other field, a large number of applications have benefited from these resources[1, 2].

As ammonia is an important chemical used to manufacture many products currently used in society, numerous approaches have been proposed to produce ammonia on a large scale. One of the most successful methods is the Haber–Bosch process. However, this process is energy-intensive and produces greenhouse gases, prompting a need for the development of alternative, environmentally and energy-friendly processes to produce ammonia. Moreover, some of the proposed methods that use renewable energy to produce ammonia, such as electrocatalysis and photocatalysis, suffer from low faradic efficiency, so are thus not ideal. This thesis focused on discovering promising active materials for solar thermal ammonia synthesis (STAS) that use a two- or three-step chemical-looping process by relying on first-principle calculations (DFT) and machine learning. Because perovskites ( $ABX_3$ ) are widely used in catalysis, and previous experimental research has found that  $Sr_{1-x}Y_xTi_{1-y}Ru_yO_{3-\delta}$  is a promising candidate for ammonia dehydrogenation because of its high activity and stability, they

may also be promising for ammonia synthesis. We thus implemented high-throughput screening to identify promising perovskite redox materials for chemical looping, which reduces the reaction barrier, improves the kinetics, and makes the processes happen spontaneously.

To provide further background to this study, explain the methodology of the research, and convey the results, this thesis is structured as follows:

**Chapter 2** surveys the literature related to the traditional Haber–Bosch process, followed by newly proposed methods for ammonia synthesis, including solar thermal processes. We discuss the problems with the experimental STAS approaches. Owing to the challenge of obtaining the temperature-dependent Gibbs formation energies of metal nitrides from experiments, DFT calculations are used. However, using the first-principle method to calculate the Gibbs formation energies requires a large amount of calculation resources. By using a machine-learning descriptor, one can calculate the temperature-dependent Gibbs formation energy quickly and accurately.

**Chapter 3** offers a brief introduction to DFT.

**Chapter 4** shows how we used random structural sampling, high-throughput DFT screening, and a machine-learning descriptor to investigate mixed-metal perovskite redox pairs for thermal ammonia synthesis. We assessed the feasibility of  $\text{Sr}_{1-x}\text{Y}_x\text{TiO}_3/\text{Sr}_{1-x}\text{Y}_x\text{TiO}_y\text{N}_{3-y}$ ,  $\text{Sr}_{1-x}\text{Y}_x\text{RuO}_3/\text{Sr}_{1-x}\text{Y}_x\text{Ru}_y\text{N}_{3-y}$ ,  $\text{SrTi}_{1-x}\text{Ru}_x\text{O}_3/\text{SrTi}_{1-x}\text{Ru}_x\text{O}_y\text{N}_{3-y}$ , and  $\text{YTi}_{1-x}\text{Ru}_x\text{O}_3/\text{YTi}_{1-x}\text{Ru}_x\text{O}_y\text{N}_{3-y}$  with respect to the pristine perovskite oxides/oxy-nitrides  $\text{SrTiO}_3/\text{SrTiO}_y\text{N}_{3-y}$ ,  $\text{SrRuO}_3/\text{SrRuO}_y\text{N}_{3-y}$ ,  $\text{YTiO}_3/\text{YTiO}_y\text{N}_{3-y}$ , and  $\text{YRuO}_3/\text{YRuO}_y\text{N}_{3-y}$ . One of the metal-alloyed perovskite redox pairs –  $\text{Sr}_{0.875}\text{Y}_{0.125}\text{TiO}_3/\text{Sr}_{0.875}\text{Y}_{0.125}\text{TiO}_{2.875}\text{N}_{0.125}$  – shows a cooperative enhancement to their pristine perovskites, thus demonstrating that metal-alloyed perovskite is a promising active material for STAS. These results pave the way for future designs of novel functional materials with complex compositions.

**Chapter 5** focuses on the thermodynamics of perovskites. As the results of Chapter 4 show, we found that a partial conversion of oxide to oxynitride rather than nitride is preferred for perovskites, which inspired us to further examine the thermodynamics of a large set of perovskite oxides and oxynitrides. Two different structural optimisations were applied, which led to different lattice strains in the structure. The full optimisation resulted in a larger lattice strain in the structures, which made some of the perovskite oxynitrides reach the true local minimum state. In other words, the perovskite oxynitrides possess more negative formation enthalpies than their corresponding perovskite with larger lattice strains. We explored the reasons why some perovskite oxynitrides can be thermodynamically more stable than their parent oxides. We demonstrated that perovskite oxynitrides with transition metals as A-sites are likely to be more stable than their corresponding perovskite oxides compared to other types of perovskite oxynitrides, and the formation enthalpy difference is mainly influenced by the interaction between the N atom and the B-site atom.

**Chapter 6** describes the high-throughput screening of the perovskite oxides/oxynitrides evaluated in Chapter 5 as potential redox materials for STAS. We systematically analysed the thermodynamic performance of 430 redox pairs for STAS and found that one of the 430 perovskite redox pairs,  $\text{BeTiO}_3/\text{BeTiO}_{2.875}\text{N}_{0.125}$ , is a promising active material for STAS. In addition, by comparing the Gibbs free energy calculated by the machine-learning descriptor with phonon-based quasiharmonic approximation (GHA), we concluded that the descriptor is reliable for calculating the Gibbs formation energies of perovskites.

## Chapter 2 Literature review

### 2.1 Introduction to perovskites

#### 2.1.1 Structures and properties of perovskites

Perovskite is a general term for a class of crystalline materials with the same crystal structure as  $\text{CaTiO}_3$  (i.e.,  $\text{ABX}_3$  as the general chemical formula)[3]. A is a metal ion with a large ion radius ( $> 0.09\text{nm}$ ), usually alkali metals, alkaline earth metals, and lanthanides which coordinates with 12 surrounding oxygen atoms to form a close-packed cubic structure, the A ions and oxygen ions form the face-centred cubic structure, A ions are located at the apex angle of the cube, and oxygen ions are located at the six face centres of the cube. B is usually a transition metal with a small ion radius ( $> 0.05\text{nm}$ ). It coordinates with six neighbouring oxygen ions and occupies the centre of the octahedron in the cubic perovskite[4]. Owing to the variability of B-ions valence, it is usually the main component that determines the physical properties of the perovskite material. For the  $\text{ABO}_3$  perovskites, B ions fill only 1/4 of the octahedral interstices,  $[\text{BO}_6]$  octahedral groups are connected to each other by vertices, and A ions are located in the gaps of the  $[\text{BO}_6]$  octahedral groups, as shown in Fig. 2.1.

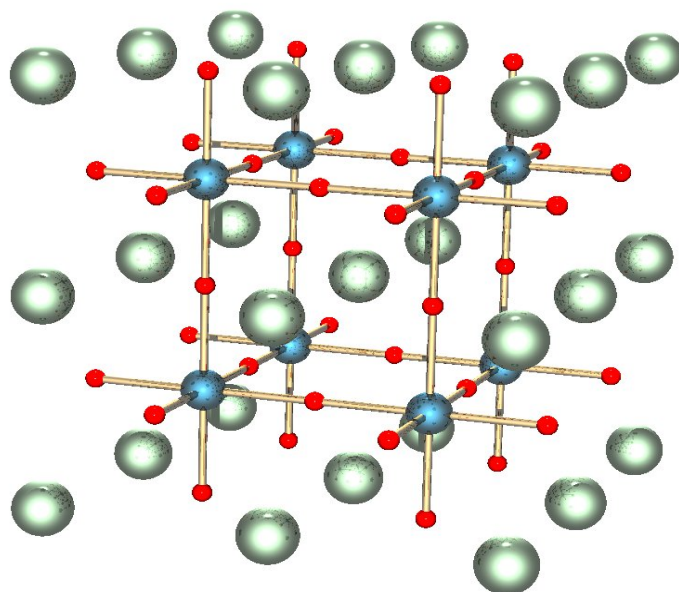


Fig. 2.1. The structure of  $ABO_3$  perovskite.

Theoretically the radius of the three ions should follow the following relationship in order to adopt a perfect close-packed cubic crystal structure:

$$\sqrt{2}[(R_A) + (R_O)] = 2[(R_B) + (R_O)] \quad (2.1)$$

However, in reality, not all combinations of ions from the periodic table can satisfy this relationship, so a tolerance factor called Goldschmidt's tolerance factor  $t$  is introduced[5], which provides a geometric measurement to assess if a given set of three atoms may form a stable cubic perovskite structure. It can be described as follows:

$$t = \frac{[(R_A) + (R_O)]}{\sqrt{2}[(R_B) + (R_O)]} \quad (2.2)$$

When  $t > 1$ , the structure is hexagonal or tetragonal, because the A ion is too big or the B ion is too small. If  $0.9 < t < 1$ , then the structure is cubic because the A ion and B ion are ideal sizes. When  $0.71 < t < 0.9$ , the structure is orthorhombic or rhombohedral, as the A ion is too small to fit into the B interstices. When  $t < 0.71$ , it means that the A ion and B ion have the same radii, which generates different structures.

Perovskites have some unique properties and can be used as superconducting materials, ferromagnets, ferroelectrics, piezoelectric ceramics, thermistors, oxygen electrodes, and catalysts.

### 2.1.2 Application of perovskites

Properties such as superconductivity, magnetoresistance, ionic conductivity and dielectric properties[6] make it possible for perovskites to be used in microelectronics



and telecommunications. Perovskites with a large light yield in radiation conversion can also be used to produce scintillators[7].

In 2008, scientists successfully used perovskite  $\text{LaAlO}_3$  doped with neodymium to generate laser light [8]. Because of their high photoluminescence quantum efficiencies, perovskites are also promising for use in light-emitting diodes[9]. Additionally, perovskites can also be used in photoelectrolysis, researchers have used perovskite photovoltaic cells that are highly efficient but low-cost for water hydrolysis[10].

One of the most important applications of perovskites is in the field of solar fuel cells. Unlike normal solar cells, perovskite solar cells (PSCs) are compounds with a perovskite structure that use a hybrid organic-inorganic lead or tin halide-based material as the light-harvesting active layer, which has the advantages of conversion efficiency and a relatively simple manufacturing process. In addition, perovskites are widely used in catalysis. In the early 1970s, perovskites were reported to have catalytic oxidation activity. That discovery led to a global increase in related research. Previous studies have shown that perovskites containing cobalt or manganese have good catalytic activity for the combustion of carbon monoxide, methane, hydrogen and hydrocarbons[11]. Perovskites have also been demonstrated to be excellent catalysts in oxidative dehydrogenation, the partial oxidation of hydrocarbons. By controlling the activity of the catalyst through experimental methods, the hydrocarbons will not be completely oxidised to carbon dioxide and water, but oxygenated compounds are expected to be generated. Another application is photocatalytic water splitting. Researchers found that, under light, strontium titanate ( $\text{SrTiO}_3$ ) can decompose water into hydrogen and oxygen, and if nickel was loaded on STO, it could help electron migration and improve the production of hydrogen. Perovskites are thus potential catalysts in many research fields, and scientists are constantly working to make perovskite catalysts widely available in practical applications.

### **2.1.3 Introduction of several common perovskites**

## 1. Strontium titanate

$\text{SrTiO}_3$  is an oxide formed by strontium and titanate. At room temperature, it is a material with a perovskite structure.  $\text{SrTiO}_3$  has a very large dielectric constant ferroelectric phase transition at low temperatures. As a result of quantum fluctuations, it remains paraelectric until the lowest temperature is measured, which makes it quantum paraelectric[12].  $\text{SrTiO}_3$  is a widely used electronic functional ceramic material in the electronics, machinery, and ceramic industries. It has the advantages of a high dielectric constant, low dielectric loss, and good thermal stability.  $\text{SrTiO}_3$  is the first perovskite oxide and insulator that was discovered to have superconducting properties when the temperature is below 0.35K at high electron densities[13]. Some high-temperature superconductors and oxide-based thin films always use  $\text{SrTiO}_3$  as the substrate for epitaxial growth, and one of the most well-known applications is the use of the material as the substrate upon which the lanthanum aluminate–strontium titanate interface can grow.  $\text{SrTiO}_3$  is also used as a substrate for the growth of other oxides such as lanthanum aluminate ( $\text{LaAlO}_3$ ) and strontium ruthenate ( $\text{SrRuO}_3$ ). Furthermore,  $\text{SrTiO}_3$  has a high band gap (3.2 eV), excellent photocatalytic activity, unique electromagnetic properties, and redox catalytic activity. These properties allow for strontium titanate to be widely used in the field of photocatalysis, such as in the photocatalytic decomposition of water to produce hydrogen, the photocatalytic degradation of organic pollutants, and photochemical batteries.

## 2. Strontium ruthenate

$\text{SrRuO}_3$ , a complex perovskite composed of strontium and ruthenium, has been studied by scientists for many years. Surprisingly, it exhibits itinerant ferromagnetism, which was researched by Randall and Ward[14].  $\text{SrRuO}_3$  also has special transport properties: when the temperature is lower than 25 K, SRO is a Fermi liquid[15] but shows poor metal behaviour when the temperature is high[16].  $\text{SrRuO}_3$  can also be used to form unlimited layers, expressed as  $\text{Sr}_{n+1}\text{Ru}_n\text{O}_{3n+1}$ .  $\text{Sr}_2\text{RuO}_4$  is an important compound in this

series, which was the first discovered perovskite superconductor with copper[17]. Normally, researchers use bulk single crystals to perform physical studies, but because thin films of  $\text{SrRuO}_3$  are used, the physical properties, of this perovskite are studied using such films on appropriate substrates. These films are also used as the conducting layer of epitaxial multilayered complex oxides, especially as electrodes in oxide electronics, which is an application that has aroused extensive research interest. The transport and magnetic properties of thin films of  $\text{SrRuO}_3$  are very sensitive to the surface morphology, temperature, film thickness, and disorder in the film and substrate-induced strain. The properties of these films have not been thoroughly studied, thus offering an attractive avenue for future research.

### **3. Barium titanate**

Barium titanate ( $\text{BaTiO}_3$ ) is a strong dielectric material with a high dielectric constant and low dielectric loss, which is why it is one of the most widely used materials in electronic ceramics—it is even known as “the pillar” of the electronic ceramic industry.  $\text{BaTiO}_3$  is a uniform molten compound with a melting point of 1891.150 K. Below this temperature,  $\text{BaTiO}_3$  crystallises, and up to 1733.150 K, it belongs to the non-ferroelectric hexagonal 6/mmm point group. When the temperature is between 403.150 K and 1733.150 K, however, it transforms into a cubic perovskite structure that is highly symmetrical and not ferroelectric or piezoelectric. As the temperature continues to decrease to 278.150 K, between 278.150 K and 403.150 K, the structure is a 4mm point group of the tetragonal system, with remarkable ferroelectricity. When the temperature falls below 278.150 K, the structure is an orthogonal system mm2 point group. Below 183.150 K, the structure transforms from an orthogonal system to a rhombohedral 3m point group, and the structure still has a ferroelectric[18]. In general,  $\text{BaTiO}_3$  has five crystal structures; as the temperature decreases, the symmetry of the crystal decreases. Because of its high dielectric constant,  $\text{BaTiO}_3$  is used to produce capacitors. Polycrystalline  $\text{BaTiO}_3$  has a positive temperature coefficient of resistance, which makes it usable in thermistors and self-regulating electric heating systems. It is

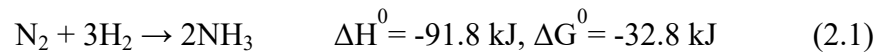
also used in microphones and transducers because it is a piezoelectric material. Moreover, high-purity BaTiO<sub>3</sub> powder is a significant element in new BaTiO<sub>3</sub> energy storage systems for electric cars.

## 2.2 Ammonia synthesis

### 2.2.1 The traditional method of ammonia synthesis

Ammonia (NH<sub>3</sub>) is an important industrial chemical that has been used for hydrogen storage, fertiliser production, and explosives. Currently, the Haber–Bosch process is widely used in its industrial production [19].

The reaction is:



In this process, H<sub>2</sub> (hydrogen) and N<sub>2</sub> (nitrogen) are dissociated as N- and H-atoms through a catalytic reaction relying upon the dissociative mechanism. The basic steps are as follows:



Generally, the reaction with a catalyst occurs under harsh conditions: at 300bar and 400-500 °C[20]. According to Equation (2.1), the whole process is an exothermic reaction. While an exothermic reaction can theoretically occur spontaneously, this process remains highly energy-intensive for the need to activate the reactants to overcome the large reaction energy barrier; nearly 1–2 % of the global energy produced every year is consumed during this process [21]. The major fraction of the consumed energy is used to produce two elemental precursors. For instance, H<sub>2</sub> is produced by the steam reforming of natural gas, and N<sub>2</sub> is cryogenically separated from the air [22]. For this reaction to happen, the most difficult step is to dissociate the strong triple bond between two nitrogen atoms, which has a bond strength of approximately 941 kJ/mol. Therefore, it is very difficult to conduct the  $N_2^* \rightarrow 2N^*$  step because the free energy change of this step is high[23]. As such, efficient catalysts are those that can absorb nitrogen and lower the reaction barrier. Fe catalysts have been widely used in the Haber-Bosch process owing to their low cost and effectiveness[24]. However, alternative methods that can produce ammonia under ambient conditions are still urgently required. Even with catalysts, the yield of NH<sub>3</sub> is still low owing to the unfavourable thermodynamic equilibrium. At 300 bar, the yield of NH<sub>3</sub> initially does not exceed 25 %, thus the unreacted H-N mixture needs to be compressed and recycled. Approximately 4–6 kg of the reactant gases is needed to produce 1 kg of NH<sub>3</sub>.

The multi-step Haber–Bosch ammonia synthesis includes the following steps[25]:

- (a) prepare CO and H<sub>2</sub> by steam reforming CH<sub>4</sub> catalytically;
- (b) shift water gas to form more H<sub>2</sub> from CO and transfer CO into CO<sub>2</sub>;
- (c) remove CO<sub>2</sub>;
- (d) generate methane to remove remaining CO and CO<sub>2</sub> ;
- (e) depurate N<sub>2</sub> and H<sub>2</sub>;
- (f) produce NH<sub>3</sub> by the Haber-Bosch process; and
- (g) generate pure NH<sub>3</sub> by separating the unreacted H-N mixture by refrigeration..

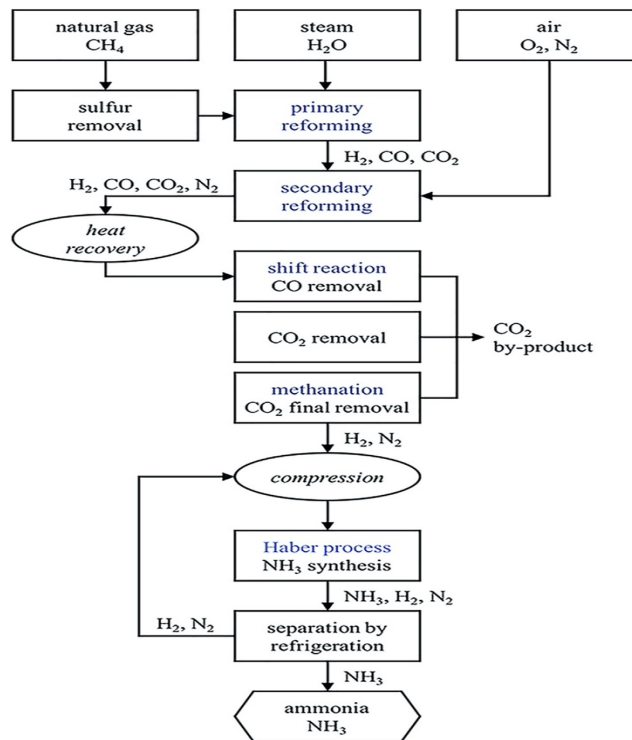


Fig. 2.2 Flow chart of the multi-step ammonia synthesis.

All of the processes discussed above require a large amount of energy that is generated by a high-temperature process using heat or electricity, which always also generates pollution[26]. Therefore, it is highly desirable to develop new ammonia synthesis techniques that will allow this process to happen under normal temperature and pressure, but researchers have not found any catalysts that provide rational reaction rates under such conditions, as demonstrated by the ratio of the activation energy for N<sub>2</sub> dissociation and the adsorption energy of nitrogen at the catalyst surface[27-29]. As such, developing catalysts that can make the ammonia synthesis process occur at a low pressure and temperature is eagerly awaited [30].

### 2.2.2 Solar thermal ammonia synthesis

STAS is one such alternative method, inspired by solar thermochemical water splitting (STWS), which uses solar energy to generate H<sub>2</sub> at high temperatures (> 1500 K ) and atmospheric pressure[31]. In the STWS method, metal oxides (MO) are replaced by non-reactive materials with good properties for exchanging oxygen, for example,

ceria[32], perovskites[33], or hercynite[34], in a chemical looping process. Similarly, STAS methods, which can generate ammonia from water and a reducing agent by using thermochemical redox cycles, have been proposed.

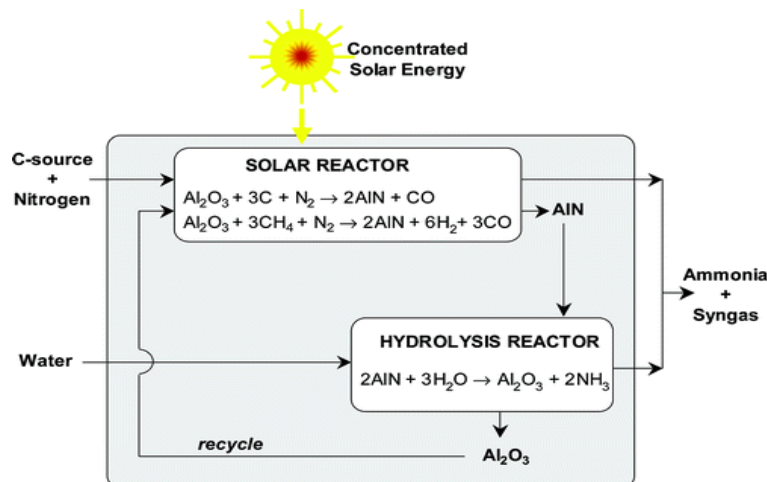


Fig. 2.3 Flow chart of solar thermochemical ammonia synthesis by  $\text{Al}_2\text{O}_3/\text{AlN}$ . (Figure reproduced from ref[26]. )

The first MN/MO redox pair used in STAS was  $\text{Al}_2\text{O}_3/\text{AlN}$ , proposed by Ga'lvez *et al.* in 2007[35]. In this method, the first step is to reduce  $\text{Al}_2\text{O}_3$  by a carbothermal reducing agent to form AlN in a nitrogen atmosphere. This step is endothermic and must be performed at 1500 °C. Then, AlN reacts with water vapour to generate ammonia and  $\text{Al}_2\text{O}_3$ , which is an exothermic steam-hydrolysis step. The reaction is thus completed in two steps. A flowchart of this method is provided in Fig. 2.3. Carbon is used because is it preferable to use a gaseous reducing agent in the thermochemical looping process as solid reducing agents should be mixed with active materials, thus wasting resources. When hydrogen, carbon monoxide, and methane are used as gaseous reducing agents, they have similar reducing powers and analogous reducing thermodynamics; however, carbon-based reducing agents have the disadvantage of bringing carbon into the active materials and thus may generate the greenhouse gas  $\text{CO}_2$ . Another method to generate  $\text{NH}_3$  using the redox pair  $\text{Gr}_2\text{O}_3/\text{Gr}_2\text{N}$ ,  $\text{H}_2$ , and  $\text{CO}$  as reducing agents was proposed in 2011 by Michalsky *et al.*[36] , which also generates  $\text{CO}_2$  during the cycle process.

In 2017, Heidlage *et al.* published a paper that introduced another redox pair as an active material that can satisfy the STAS process [37]. The first step is to produce  $\text{Mn}_5\text{N}_2$  with metal Mn and  $\text{N}_2$  in the atmosphere, and the second step is the hydrolysis of metal nitride using the generated  $\text{Mn}_5\text{N}_2$  to react with  $\text{H}_2\text{O}$ , which produces  $\text{MnO}$ ,  $\text{NH}_3$ , and  $\text{H}_2$ . The final step is to reduce  $\text{MnO}$  with  $\text{CH}_4$  as a reducing agent to generate Mn, CO, and  $\text{H}_2$ , which can be used to repeat the first step in this cycle (Fig. 2.4). During the reaction, ammonia, hydrogen, and carbon monoxide syngas are generated, which can be used for Fischer–Tropsch process and methanol synthesis. In the  $\text{NH}_3$  generation step, the output of  $\text{NH}_3$  generated from the metal nitride by steam corrosion at 500 °C and atmospheric pressure is 0.04. If NaOH is mixed with the metal nitride in a 1:1 molar ratio, the yield of  $\text{NH}_3$  will increase to 0.54 under the same conditions. The thermochemical process improves the  $\text{NH}_3$  output by nearly  $9.1 \text{ GJ t}^{-1} \text{ NH}_3$  compared to the conventional Haber–Bosch process because of the syngas coproduct, rather than transferring natural gas to  $\text{CO}_2$ , which is environmentally friendly.

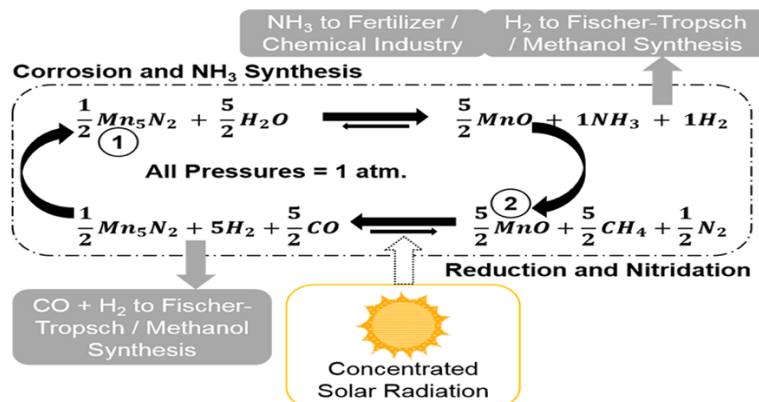


Fig. 2.4. Flow diagram of  $\text{NH}_3$  and syngas generation by  $\text{Mn}_5\text{N}_2/\text{MnO}$  with concentrated solar radiation. (Figure reproduced from ref[37].)

The STAS process requires a phase change from MN to MO, thus differing from the STWS process, which partially reduces single active materials. In this phase change, the active material is the MN/MO redox pair, and the feasibility of one redox pair for STAS is closely related to its temperature-dependent thermodynamics. The appropriate



reactant material (metal M in metal nitride and metal oxide) should have the following characteristics[38]:

1. It should have medium to high nitridation and suitable kinetics.
2. It should be a metal nitride with acceptable kinetics that can generate medium to high yields of  $\text{NH}_3$ .
3. The reduction of metal oxide should occur near the best temperature for receiving solar energy in an industry-scale, solar-heated reactor[39].
4. The reactant should be regenerated by a gas agent that is sustainable and economic friendly.
5. It should decrease the reactant porosity or sophisticated gas phase separation without melting or boiling the reactant to avoid blocking the pipe.
6. The exothermic reactions that produce low to medium heat should occur at temperatures lower than those of the metal oxide reduction reaction.
7. The reactant should be non-toxic to people and the environment.
8. It should not require multi-step reactions.
9. It should entail few separation processes to avoid increasing the energy requirement.
10. A high amount of solar energy should be used in this process.

However, previous efforts to find suitable MN/MO redox pairs only assessed 35 pairs because the temperature-dependent formation free energy [ $\Delta G_f(T)$ ] of the metal nitride is experimentally difficult to determine. There is thus an urgent need to find a feasible method to measure the temperature-dependent Gibbs formation energies of redox materials.

### **2.2.3 High-throughput screening of active materials for STAS**

In recent years, HPC clusters have been rapidly developed. The use of computers has provided scientists greater opportunities to discover or create new materials. The advantages of computer-aided methods over experiments are that materials can be evaluated and tested before they are synthesised. For instance, a recent report by

Raccuglia *et al.* described the generation of organic–inorganic materials from failed experiments using machine learning [40]. The computer-aided method thus makes it possible to test thousands of materials through calculations and modelling instead of relying on experiments. Moreover, as computer science has developed, interdisciplinary computer science will become a trend in the future.

Scientists have also been working on combining STAS with computer calculations. In 2019, Bartel *et al.* proposed a creative method that analysed 1148 pairs of MN/MO redox materials for solar ammonia synthesis, regardless of whether MN/MO could be found or synthesised by experiments. In this method, a high-throughput thermodynamic screening of Gibbs formation energies –  $G_f(T)$  – of these 1148 MN/MO redox pairs at three different temperatures was conducted. The  $G_f(T)$  is calculated using a descriptor[41] and 0 K DFT formation energies, which can be sourced from an open material database, Materials Projects [42]. The descriptor can predict the  $\Delta G_f(T)$  of inorganic crystalline solids rapidly and accurately ( $\sim 50$  meV/atom) when  $\Delta H_f$  is known. Although the number of known standard-state formation enthalpies is still small, a large number of  $\Delta H_f$  calculated by DFT can be obtained from Materials Projects.

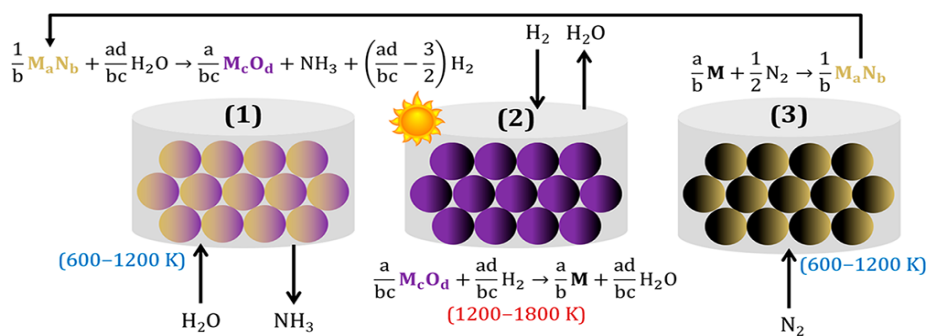


Fig. 2.5 Scheme of solar thermochemical ammonia synthesis. (1) Hydrolysis of metal nitride ( $M_aN_b$ ) produces  $NH_3$ ,  $H_2$ , and metal oxide ( $M_cO_d$ ); (2) reducing metal oxide to yield metal and water and (3) fixation of  $N_2$  to yield metal nitride. (Figure reproduced from ref.[43].)

These redox pairs are made from binary oxides and nitrides by evaluating their thermodynamic viability, and MN/MO redox pairs based on B, V, Fe, and Ce have the potential to be used in the STAS cycle reaction. Arguably, scientists are here provided

with the chance to determine the relevant reaction thermodynamics and materials challenges, and materials that have not been explored should perhaps be focused upon in future computational and experimental studies.

## **2.3 Gibbs free energy**

### **2.3.1 The definition of Gibbs free energy**

In thermodynamics, the Gibbs free energy is a thermodynamic potential that determines the reaction direction and material stability. Gibbs free energy is also called Gibbs energy, Gibbs function, or free enthalpy[44]. In isothermal and isobaric thermodynamics systems, the Gibbs free energy can be used to calculate the maximum reversible work. In the standard state, the Gibbs energy is the maximum non-expansion work that can be taken out of a closed thermodynamic system. It is worth noting that if and only if the reaction is reversible then the maximum non-expansion work can be obtained. The reduction of the Gibbs free energy equals the work done by the system to the ambient minus the work done by the pressure. To ensure that the reaction begins spontaneously at a constant temperature and pressure, a decrease in the Gibbs free energy from the reactants to the products is essential. Because it is the thermodynamic potential of the reaction, which is minimised when the reaction reaches chemical equilibrium, the derivative of the Gibbs free energy with respect to the reaction coordinate of the system disappears[45].

Gibbs free energy is written as

$$G(p, T) = U + pV - TS = H - TS \quad (2.8)$$

where  $U$  is the internal energy of the system,  $p$  is the pressure,  $V$  is the volume,  $T$  is the temperature,  $S$  is the entropy, and  $H$  is the enthalpy.

### **2.3.2 Features of the Gibbs free energy**

In the Gibbs free energy  $G(p, T) = H - TS$  formula,  $H$ ,  $T$ , and  $S$  are all state functions, so  $G$  is also a state function. The state function  $G$  represents the ability of the system to perform non-PV work under isothermal pressure. The change in the Gibbs free energy ( $\Delta G$ ) represents the favourability of a reaction occurring at a constant temperature and pressure.  $G$  is the ability of the system to perform non-PV work under isothermal pressure. One of the necessary conditions for the reaction to occur at a constant pressure and temperature is that  $\Delta G$  should be smaller than that required for non-PV work. In fact, non-PV work always equals zero, which means that the  $\Delta G$  must be smaller than zero. If it is positive, then in order to make the reaction happen, energy must be added to the system in the form of non-PV work[46].

### 2.3.3 The isothermal formula

The Gibbs free energy changes significantly with temperature and pressure. In order to obtain the Gibbs free energy under non-standard conditions, the van 't Hoff isothermal formula can be used.

$$\Delta_f G = \Delta_f G^\circ + RT \ln Q_f \quad (2.9)$$

where  $\Delta_f G^\circ$  is Gibbs free energy at the same temperature and standard pressure,  $R$  is the gas constant, and  $Q_f$  is the reaction quotient. Different temperatures use different  $\Delta_f G^\circ$  values. In isothermal and isobaric reactions, if  $\Delta_f G^\circ$  is negative, the positive reaction is spontaneous. If  $\Delta_f G^\circ$  is positive, the reverse reaction is spontaneous. When it is at the equilibrium condition,  $\Delta_f G^\circ = 0$  and  $Q_f = K$ ,  $K$  is the equilibrium constant, and Equation (2.9) can also be written as:

$$\Delta_f G^\circ = -RT \ln K \quad (2.10)$$

From the discussion, one conclusion can be obtained: when  $\Delta_f G^\circ > 0$ ,  $K < 1$ , when  $\Delta_f G^\circ = 0$ ,  $K = 1$ , and when  $\Delta_f G^\circ < 0$ ,  $K > 1$ .

## 2.4 Data science and machine learning

### 2.4.1 The relationship between data science and materials science

As big data and artificial intelligence have developed significantly in recent years, they have been applied in almost every sphere of society. One application is combining data science and machine learning with materials science[47] and computational chemistry [48], which makes it possible for the development of data mining and machine-learning tools that can help scientists to research materials more efficiently [49]. Specifically, because of the data mining and machine-learning tools, a vast majority of material properties can be obtained, especially when investigating catalysts[50].

In order to find a suitable catalyst for the reaction, the activity, selectivity, and stability of the catalyst need to be optimised. Based on machine learning, scientists can use raw data to retrieve those features, which are represented as descriptors, predictors, and so forth. Even though only these three properties (i.e., activity, selectivity, and stability) are required in catalysis research, many other properties can also be obtained by machine-learning tools, depending upon the composition and structure of the material[51]. There are three major steps when machine-learning tools are used: 1) data mining and storage, 2) material featurisation, and 3) machine-learning modelling.

In the first step, the most important aspect is data sharing and recycling, which promotes the development of a computational material database. To use DFT calculations – computer-aided calculations are generally based – and machine-learning tools, the data must be structured, and small, relevant subsets should be obtained from larger datasets. Both the input and output of the parameters should be reproduced – for example, parameters such as cut-off energy, pseudopotential, and  $k$ -points used in a solid-state DFT calculations should be stored. Databases that use Structured Query Language (SQL), such as SQLite, MySQL, and PostgreSQL, are used to store information that is

defined. For example, the Atomic Simulation Environment (ASE) provides the utilities for storing atomic structures and related information retrievable from DFT calculations into a relational database [52]. Other databases with noSQL/not-only SQL backends treat data as key-value pairs, which can adapt to changes in the data format or structure. Examples of such databases are Materials Project[53] and MaterialsCloud[54].

The third step is machine-learning modelling. By modelling the data obtained from the first two steps, scientists can predict, casually understand, and mechanically explain the model. In machine learning, especially in materials and atomic datasets, the models are accurate when interpolating similar systems but are not very accurate for other systems. Therefore, machine-learning models should be able to generalise predictions or understandings into data dissimilar to the data sets. There are several kinds of machine-learning models, each of which has different functions and operates under different conditions. As such, it is worth investigating which model is the most appropriate. Usually, machine-learning models are categorised into unsupervised and supervised ones. The categories may be further sub-divided as follows:

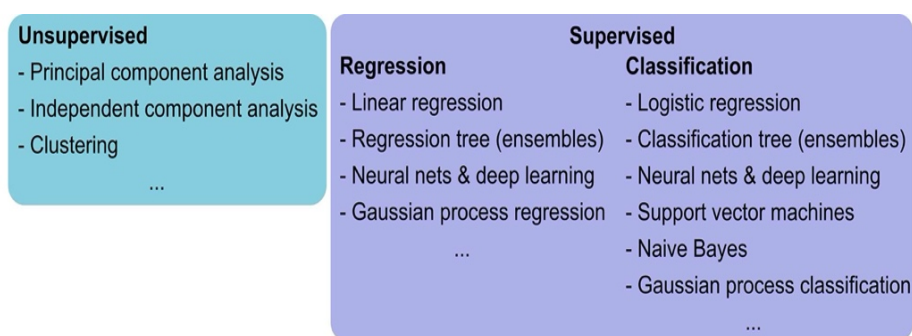


Fig. 2.6 The classification of machine learning models. (Figure reproduced from ref[40].)

Unsupervised models can infer patterns in unmarked data, which can help create causal and mechanical theories, and thus be used in predictive studies. One unsupervised model is *k*-means clustering[55]. This model has several advantages – for example, it can be easily prosecuted and adjusted, and it is easy to understand and visualise. It can also separate big datasets and compute efficiently[56]. Other unsupervised models

include principal component analysis[57], self-organising maps[58], and hidden Markov models[59].

Supervised models comprise regression and classification models. Regression models contain consequent numerical results such as selectivity, adsorption energy, molecular weight of the polymer, and band gaps. When the results are limited to a set of tight ranges, however, classification models are used. Classification models can, for instance, categorise materials into conductors/semi-conductors/insulators.

Recent computational catalysis research also falls into one of two categories. The first method uses a descriptor to investigate solid bulk materials. In a method is called catalysis informatics[60], researchers use the structure and composition of catalysts to predict and understand their selectivity, activity, and stability. The second method is accelerating typical optimisation algorithms based on machine learning. Traditional optimisation algorithms calculate the energy and force in each step during the optimisation, which is cumbersome. New machine-learning models can thus be developed to calculate these properties of the atomic structures, thus reducing the number of multi-step calculations and simplifying the entire process, which is beneficial for catalyst research[61].

## **2.5 Physical descriptor for the Gibbs energy of inorganic crystalline solids**

In recent years, as science and technology have developed, DFT calculations and materials informatics have been used to rapidly populate computational materials databases, which makes it easier to screen materials for target properties[1, 62]. Although there are an increasing number of such materials, only a small fraction have known Gibbs formation energies ( $\Delta G_f(T)$ ), which is used to predict the stability and the synthesisability of materials at different temperatures. Experimental methods to

determine  $\Delta G_f(T)$  are demanding, thus researchers are more likely to focus on the discovery and synthesis of new materials rather than obtaining the  $\Delta G_f(T)$  by calorimetry.

First-principle computational approaches for calculating the  $\Delta G_f(T)$  include the calculation of the vibrational contribution to  $G(T)$  as a function of volume[63]. However, calculating the vibrational entropy of phonons quantum mechanically requires significant computational resources. As such, the number of computational materials databases has exceeded the number of materials with computed  $\Delta G_f(T)$ , which prevents scientists from gaining a comprehensive understanding of the stability of various inorganic materials.

Based on symbolic regression, researchers can obtain optimised analytical expressions of intrinsic properties from experimental and calculated data. In 2018, Bartel *et al.* proposed a descriptor to predict Gibbs formation energies from high-throughput DFT calculations of a single inorganic structure by using the statistical-learning approach sure independence screening and sparsifying operator (SISSO), which makes the investigation of the temperature-dependent material stability highly feasible with negligible computational cost. The authors apply the descriptor to extrapolate the Gibbs free energy from the formation enthalpies 0 K  $\Delta H_f$ , which can be easily obtained using DFT calculations.

$$G^\delta(T) = G(T) - \Delta H_f(0\text{ K}) \quad (2.11)$$

Here, the temperature and material dependence of the enthalpic contribution to the  $G^\delta(T)$  are relatively larger than those of the entropic contribution ( $TS$ ). So, if the standard state formation enthalpy  $\Delta H_f$  is known, the temperature dependence of the enthalpy can be predicted reliably.  $G(T)$  in Equation (2.11) is obtained by QHA of



phonon free energy – a method that uses phonons to investigate volume-dependent thermal effects.

In order to obtain the Gibbs formation energy of a given compound, the  $G_i(T)$  is needed in addition to the  $\Delta H_f(0K)$  and  $G(T)$ .  $G_i(T)$  represents the chemical potential of elements. After those values are obtained, the Gibbs formation energy can be calculated as Equation (2.12):

$$\Delta G_f(T > 0K) = \Delta H_f(0K) + G^\delta(T) - \sum_i^N \alpha_i G_i(T) \quad (2.12)$$

Here,  $N$  represents the number of elements in the compound,  $\alpha_i$  is the stoichiometric weight of element  $i$ , and  $G_i$  is the absolute Gibbs energy of the element.

## Chapter 3 Theoretical understanding of Density Functional Theory (DFT)

Since the work in this thesis is mainly based upon DFT calculations, a brief overview of this theory is necessary.

### 3.1 The Schrödinger equation

Quantum mechanics is a theory that can be used to interpret the behaviour of electrons at the atomic scale. In quantum physics, the state of a microscope particle is described by the wave function ( $\Psi$ ), which is the solution of the linear partial differential Schrödinger equation. For most quantum chemical or quantum physical approaches, the main aim is to solve the time-independent, non-relativistic Schrödinger equation:

$$\hat{H}\Psi_i(\vec{x}_1, \vec{x}_2, \dots, \vec{x}_N, \vec{R}_1, \vec{R}_2, \dots, \vec{R}_M) = E_i\Psi_i(\vec{x}_1, \vec{x}_2, \dots, \vec{x}_N, \vec{R}_1, \vec{R}_2, \dots, \vec{R}_M) \quad (3.1)$$

Here,  $\hat{H}$  is the Hamilton operator of a system that comprises  $M$  nuclei and  $N$  electrons without magnetic or electric fields.  $\hat{H}$  can be written as the summation of the kinetic energy of electrons and nuclei, the attractive electrostatic interaction between the nuclei and electrons, and the repulsive potential due to the electron–electron and nucleus–nucleus interactions:

$$\hat{H} = -\frac{1}{2}\sum_{i=1}^N \nabla_i^2 - \frac{1}{2}\sum_{A=1}^M \frac{1}{M_A} \nabla_A^2 - \sum_{i=1}^N \sum_{A=1}^M \frac{Z_A}{r_{iA}} + \sum_{i=1}^N \sum_{j>i}^N \frac{1}{r_{ij}} + \sum_{A=1}^M \sum_{B>A}^M -\frac{Z_A Z_B}{R_{AB}} \quad (3.2)$$

Because of the significant mass differences between the nuclei and electrons, the Schrödinger equation can be simplified as

$$\hat{H}_{elec}\Psi_{elec} = E_{elec}\Psi_{elec} \quad (3.3)$$

where  $\hat{H}_{elec}$  is the electronic Hamiltonian, simplified from the  $\hat{H}$  using the Born–Oppenheimer approximation, which assumes that the electrons are moving in the field of fixed nuclei. As the nuclei are fixed, the kinetic energy of the nuclei is zero, and the potential energy between two nuclei is constant; therefore, so the  $\hat{H}_{elec}$  can be written as

$$\hat{H}_{elec} = -\frac{1}{2} \sum_{i=1}^N \nabla_i^2 - \sum_{i=1}^N \sum_{A=1}^M \frac{Z_A}{r_{iA}} + \sum_{i=1}^N \sum_{j>i}^N \frac{1}{r_{ij}} = T + V_{Ne} + V_{ee} \quad (3.4)$$

### 3.2 The Hohenberg–Kohn Theorems: Origin of DFT

In 1964, Hohenberg and Kohn published the paper that is now seen as the cornerstone of the DFT [64]. Two theorems (HK theorems) were proposed in this paper, which are discussed below.

For a common external potential, the ground state energy of a many-electron system is a unique functional of the single-electron density:

$$E = E[\rho(r)]. \quad (3.8)$$

The second theorem states that, when the input density is the ground state density, the functional delivers the ground state energy:

$$E_0 \leq E[\tilde{\rho}] = T[\tilde{\rho}(r)] + E_{Ne}[\tilde{\rho}(r)] + E_{ee}[\tilde{\rho}(r)] \quad (3.9)$$

The first HK theorem states that the mutual connections between the electron density and the ground state energy, and the Hamiltonian operator is determined by the electron density – that is, all properties in the system are determined. The second HK theorem is derived from the energy variation principle, which indicates that the ground state energy will be delivered by the functional only if the ground state density is inserted. These two theorems are very important for the establishment of modern DFT and are also potential avenues for the study of DFT.

### 3.3 The Kohn-Sham approach

One year after the HK theorems were proposed, Kohn and Sham proposed a method to reach the hitherto unknown functional, and they realised that problems with density functionals are closely related to the way the kinetic energy is determined[65]. In their approach, the energy functional is described in two parts. First,

$$E[\{\Psi_i\}] = E_{known}[\{\Psi_i\}] + E_{XC}[\{\Psi_i\}] \quad (3.10)$$

$E_{known}$  expresses the Coulomb interactions between the electrons and nuclei, which are clearly known and can be calculated. However,  $E_{XC}$ , which is called the exchange–correlation functional, comprises all those features that are obscure, such as self-interaction correction, exchange and correlation, kinetic energy, and the residual portion of the kinetic energy. In the Kohn–Sham (KS) approach, the problem is transferred to find the solution of a set of single-electron wave functions:

$$\left[ -\frac{\hbar^2}{m} \nabla^2 + V(r) + V_H(r) + V_{XC}(r) \right] \psi_i(r) = \varepsilon_i \psi_i(r) \quad (3.11)$$

The KS equation has three potential energy terms,  $V$ ,  $V_H$ , and  $V_{XC}$ .  $V$  indicates the interaction between one electron and all nuclei, while  $V_H$ , also called the Hartree potential energy, can be written as

$$V_H(r) = e^2 \int \frac{n(r')}{|r - r'|} d^3r' \quad (3.12)$$

$V_H$  describes the Coulomb repulsion between the total electron density generated by all the electrons and the single atom considered in the KS equation.  $V_H$  contains a self-interaction because the single electron described in the KS equation is a part of the total electron density, so part of  $V_H$  is the Coulomb interaction of that electron with itself.

### 3.4 The exchange-correlation functional

After the development of the HK theorems and KS calculations, scientists became close to solving the Schrödinger equation. However, there is still a challenge: to solve the KS equation, the  $E_{XC}[\{\Psi_i\}]$  must be given. The real form of the exchange–correlation functional is unknown, so it is very important to find approximations of the  $E_{XC}$  functional. Indeed, finding a suitable exchange–correlation functional is the core of the DFT, which determines the performance of the calculation. While an improper correlation functional may lead to error, an appropriate correlation functional will ideally ensure that the results from the calculation agree with those of the experiment[66]. In the following section, several exchange–correlation functionals are introduced.

The first is the local density approximation (LDA)[67] proposed by Dirac and Bloch. This approach assumes that the  $E_{XC}$  is a function of the density of a presumptive uniform electron gas in a system that is electrically neutral. Because this approach only uses local electron density to determine the exchange–correlation functional, it is called the LDA. The exchange energy can be written as

$$E_X^{LDA}[\rho] = \int \rho(r) \varepsilon_X(\rho(r)) dr \quad (3.13)$$

The correlation energy is  $E_C^{LDA} = E_{XC}^{LDA} - E_X^{LDA}$ , which cannot be determined. This problem originated in numerical quantum Monte Carlo simulations, which simulate uniform electron gas. In the approximation, the electron density is constant at all points in the space – that is,  $\rho(r)$  is unchanged – but for real materials, this approximation is not meaningful. When considering LDA in an unrestricted version, it becomes the local spin-density approximation, which separates the  $\rho(r)$  into two spin densities,  $\rho(r) = \rho_\alpha(r) + \rho_\beta(r)$ . The LSD approximation works well when there are an even number of electrons in the system, owing to the symmetry break[68]. The local spin-density approximation can be written as

$$E_{XC}^{LSD}[\rho_\alpha, \rho_\beta] = \int \rho(r) \varepsilon_{XC}(\rho_\alpha(r), \rho_\beta(r)) dr \quad (3.14)$$

As mentioned above, in real materials, the non-uniform electron gas results in inconsistencies with real experimental observations. As such, the generalised gradient approximation (GGA) was proposed, and functionals based on this approximation can accurately calculate the total energies[69], atomisation energies[70, 71], and energy barriers[72, 73]. The generalised gradient can be depicted as  $\nabla\rho$ , then the exchange–correlation energy can be expressed as

$$E_{xc}[\rho(r)] = \int f(\rho, \nabla\rho) dr \quad (3.15)$$

There are many different types of GGA functionals; the Perdew–Wang (PW91) functional and Perdew–Burke–Ernzerhof (PBE) functional are two types that are always used in solid-state calculations. The exchange energy of the PBE functional can be written as

$$E_x^{PBE} = -\int \rho^{\frac{4}{3}} \left[ \frac{3}{4} \left( \frac{3}{\pi} \right)^{\frac{1}{3}} + \frac{\mu s^2}{1 + \frac{\mu s^2}{\kappa}} \right] dr \quad (3.16)$$

where  $\kappa$  is the crest value of the Lieb–Oxford bound[74],  $s = |\nabla\rho|/(2k_F \rho)$ , and  $\mu$  is the effective gradient.

### 3.5 Application of DFT: Vienna Ab initio Simulation Package

Vienna Ab initio Simulation (VASP) is software that can perform electronic structure calculations and quantum mechanics–molecular dynamics simulations, based on DFT[75]. It can solve the KS equation to obtain the electronic states and energy of the system with the imposing of periodic boundary conditions [76] to deal with atoms, molecules, clusters, nanowires(tubes), films, crystals, quasicrystals, and amorphous materials, as well as surface systems and solids. It can be applied to determine the structural parameters, state equations, mechanical properties, optical properties, magnetic properties of solids.

Pseudopotentials, which approximate the behaviours of core electrons near the nuclei, are used to further simplify the calculations to be performed on complex systems. Standard pseudopotentials separate atom into two parts, valence electrons and frozen ion cores, which have nuclei and inner electrons[77], using a pseudo wavefunction that varies in the spatial region to imitate the all-electron counterpart. In some systems that contain heavy elements, when comparing the results of all-electron calculations and pseudopotential approximations, it seems that the pseudopotential approximation can take into account the relativistic effects more efficiently. Because the results obtained from the pseudopotential approximation are good[78], it is the preferred method in approximate relativistic molecular theories.

## **Chapter 4 Can Metal Intermixing Cooperatively Improve Perovskites as Redox Materials for Thermochemical Ammonia Synthesis? A Case Study on (Sr,Y)(Ti,Ru)O<sub>3</sub>**

(This chapter has been published in The Journal of Physical Chemistry C, *J. Phys. Chem. C* 2021, 125, 31, 17019–17030)

### **4.1 Introduction**

Ammonia, a simple compound of nitrogen and hydrogen with the formula NH<sub>3</sub>, is one of the most important chemicals or precursors in the manufacturing of products that we use every day. Importantly, ammonia can be dissociated and turned into an efficient source of hydrogen to power hydrogen fuel cells without greenhouse emission, facilitating the development of human society towards the hydrogen economy. In particular, with 100 years of development, the supply chain infrastructures from synthesis, transportation to storage and safe usages of this world's second-largest manufactured industrial chemical have been well established, making the usage of ammonia as an intermediate product for hydrogen production a feasible approach for the realization of hydrogen economy. However, the current industrial process of ammonia synthesis, which is based on the modified Haber-Bosch cycles, is one of the most complicated processes. It combines nitrogen and hydrogen directly under high temperatures and pressures in the presence of a catalyst including Fe-based alloys to form ammonia [79]. It results in the ammonia production being one of the energy inefficient industries. As such, the development of an alternative manufacturing technology to replace the Haber-Bosch process, in response to the ongoing challenge of shortages in global energy supplies, as well as climate changes is eagerly awaited.

Over the past decade, electrocatalysis[80], bio-catalysis[81], plasma-catalysis[82], as well as photocatalysis[83] have attracted enormous research efforts to develop them as alternative approaches to tackle the fundamental problems of large energy consumption



in ammonia production. Nevertheless, the processes that use renewable energies, such as photo- and electrocatalysis, suffer from the well-known bottlenecks of low Faradic efficiency[84] and poor selectivity[85], making them difficult to be scaled up for industrial applications. Different from these approaches, which the catalyst recovers to its original state from short-lived reaction intermediate in the same reaction vessel, chemical looping process[30, 86] that consists of two or more full redox reactions in different chambers exhibits unique advantages to continuously drive the process of ammonia formation[87]. In this process, the starting catalytic material  $C$  is first converted to a metastable phase/compound  $C'$ , which is subsequently transferred to the next chamber where the second redox reaction leads to both the product formation and the regeneration of  $C$ . Here,  $C$  and  $C'$  are often referred as the ‘redox-pair’ or the ‘active material’, as they do not behave as catalyst in *individual* step of the chemical loop.

In recent year, thermal ammonia synthesis (TAS) as a chemical looping method has emerged as a promising strategy for green ammonia production under ambient pressure. With a suitable thermal redox pair, this approach owns the potential of utilizing the full spectrum of thermal energies from either renewable source, such as concentrated solar thermal energies[31] (with operating temperature between 1000-1600 °C), geothermal energies (from 125-600 °C), or waste heat from thermal power plants, metal refineries, or turbine engines (~800-1600 °C).

However, there are a very small number of suitable solid-state redox materials that are capable of driving TAS reactions. This has been restricting the development of these technologies. Up to date, most efforts have been devoted to searching binary metal oxides with low Gibbs reaction energy of inter-conversion to their corresponding nitrides as the potential redox materials. Several binary redox pairs, such as  $Al_2O_3/AlN$ [26],  $Cr_2O_3/CrN$ [36],  $MoO_2/Mo_2N$ [88],  $MnO/Mn_5N_2$ [37], have been experimentally proven as promising active materials for solar thermal ammonia synthesis. Although carbon can also be used as additional reducing agent to enhance the performance of some of these redox pairs, the byproduct of  $CO_2$  in these chemical

looping causes a concern in environmental pollution. Currently, only 35 pairs of binary metal oxides/nitrides are found to be the suitable redox materials for TAS because the data of experimentally determined Gibbs formation energies of metal nitrides are sparse[38].

To overcome the experimental limit, Density Functional Theory (DFT)-based high-throughput computational screening has become pivotal in driving material innovations during the past decades[89, 90]. However, whilst calculating the formation enthalpies of solids at 0 K is trivial, obtaining temperature-dependent formation free energies requires additional calculations on the entropic contributions from phonon vibrations, which involves significantly larger amount of computational resources. With the recent advances of machine-learning in material science, a Gibbs formation energy descriptor was developed[41] to enable the ultra-fast enumeration of Gibbs formation energies based on the DFT total energies and atomic volumes. With this advancement, Bartel *et al.* evaluated the catalytic performance of 1148 metal oxide/metal nitride pairs for STAS (Solar Thermal Ammonia Synthesis) using high-throughput theoretical screening [91]. Nevertheless, only the redox pairs based on B, V, Fe, and Ce exhibit good potential for the STAS process. Therefore, there is a pressing need to discover new solid-state redox pairs with more complex compositions.

Recent experimental work on  $\text{Sr}_{1-x}\text{Y}_x\text{Ti}_{1-y}\text{Ru}_y\text{O}_{3-\delta}$  has demonstrated it as a promising candidate for ammonia dehydrogenation due to its high activity and stability, which may also be applicable for thermal ammonia synthesis [92]. However, there is a lack of consolidated approach to reveal how complex compositional engineering of oxides can improve their performances as heterogeneous catalysts. This has significantly impeded the development of complex oxide thermal catalysts. Fundamentally, the new chemical bonding states induced by chemical alloying, which do not exist in the parent compounds, may facilitate the breaking of triple bonds in nitrogen to lower the reaction free energy. This is the fundamental science behind the concept of ‘cooperative enhancement effect’[93], which is particularly relevant to compositionally engineered

perovskites to explore how it modifies the subtle interactions between charge, orbital and spin degrees-of-freedom to deliver unconventional functionalities. This effect is quantifiable theoretically and has been extensively used to examine how multiple coexistence of non-covalent interactions in molecular systems enhances their stabilities and functionalities. However, to our best knowledge, this has not been applied in the design of solid-state catalysts. Whilst accurate computation of formation energies for simple solids can now be routinely done with DFT even using the computational power available on a personal laptop, this is not the case for establishing the thorough compositional-dependent thermodynamic landscapes of solid solutions, as the number of possible random atomic configurations in a solid solution can be factorially large.

To tackle this challenge, we strategically combine high-throughput DFT-based random configurational sampling, machine learned Gibbs formation energy descriptor and the concept of cooperative enhancement, making it tractable for systematically evaluating the performance of mixed cation perovskite oxides and oxynitrides as redox pairs for ammonia synthesis with renewable thermal energies. With this, we evaluate the feasibility of metal-alloyed perovskite oxides/oxynitrides  $\text{Sr}_{1-x}\text{Y}_x\text{TiO}_3/\text{Sr}_{1-x}\text{Y}_x\text{TiO}_y\text{N}_{3-y}$ ,  $\text{Sr}_{1-x}\text{Y}_x\text{RuO}_3/\text{Sr}_{1-x}\text{Y}_x\text{RuO}_y\text{N}_{3-y}$ ,  $\text{SrTi}_{1-x}\text{Ru}_x\text{O}_3/\text{SrTi}_{1-x}\text{Ru}_x\text{O}_y\text{N}_{3-y}$  and  $\text{YTi}_{1-x}\text{Ru}_x\text{O}_3/\text{YTi}_{1-x}\text{Ru}_x\text{O}_y\text{N}_{3-y}$  with the references to their pristine counterparts of  $\text{SrTiO}_3/\text{SrTiO}_y\text{N}_{3-y}$ ,  $\text{SrRuO}_3/\text{SrRuO}_y\text{N}_{3-y}$ ,  $\text{YTiO}_3/\text{YTiO}_y\text{N}_{3-y}$  and  $\text{YRuO}_3/\text{YRuO}_y\text{N}_{3-y}$ , respectively. Most importantly, the extremely high thermodynamic instabilities of the pristine perovskite nitrides inspired us to further explore the uncharted chemical space of mixed cation perovskite oxynitrides as the TAS reaction intermediate for enhancing the efficiency of ammonia production. By comparing the Gibbs formation energies and the Gibbs reaction energies in ammonia synthesis using these redox pairs, we demonstrate as redox pairs the performance of the pristine perovskite oxides/oxynitrides is mediocre. However, one of the A-site rare-earth-metal-alloyed perovskite pairs, namely  $\text{Sr}_{0.875}\text{Y}_{0.125}\text{TiO}_3/\text{Sr}_{0.875}\text{Y}_{0.125}\text{TiO}_{2.875}\text{N}_{0.125}$  shows a subtle cooperative enhancement relative to its complementary pristine structures of  $\text{SrTiO}_3/\text{SrTiO}_{2.875}\text{N}_{0.125}$  and  $\text{YTiO}_3/\text{YTiO}_{2.875}\text{N}_{0.125}$  in reducing the Gibbs reaction energy of the limiting reaction in

a two-step cycle, providing a universal approach to search for chemical modification pathways that lead to high performance heterogeneous thermal active materials.

## 4.2 Methodologies

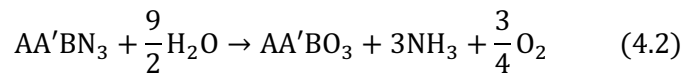
### Two-step chemical looping in solar thermal ammonia synthesis

In this work, we consider the STAS as a two-step process. Furthermore, instead of using the nominal composition of  $\text{Sr}_{1-x}\text{Y}_x\text{Ti}_{1-y}\text{Ru}_y\text{O}_{3-\delta}$ , we focus here on purely A- or B-site mixed perovskite  $\text{ABX}_3$  solid solutions with full X-site occupancy to dissect the effect of metal intermixing on the TAS as redox pairs.

The first process is a nitridation process at high temperature (1200-1800 K). Assuming the oxide is fully consumed, using an A-site intermixed perovskite as an example, the reaction proceeds as:

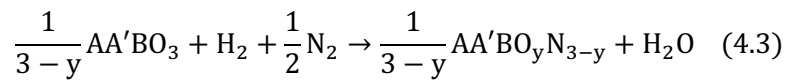


Then a hydrolysis process at 600-1200 K follows to hydrolyze nitride back to oxides, while generating ammonia:

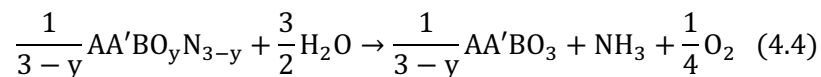


However, as discussed later on when testing the pristine perovskites, it is found that full nitridation of perovskites is highly endothermic. Since the main purpose of the reaction cycle is not to produce nitride, it would be more appropriate to consider partial nitridation, thus forming perovskite oxynitrides as the reaction intermediates. As such, we consider the following balanced reactions:

1. Nitridation:



2. Hydrolysis:



Although many precious metals, such as Ru, are known good catalysts for chemical reactions, the research on the perovskite oxides/oxy-nitrides as thermal redox materials for ammonia production is very limited. A critical requirement for using the perovskite redox pairs is the reduced compounds need to be oxidized and restore the original structures. In reactions (4.1-4.4), we specifically choose not to use metal elements/alloys as the reaction intermediate to ensure we are investigating the potential of the perovskite phase as redox pair not the metals. This is also because many perovskite oxides may not be reformed by simply oxidizing the metals at high temperature, hence it is also important to control the reduction atmosphere in real experiments such that the oxides can only be partially reduced. Furthermore, there exist ample experimental evidences that the perovskite oxides are capable of losing/regaining oxygens under cyclic redox reaction conditions by remaining the basic perovskite structures, and this is a phenomenon that has been harnessed in the perovskite oxides for thermal storage applications.[94] Manipulating the reduction level of perovskite oxides can modify the chemical states and local chemical environment of the metallic ions. This may be the origin to facilitate the  $\text{N}_2$  dissociation and the subsequent  $\text{NH}_3$  formation. Such a mechanism is the key rationale behind the choice of reactions (4.3-4.4) as our targeted reactions to investigate theoretically the potential for alloyed perovskites as redox materials for ammonia synthesis. Using theoretical modelling to discover which composition of perovskite alloy is capable of lowering the reaction free energies to the largest extent will also provide critical guidance to experiments, by significantly reducing the cost associated with the optimization of materials' compositions through trial-and-error approach.

It is clear that in order to calculate the reaction free energies for reactions (4.1-4.4), we must first obtain the formation energies for the perovskite solid solutions with different chemical compositions. These are detailed as following.

## Random structure sampling and DFT calculation

All perovskites in this work are modeled using a  $2 \times 2 \times 2$  supercell. This contains 8 A-/B- site cations and 24 X-site anions in total. Following our previous work on solid solutions of mixed halide perovskites[95], we first generate random configurations of oxynitrides  $\text{ABO}_y\text{N}_{3-y}$  by sequentially replacing O with N in the perovskite lattice. As discussed later, the sampling is only performed for  $3 - y \leq 0.375$ , and only the oxynitride structure with  $3 - y = 0.125$  is retained as the starting point for sampling the random solid solutions with A-/B-site metal mixing. This is because the instabilities of most oxynitrides increase sharply with respect to  $y$ . All nitrides  $\text{ABN}_3$  are modelled by replacing all O in  $\text{ABO}_3$  by N followed by structure optimizations using DFT. The same approach is used to generate the random configurations of  $\text{A}_x\text{A}'_{1-x}\text{BO}_3$ ,  $\text{AB}_x\text{B}'_{1-x}\text{O}_3$ ,  $\text{A}_x\text{A}'_{1-x}\text{BO}_{2.875}\text{N}_{0.125}$ ,  $\text{AB}_x\text{B}'_{1-x}\text{O}_{2.875}\text{N}_{0.125}$  solid solutions across all 8 compositions of  $x \in [\frac{1}{8}, \frac{2}{8}, \dots, 1]$ . In total, 415 solid state configurations (144 for oxides and 271 for oxynitrides) have been sampled in our work.

Both the ionic positions and the lattice parameters of these compounds are fully relaxed. All DFT calculations are performed in VASP[75] with exchange-correlation energy approximated by PBE (Perdew-Burke-Ernzerhof)[96] functional. Electron density are expanded with standard PAW (projector augmented wave method)[97], with kinetic energy cutoff of 400 eV. The Monkhorst-Pack[98]  $k$ -point sampling is set to  $6 \times 6 \times 6$  in the Brillouin zone for all structures. Structural optimizations are terminated when the total energy change between two ionic steps is lower than  $2.5 \times 10^{-3}$  eV/atom. The formation enthalpy  $\Delta H_f$  of every optimized structure is calculated with respect to its constituent atoms, e.g.:

$$\Delta H_f[\text{ABO}_3] = E[\text{ABO}_3] - E[\text{A}] - E[\text{B}] - \frac{3}{2}E[\text{O}_2] \quad (4.5)$$

in which,  $E$  represents the total energy of the corresponding structure or atom. All the values of  $\Delta H_f$  reported here are normalized by the total number of atoms in the simulation supercell.

## Calculation of the Gibbs formation energies

After we calculated the formation enthalpy  $\Delta H_f$  of the solid solutions, to evaluate the reaction free energies at finite temperature, we must calculate the temperature-dependent Gibbs formation energies  $\Delta G_f(T)$  for each compound, which is obtained by using the machine-learned temperature-dependent Gibbs formation energy model as described in Ref.19 20. The validity of this model is benchmarked against the Gibbs formation energies obtained using DFT-based quasiharmonic approximation calculations, and as shown in the Supporting Information, the agreement in results obtained with these two models are high, validating the use of Gibbs energy descriptor for high-throughput screening of the solid-state reaction thermodynamics. All the  $\Delta G_f$  values for materials in gaseous phase are obtained from FactSage[99] except for elemental gases ( $H_2$ ,  $N_2$  and  $O_2$ ), which are zero by definition.

## Calculation of the reaction free energies

After obtaining the Gibbs formation energies for the reactants and products in the STAS chemical looping, the Gibbs reaction free energies of each reaction in the process can be evaluated. The reaction free energies are the fundamental quantities that will enable us to judge whether a redox pair is capable of catalyzing ammonia synthesis. By definition, the reaction free energies can be calculated as:

$$\Delta G_r(T) = \sum_i^{products} v_i \Delta G_{f,i}(T) - \sum_i^{reactants} v_i \Delta G_{f,i}(T) \quad (4.6)$$

where  $v_i$  is the stoichiometric coefficient of species  $i$  that leads to the formation of 1 mol  $NH_3$  in one complete reaction cycle.

## Evaluation of the cooperative effects in the STAS cycles

Finally, to judge whether metal-substituted perovskites redox pairs are more suitable for STAS compared to the pure perovskites redox pairs, we analyze the possible existence of cooperative effects driven by metal intermixing according to the following criteria (using A-site-intermixed perovskite as example)[93, 100]

$$\Delta G_{AA'BO_3}^{\text{reaction}} < \min \{ \Delta G_{ABO_3}^{\text{reaction}}, \Delta G_{A'BO_3}^{\text{reaction}} \} \quad (4.7)$$

$\Delta G_{AA'BO_3}^{\text{reaction}}$ ,  $\Delta G_{ABO_3}^{\text{reaction}}$  and  $\Delta G_{A'BO_3}^{\text{reaction}}$  represent the reaction free energies of a specific reaction in the STAS cycle when using the compounds indicated in the subscript as the active materials. This inequality indicates that, in a specific reaction, if metal-substituting redox pair has the lowest reaction energy compare to its complementary pure perovskite counterparts, it means metal substitution improves the performance of the pure perovskites for STAS.

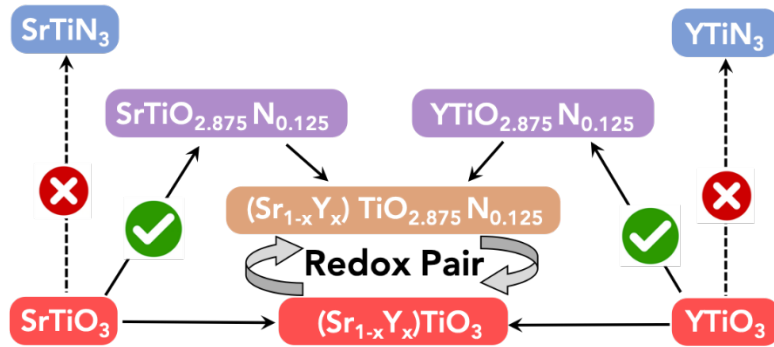


Fig. 4.1. Diagram exemplifying the relationship among solid solutions used as redox materials for thermal ammonia synthesis.

## 4.3 Results and Discussions

### Reaction thermodynamics of pristine perovskites

In order to determine the viability of metal-alloyed perovskite oxides/oxyntitrides for STAS, we must establish the baseline reaction thermodynamics with the pristine



perovskite oxides/oxyntitrides that are used as redox pairs in the TAS process. This provides us the references to reveal the fundamental mechanisms behind the efficacy of using perovskite alloys with complex compositions that involves both cation and anion intermixing in STAS, establishing a high-level overview on the relationship among the perovskite alloys and their pristine counterparts in order to facilitate the subsequent discussions. This relationship, using  $\text{Sr}_{1-x}\text{Y}_x\text{TiO}_3$  as an example, is presented in Fig. 4.1.

TABLE 4.1. The Gibbs formation energies of the redox pairs at different temperatures for thermal ammonia synthesis. For the perovskite nitrides, we only calculated their formation enthalpies at 0 K, so the rest of the table is represented by ‘-’. All energies are given in the unit of eV/atom.

Structures	$\Delta H_f$	$\Delta G_f(600\text{ K})$	$\Delta G_f(1200\text{ K})$
$\text{SrTiO}_3$	-3.561	-3.214	-2.897
$\text{SrTiO}_{2.875}\text{N}_{0.125}$	-3.409	-3.090	-2.793
$\text{SrTiN}_3$	-0.534	-	-
$\text{SrRuO}_3$	-2.192	-1.867	-1.575
$\text{SrRuO}_{2.875}\text{N}_{0.125}$	-2.115	-1.814	-1.541
$\text{SrRuN}_3$	-0.004	-	-
$\text{YTiO}_3$	-3.384	-3.049	-2.747
$\text{YTiO}_{2.875}\text{N}_{0.125}$	-3.317	-3.013	-2.735
$\text{YTiN}_3$	-0.898	-	-
$\text{YRuO}_3$	-2.128	-1.816	-1.541
$\text{YRuO}_{2.875}\text{N}_{0.125}$	-2.195	-1.911	-1.658
$\text{YRuN}_3$	-0.255	-	-

TABLE 4.2. The nitridation reaction energies from pristine perovskites to  $\text{ABO}_{2.875}\text{N}_{0.125}$ ,  $\text{ABO}_{2.75}\text{N}_{0.25}$  and  $\text{ABO}_{2.5}\text{N}_{0.5}$ . All energies are given in the unit of eV/atom.

Pristine perovskites	$\text{ABO}_{2.875}\text{N}_{0.125}$	$\text{ABO}_{2.75}\text{N}_{0.25}$	$\text{ABO}_{2.5}\text{N}_{0.5}$
$\text{SrTiO}_3$	0.284	0.718	1.289
$\text{SrRuO}_3$	-0.064	0.253	0.568
$\text{YTiO}_3$	-0.175	0.073	0.288
$\text{YRuO}_3$	-0.821	-1.341	-1.461

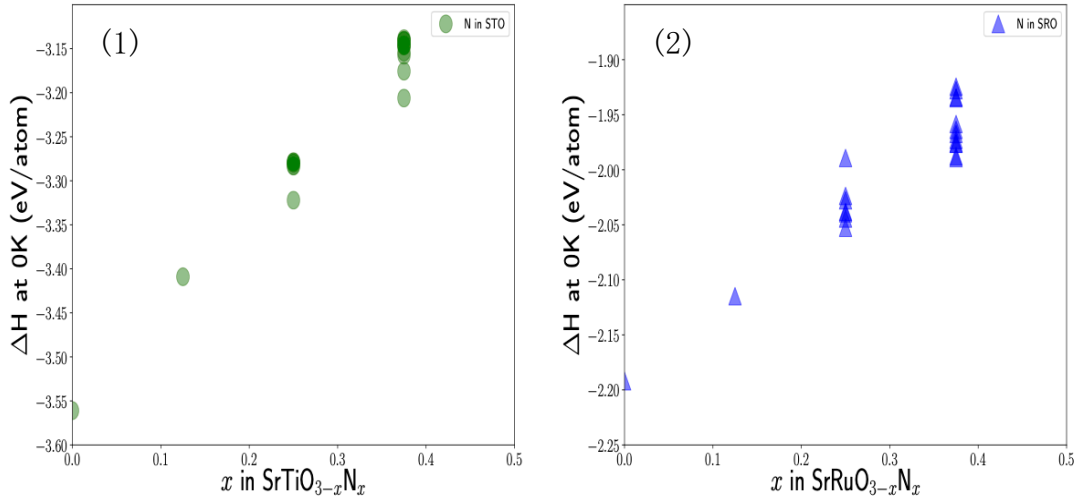
Since both perovskite oxides  $\text{ABO}_3$  and molecular  $\text{N}_2$  are generally very stable, it is extremely unlikely that  $\text{ABO}_3$  can be fully converted into  $\text{ABN}_3$  via a nitridation step. Indeed, this is what we found in Table 4.1 when we compared the formation energies

between a pair of perovskite oxide and nitrides, which shows the formation energies of the pure nitrides are always 2 eV/atom higher than the pure oxides counterparts, demonstrating the direct nitridation from  $\text{ABO}_3$  to  $\text{ABN}_3$  is unlikely. As such, no reaction can possibly proceed if we use pure nitrides as the reaction intermediate. However, for the thermal ammonia synthesis processes, we are not interested in the synthesis of pure nitrides. Importantly, most heterogeneous catalytic reactions occur on the surface of catalysts only, therefore, we proceed to consider a partially nitrated perovskite oxynitride as the reaction intermediate.

This sparks us to first investigate the thermodynamic stability landscape of perovskite oxynitride to determine a critical nitrogen concentration  $x$  in  $\text{ABO}_{3-x}\text{N}_x$ , which is to be used in subsequent reaction screenings. The energy landscapes for all four perovskite oxynitrides are shown in Fig. 4.2. It is clear that, for  $\text{SrTiO}_3$ ,  $\text{SrRuO}_3$  and  $\text{YTiO}_3$ , their formation energies increase monotonically as the concentration of nitrogen increases. According to the Eqs. (4.3) and (4.6), we can calculate the reaction energy of the nitridation reaction from  $\text{ABO}_3$  to  $\text{ABO}_{2.875}\text{N}_{0.125}$ ,  $\text{ABO}_{2.75}\text{N}_{0.25}$  and  $\text{ABO}_{2.5}\text{N}_{0.5}$  separately, which, as shown in Table 4.2 that, for  $\text{SrTiO}_3$ ,  $\text{SrRuO}_3$  and  $\text{YTiO}_3$ , as the nitrogen concentration increases, the reaction energies increase correspondingly, i.e. the nitridation reaction becomes more difficult to happen. This indicates that, practically, perovskite oxynitrides can only be formed in these compounds with ultra-diluted nitrogen concentrations. However, from Fig. 4.2, we find that the formation energy of  $\text{YRuO}_{3-x}\text{N}_x$  decreases as nitrogen concentration increases up to the limit that has been calculated, which is also reflected in Table 4.2 that the corresponding nitridation reaction energy decreases as the nitrogen concentration is increased. It can also be observed that large variations in the formation energies of  $\text{YRuO}_{3-x}\text{N}_x$  occur at  $x=0.23$  and  $0.38$  in Fig. 4.2, indicating that the stabilities of  $\text{YRuO}_{3-x}\text{N}_x$  solid solutions are very sensitive to the position of N in the lattice. However, to our best knowledge, no work on perovskite  $\text{YRuO}_3$  as a thermal redox material has been reported either experimentally or theoretically. In this regard, it is fundamentally important to further understand the chemistry of the common perovskites, i.e.  $\text{SrTiO}_3$  as a model system,

and to assess their potential and limit as active materials for the synthesis of ammonia with renewable thermal energies including solarthermal, geothermal and waste heat of power plants.

Ideally, it would be highly desirable if solid solutions of  $\text{ABO}_{3-y}\text{N}_y$  across all nitride concentrations ( $y$ ) were sampled to thoroughly investigate the nitrogen uptake capacity of perovskite oxides. However, this would imply that for each  $\text{ABO}_{3-y}\text{N}_y$  configuration at a given nitride concentration  $y$ , a separate random sampling of the metal-intermixed structures of  $\text{A}_x\text{A}'_{1-x}\text{BO}_{3-y}\text{N}_y$ ,  $\text{AB}_x\text{B}'_{1-x}\text{O}_{3-y}\text{N}_y$  must be performed, for which the associated computational cost will grow factorially for a two-site alloyed perovskite oxynitride. Since  $x=0.125$  is the lowest nitrogen concentration that we can model using our simulation supercell (with only one possible  $\text{ABO}_{3-y}\text{N}_y$  configuration), and it is the nitride concentration at which the oxynitrides for 3 out of 4 perovskite oxides are found to have the lowest formation energies, this will be the lower threshold nitrogen content that we will employ in the subsequent analysis with Eqs. (4.3) and (4.4) shown in the section of Methodologies.



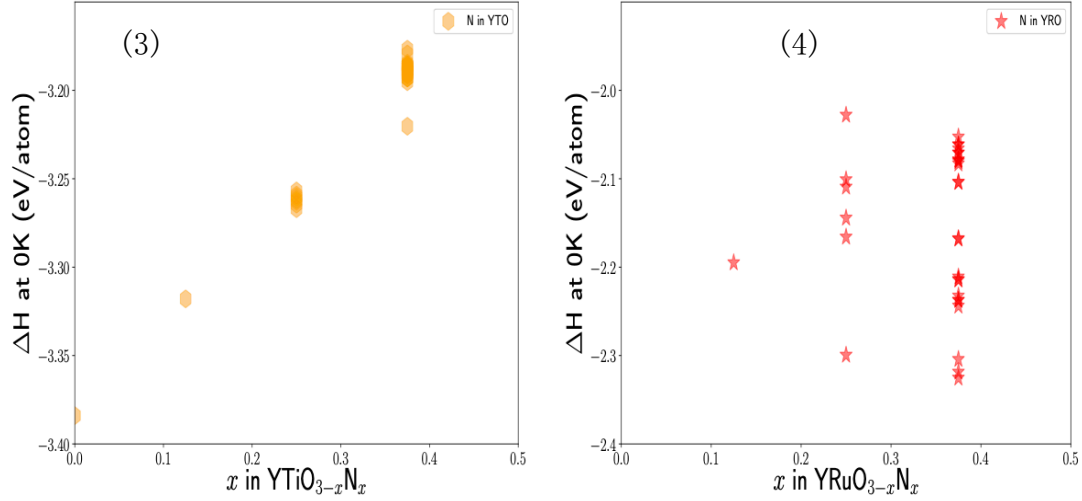


Fig. 4.2. The formation enthalpies of different N-substituting ratios of  $\text{SrTiO}_{3-x}\text{N}_x$ ,  $\text{SrRuO}_{3-x}\text{N}_x$ ,  $\text{YTiO}_{3-x}\text{N}_x$  and  $\text{YRuO}_{3-x}\text{N}_x$  ( $x = 0.125, 0.25$  and  $0.5$ ).

Having determined the critical nitrogen content for the redox pair as active materials based on 0 K formation enthalpies, we need to further examine their finite-temperature formation free energies. This is because one of the essential criteria for the redox pair being feasible to use in the chemical looping process is that each compound in the pair is required to possess negative formation free energy [ $\Delta G_f(T) < 0$ ] at the reaction temperature. In the present study, we fix the temperature for nitridation reaction at 1200 K and hydrolysis reaction at 600 K, because these are the well-accepted lowest temperature at which these reactions are most likely to proceed. Table 4.1 shows that the Gibbs formation energies for these redox materials are all negative at these two selected temperatures, meaning that they are likely to be stable at elevated temperatures. Furthermore, the results also show that the relative stabilities between oxide and its corresponding oxynitride are not altered as the temperature increases, meaning that oxynitride is not further stabilized by vibrational entropies. Nevertheless, we also note that  $\Delta G_f(T) < 0$  is insufficient criteria for judging materials' stabilities, where the decomposition energies to the corresponding binaries should ideally also be considered.[101, 102] However, as the STAS reaction energies are directly dependent on the formation free energies, here, we have chosen to focus primarily on the formation free energies as the criteria to judge materials' stabilities.

With the obtained Gibbs formation energies of the oxide/oxy-nitride redox pairs, we can calculate their corresponding reaction free energies in the TAS cycle. The results are shown collectively in Table 4.3. It can be seen that, except for  $\text{SrTiO}_3$ , all other perovskites possess a negative nitridation free energy at 1200 K, indicating these reactions occur spontaneously. Particularly,  $\text{YRuO}_3$  exhibits the most negative reaction free energies due to its high capability to take up the nitrogen. However, only  $\text{SrTiO}_3/\text{SrTiO}_{2.875}\text{N}_{0.125}$  pair shows negative free energy for hydrolysis. In the hydrolysis step, the Gibbs formation energy of  $\text{NH}_3$  is always larger than that of  $\text{H}_2\text{O}$ , hence in order to drive this reaction to occur spontaneously, this free energy difference must be compensated by an even larger decrease in Gibbs formation free energy from oxy-nitride back to the oxide. This condition can only be fulfilled with the  $\text{SrTiO}_3/\text{SrTiO}_{2.875}\text{N}_{0.125}$  pair (that has the positive nitridation reaction free energy). This analysis also shows that none of the four pristine perovskite redox pairs investigated above can solely drive both nitridation and hydrolysis reactions spontaneously due to inherent competition between nitridation and hydrolysis. This is a key motivation for us to further explore whether chemical alloying of two different perovskites can benefit the formation of  $\text{NH}_3$  by ‘combining the goods in two worlds’.

TABLE 4.3. The reaction energies of using different redox pairs during the TAS process. All energies are given in the unit of eV.

Redox pairs	$\Delta G_{\text{nitridation}}$ (1200 K)	$\Delta G_{\text{hydrolysis}}$ (600 K)
$\text{SrTiO}_3/\text{SrTiO}_{2.875}\text{N}_{0.125}$	0.284	-0.181
$\text{SrRuO}_3/\text{SrRuO}_{2.875}\text{N}_{0.125}$	-0.064	0.175
$\text{YTiO}_3/\text{YTiO}_{2.875}\text{N}_{0.125}$	-0.175	0.258
$\text{YRuO}_3/\text{YRuO}_{2.875}\text{N}_{0.125}$	-0.821	0.913

## The effect of metal intermixing on the formation Gibbs free energies

We now proceed to discuss how A-/B- site metal intermixing changes the thermodynamic stabilities of perovskite oxides/oxy-nitrides. Using our random structure

generators, 144 different configurations in total have been generated across the compositional space of  $\text{Sr}_{1-x}\text{Y}_x\text{TiO}_3$ ,  $\text{Sr}_{1-x}\text{Y}_x\text{RuO}_3$ ,  $\text{SrTi}_{1-x}\text{Ru}_x\text{O}_3$ , and  $\text{YTi}_{1-x}\text{Ru}_x\text{O}_3$ , whereas 271 configurations have been sampled for their oxynitride ( $\text{ABO}_{2.875}\text{N}_{0.125}$ ) counterparts. Fig. 4.3 presents the 0 K formation enthalpy landscapes ( $\Delta H_f$  at 0 K) for these solid solutions.

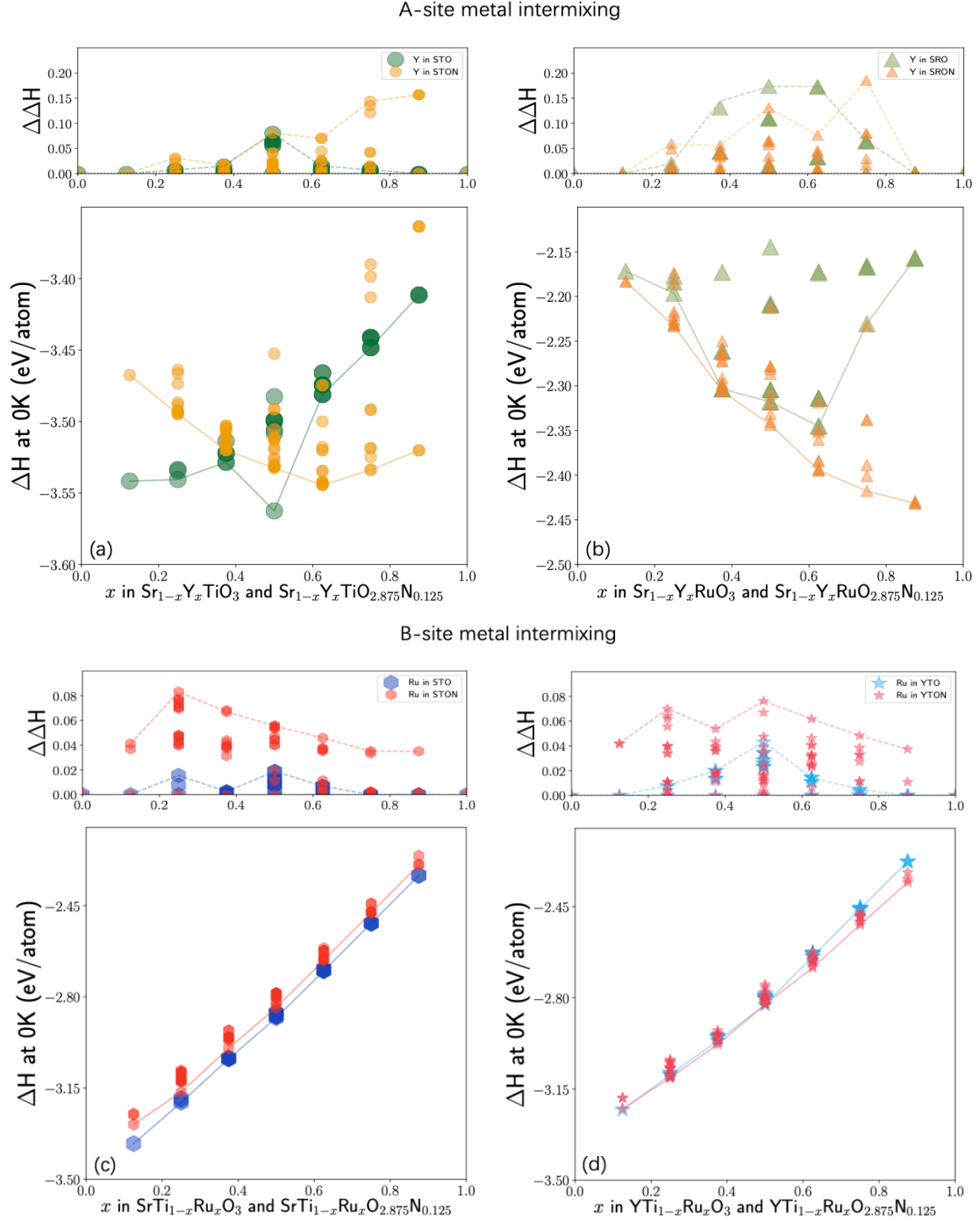


Fig. 4.3. The formation enthalpy ( $\Delta H_f$  at 0 K) landscapes for perovskite oxide and oxynitride solid solutions with metal intermixing.  $\Delta\Delta H_f$  is the enthalpy difference between a configuration to the one with the lowest formation enthalpy with the same chemical composition. The symbols connected by lines are configurations which have the lowest formation enthalpy with a given composition. The legend is the abbreviation of one metal intermixed in perovskite oxides or oxynitrides, eg. ‘Y in STO’ means yttrium intermixing in  $\text{SrTiO}_3$ .

As shown in Figure 4.3, all oxides and oxynitrides with A-/B- site metal intermixing have negative  $\Delta H_f$  at 0 K, indicating that they are stable compounds, in principle. First of all, it is obvious that A-site and B-site metal intermixing result in different formation enthalpy landscapes. For A-site intermixing [Fig. 4.3(a,b)],  $\Delta H_f$  show distinct nonlinear behavior, whereas for B-site intermixing [Fig. 4.3(c,d)], their  $\Delta H_f$  increase monotonically, demonstrating that they behave as a simple mixture with no significant electronic interactions between the two different B-site cations. This is fundamentally governed by the energy difference between perovskite oxides ( $\text{ABO}_3$ ) and perovskites nitrides ( $\text{ABN}_3$ ), showing that changing the chemical contents of B- site cation leads to more significant change in the formation enthalpies of perovskite oxides and oxynitrides. Secondly, for the A-site mixed  $\text{Sr}_{1-x}\text{Y}_x\text{TiO}_3$ , low Y mixing concentrations stabilize the perovskite oxides while the high mixing concentrations stabilize the oxynitrides [Fig. 4.3(a)]. It is particularly interesting to see in Fig. 3(b) that  $\Delta H_f$  for  $\text{Sr}_{1-x}\text{Y}_x\text{TiO}_{2.875}\text{N}_{0.125}$  decreases monotonically, but not for the pristine perovskite oxides. This can be understood from Table 1 that  $\text{YRuO}_3$  is the only compound that can decrease the formation enthalpy with the incorporation of N into the O site. However, such a stabilizing effect is not observed in B-site mixed  $\text{YRuO}_3$  or  $\text{YRuO}_{2.875}\text{N}_{0.125}$  [Fig. 4.3(d)]. Finally, to better highlight the large number of solid solution configurations that had been sampled at different metal intermixing concentrations, we also plotted the values of  $\Delta\Delta H_f = \Delta H_i - \Delta H_{\min}$ , in Fig. 3, where  $\Delta H_i$  is the formation enthalpy of each configuration at a given composition ( $i = 1, 2, 3, \dots$ ) and  $\Delta H_{\min}$  represents the lowest possible formation enthalpy at that composition. It also indicates how sensitive the formation energy is on the lattice positions of the cations,

which demonstrates that A-site cation intermixing results in a larger spread in  $\Delta\Delta H_f$  compared to the case of B-site cation intermixing, suggesting that the formation enthalpies are very sensitive to the local structural environment of the A-site cation. This is also reflected in Fig. 4.3(c,d) that the differences in  $\Delta H_f$  between oxide and oxynitride across all different B-site cation compositions are generally very small.

Finally, to better highlight the large number of solid solution configurations that had been sampled at different metal intermixing concentrations, we also plotted the values of  $\Delta\Delta H_f = \Delta H_i - \Delta H_{\min}$ , in Fig. 4.3, where  $\Delta H_i$  is the formation enthalpy of each configuration at a given composition ( $i = 1, 2, 3, \dots$ ) and  $\Delta H_{\min}$  represents the lowest possible formation enthalpy at that composition. It also indicates how sensitive the formation energy is on the lattice positions of the cations, which demonstrates that A-site cation intermixing results in a larger spread in  $\Delta\Delta H_f$  compared to the case of B-site cation intermixing, suggesting that the formation enthalpies are very sensitive to the local structural environment of the A-site cation. This is also reflected in Fig. 4.3(c,d) that the differences in  $\Delta H_f$  between oxide and oxynitride across all different B-site cation compositions are generally very small.

After establishing the formation enthalpy landscapes of mixed-cation perovskite oxides and their corresponding oxynitrides, we proceed to investigate their Gibbs formation free energies at the elevated temperatures. All subsequent discussions will be focusing on the lowest energy configurations of oxides/oxynitrides with a specific chemical composition [along the dashed lines in the plots shown in Fig. 4.3], this will give us the reaction free energies for interconverting between the most stable structures of a redox pair in the chemical looping, which will require the most energy input in an endothermic reaction.



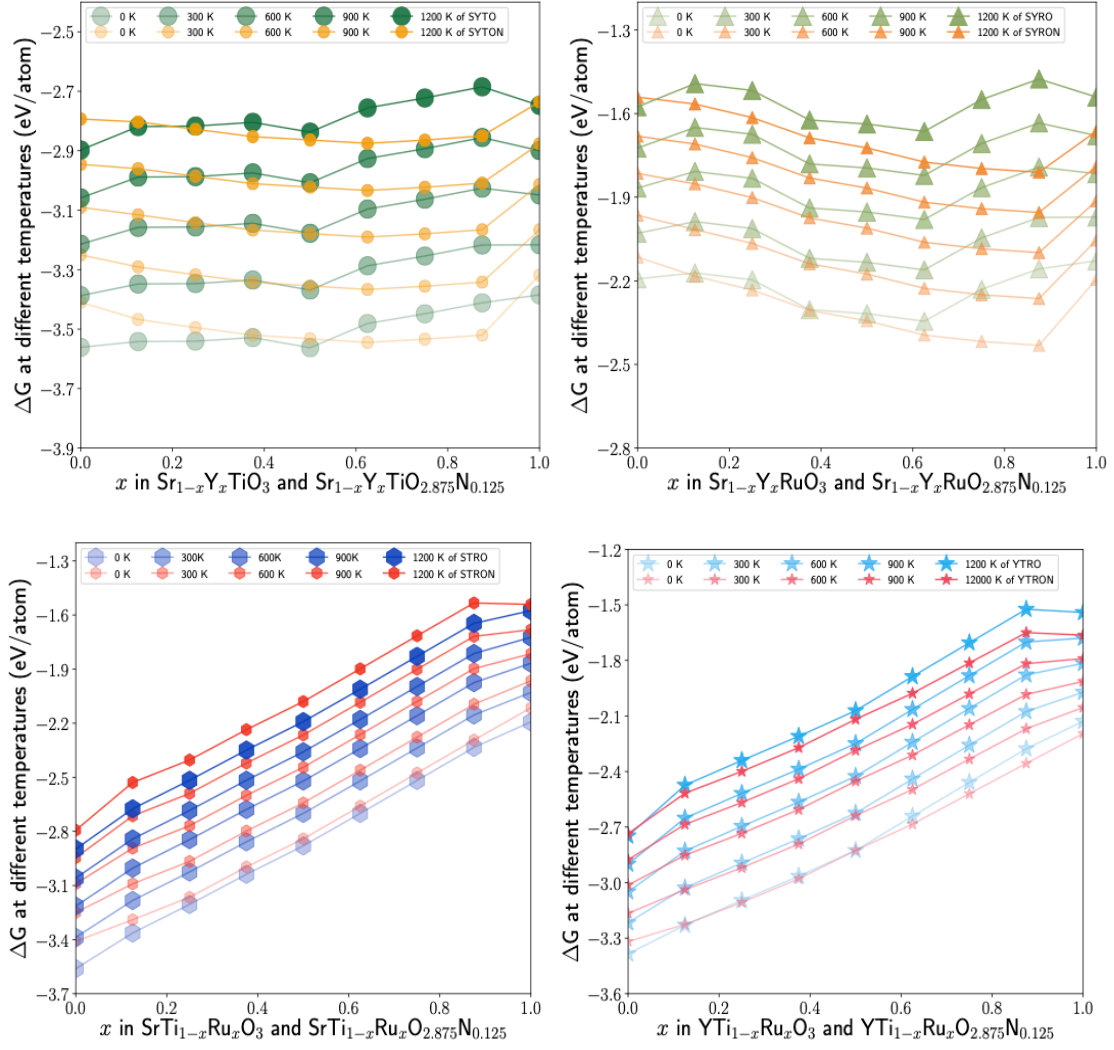


Fig. 4.4. Composition and temperature dependent Gibbs formation free energies of redox pairs. The temperature dependent Gibbs formation energies of the solid solutions are distinguished by the increasingly darker color from 0 K to 1200 K.

FIG. 4.4 plots the composition and temperature dependence of Gibbs formation energies for all compounds. It shows that their Gibbs formation energies increase with increasing temperature, which indicates temperature change is expected play a significant role in the thermodynamic driving force of STAS reactions. The dashed line for the formation enthalpies in Fig. 4.3 is observed to have a dominant effect in the composition dependent Gibbs formation free energies for cation-intermixed perovskite oxides and oxynitrides.  $\Delta G_f(T)$  in A-site cation intermixed systems shows mild composition dependency across all temperatures, whereas strong linear compositional

trend in  $\Delta G_f(T)$  for B-site cation intermixed systems can be observed. These are consistent with the behaviors of  $\Delta H_f$  shown in Fig. 43. Practically, the relative difference of  $\Delta G_f(T)$  for a pair of oxide/oxynitride at the same cation intermixing ratio (i.e. the redox pair) is of our fundamental interests for assessing the viability of the chemical looping process shown in Fig. 4.4. The result shows that, for most compounds, introducing extra thermal energies does not lead to a re-ranking in the relative stability between oxides and their oxynitrides across the entire compositional range, but the differences of  $\Delta G_f(T)$  between a redox pair increase with temperature. An exceptional case is  $\text{Sr}_x\text{Y}_{1-x}\text{TiO}_3$ , which critical concentration of yttrium required to stabilize its oxynitride decreases as temperature rises. It raises a question in whether such phenomenon is strongly originated from the cooperative effects between two different A-site cations, which may benefit them to act as redox pairs for TAS.

### **The effect of cation intermixing on the reaction Gibbs free energies**

To address this question, we use the formation free energies of the oxide/oxynitride pairs as determined to probe the reaction free energies for the nitridation and hydrolysis steps in the chemical looping based on the reactions (4.3) and (4.4) shown in the section of Methodologies. It is apparent from these two balanced equations that the formation free energy differences between the oxide/oxynitride redox pairs must compete with the relative stabilities of other gases ( $\text{H}_2$ ,  $\text{O}_2$  and  $\text{NH}_3$ ) as well as water in order to drive these processes to occur.

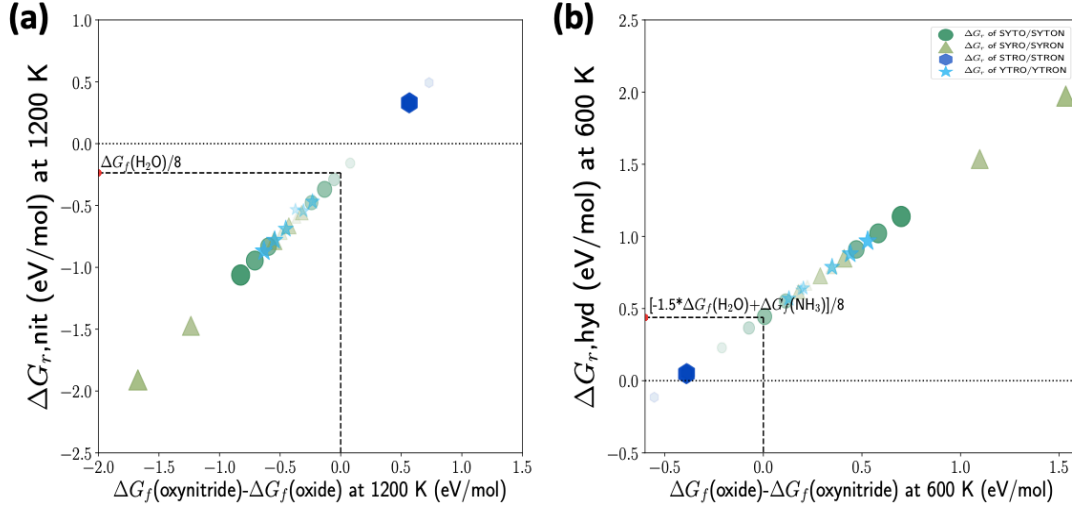


Fig. 4.5. Reaction free energies of nitridation (a) at 1200 K and hydrolysis (b) at 600 K in the STAS, using the stable oxide/oxynitride pairs obtained from thermodynamic screening (Fig. 4.4). The increasing metal intermixing concentrations ( $x$ ) are indicated by increasingly darker color and size of the markers. The dashed lines indicate the free energies for the competing reactions that oxide/oxynitride interconversion must overcome in order to make the overall reaction spontaneous, which is the reaction free energy at which the formation free energies for oxide and oxynitride are identical. For example, in (a), the free energy difference between oxynitride and oxide must be lower than the formation energy of water  $[\Delta G(\text{H}_2\text{O})/8]$  in order for the overall reaction to proceed.

To demonstrate this competing effect, we plot the free energies for the nitridation and hydrolysis reactions against the formation free energy differences between the reacting oxide/oxynitride pairs, which exhibits nice linear correlations between the two quantities in Fig. 4.5. As shown in Fig. 4.5(a), at 1200 K, most of the nitridation reactions can occur spontaneously except when Ru-incorporated  $\text{SrTiO}_3$  is used in the chemical looping, which is indicated by the negative values of  $\Delta G_{r,nit}$ . This is clearly driven by the higher thermodynamic stabilities of oxynitrides over oxides at 1200 K, in conjunction with higher thermodynamic stability (indicated by negative  $\Delta G$ ) of water compared to  $\text{N}_2$  ( $\Delta G_f = 0$ ). This is particularly true for the Y-rich  $\text{Sr}_{1-x}\text{Y}_x\text{RuO}_3$ , where their oxynitrides are the most stable ones (Fig. 4.3) across all materials screened here, the corresponding thermodynamic driving forces towards oxynitride formation are also the largest. It shows that a wider range of chemical compositions in  $\text{Sr}_{1-x}\text{Y}_x\text{RuO}_3$  allows

to be manipulated in the laboratory to facilitate the conjunct optimization of reaction condition for achieving the highest ammonia yield.

Next to  $\text{Sr}_{1-x}\text{Y}_x\text{RuO}_3$ , the performances of  $\text{Sr}_{1-x}\text{Y}_x\text{TiO}_3$  and  $\text{YTi}_{1-x}\text{Ru}_x\text{O}_3$  in the nitridation process are comparable to each other. From Fig. 4.5(b), it is also clear that almost all compounds with high Y or Ru contents are beneficial for breaking triple bonds in  $\text{N}_2$  by promoting the formation of oxynitrides. However, as shown in Fig. 4.5(b), when the oxynitride is too stable, it can inhibit the effective conversion back to oxide, which is essential for the formation of  $\text{NH}_3$  even when the reaction occurs at 600 K. This is fundamentally governed by how chemical looping operates [competing stabilities within a redox pair], as well as high endothermicity of converting  $\text{H}_2\text{O}$  to  $\text{NH}_3$  as indicate by the dash lines in Fig. 4.5(b). In this case,  $\text{Sr}_{1-x}\text{Y}_x\text{TiO}_3$  with low Y concentrations may be the most stable material to drive the TAS chemical loops because it shows close-to-zero reaction free energies for both nitridation and hydrolysis steps to ensure fast interconversion between oxide and oxynitrides. This is further supported by analyzing the cooperative effects induced by cation intermixing, which are discussed in the following section.

## Cooperative effects on cation intermixing redox pairs

In order to apply the concept defined in Eq. (4.7) in the section of Methodologies to study the possible existence of cooperative effects on the catalytic performance introduced by the cation intermixing, we first need to introduce the concept of limiting reaction, which is the reaction that has the highest reaction energy in the TAS cycle when a given redox pairs is used. It means that the free energy for the limiting reaction is  $\Delta G_{r,\text{lim}} = \max [\Delta G_{\text{hyd}}, \Delta G_{\text{nit}}]$ . Next, we define  $\Delta \Delta G_{r,\text{lim}} = \Delta G_{\text{AA}'\text{BO}_3}^{\text{lim}} - \min [\Delta G_{\text{ABO}_3}^{\text{lim}}, \Delta G_{\text{A}'\text{BO}_3}^{\text{lim}}]$  [which is equally applicable to  $\text{A}(\text{BB}')\text{O}_3$ ]. Physically,  $\Delta \Delta G_{r,\text{lim}} < 0$  corresponding to ‘cooperative enhancement effect’, meaning the cation intermixing is indeed beneficial to lower the thermodynamic barrier of the most

difficult catalytic step when the pure perovskite oxide is used as the catalyst. Fig. 4.6 shows the compositional-dependent of  $\Delta\Delta G_{r,\text{lim}}$  for all materials screened in this work.

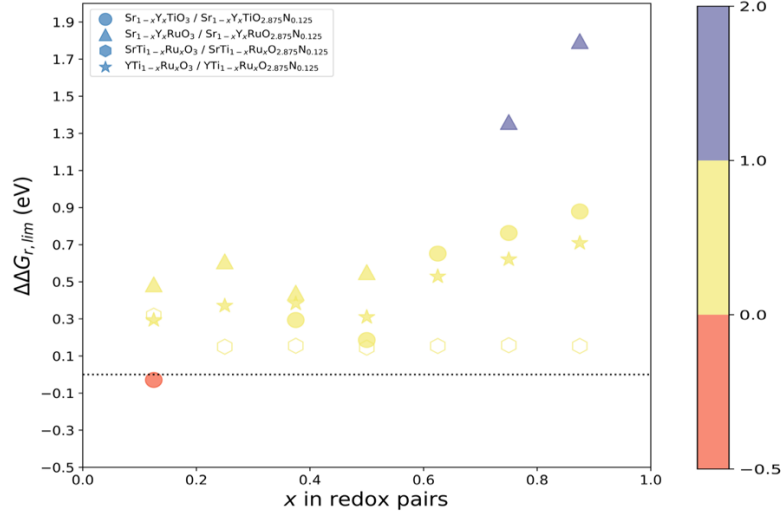


Fig. 4.6. Differences in the free energies for the limiting reactions when using the metal-intermixed redox pairs compared to the lowest reaction free energy of the same limiting step either one of the pure perovskites is involved ( $\Delta\Delta G_{r,\text{lim}}$ ). We distinguish the limiting reaction with the hollow (nitridation) and solid (hydrolysis) markers. The coloring scheme differentiate reactions that show cooperative enhancement ( $\Delta\Delta G_{r,\text{lim}} < 0$ ), weak anticooperative  $\Delta\Delta G_{r,\text{lim}} \in [0,1]$  and strong anticooperative  $\Delta\Delta G_{r,\text{lim}} > 1$  when metal-intermixed perovskites are used for driving the chemical looping of TAS processes.

For most compounds to be used as the active materials for TAS, it is found that the limiting reaction is the hydrolysis reaction, except for  $\text{SrTi}_{1-x}\text{Ru}_x\text{O}_3/\text{SrTi}_{1-x}\text{Ru}_x\text{O}_y\text{N}_{3-y}$ , in which the reaction is limited by the nitridation step. Fig. 6 shows that cooperative enhancement in the reactivity of the cation-intermixed perovskites as TAS redox pairs is rare.  $\text{Sr}_{0.875}\text{Y}_{0.125}\text{RuO}_3/\text{Sr}_{0.875}\text{Y}_{0.125}\text{RuO}_{2.875}\text{N}_{0.125}$  with high Sr concentrations shows anticooperative effects, this is because in these cases, oxynitride is much more stable than the oxide. As a result, the conversion of the oxynitride back to oxide in the limiting reaction (hydrolysis) is extremely difficult to proceed. In this case, the cation intermixing has exerted a negative effect on the performance of the cation-intermixed compound for TAS, compared to that of pure perovskites. For most redox pairs investigated here it is found from Fig. 4.6 that  $\Delta\Delta G_{r,\text{lim}}$  falls between 0 and 1 eV for

the majority cases, meaning that there is generally no distinctive thermodynamic advantages to use the cation-intermixed perovskites as redox materials for STAS. The notable exception is  $\text{Sr}_{0.875}\text{Y}_{0.125}\text{TiO}_3/\text{Sr}_{0.875}\text{Y}_{0.125}\text{TiO}_{2.875}\text{N}_{0.125}$ , which is the only compound, that shows a negative  $\Delta\Delta G_{r,\text{lim}}$ , i.e. cooperative enhancement effect. Nevertheless, it can be seen that the values of  $\Delta\Delta G_{r,\text{lim}}$  tend to be smaller when the concentrations of Y/Ru cations are in the diluted limit. Hence, we envisage that further lowering of the concentration of cation intermixing may lead to the discovery of even better perovskite-based redox materials for STAS. However, computationally, this would require the screening to be performed using much larger supercells, which is beyond the scope of the present investigation.

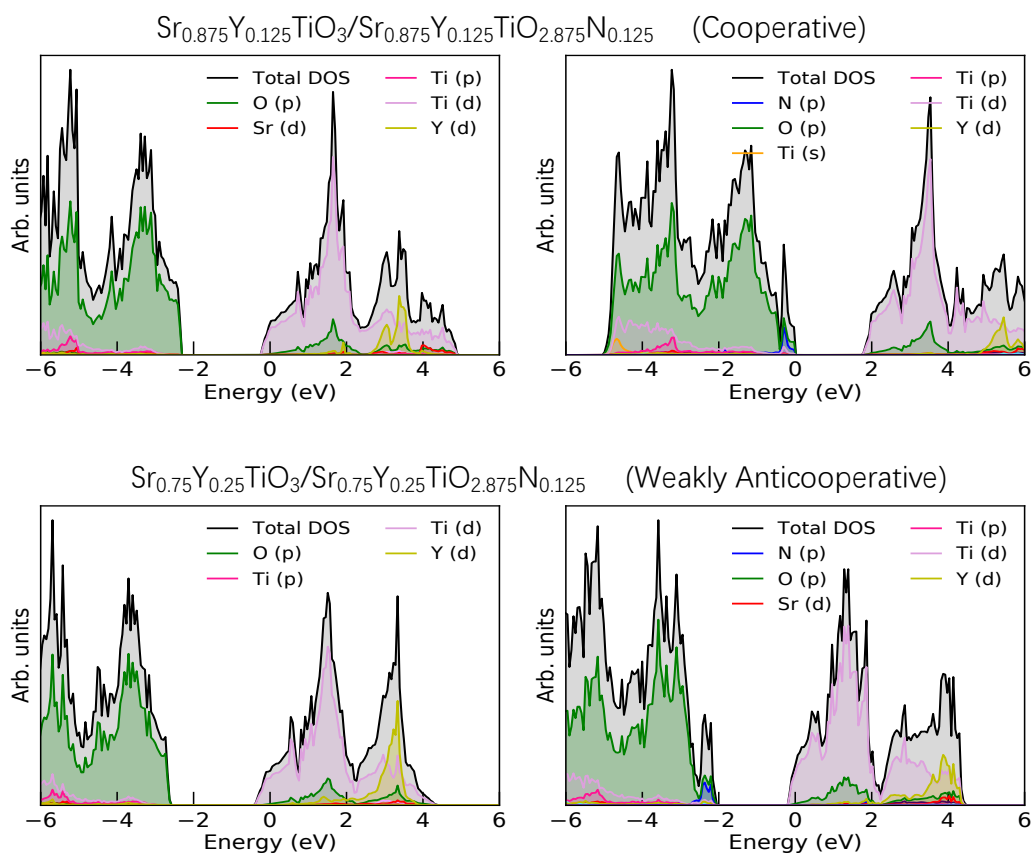


Fig. 4.7. Atom- and orbital-resolved electronic density-of-states for  $\text{Sr}_{0.875}\text{Y}_{0.125}\text{TiO}_3/\text{Sr}_{0.875}\text{Y}_{0.125}\text{TiO}_{2.875}\text{N}_{0.125}$  and  $\text{Sr}_{0.75}\text{Y}_{0.25}\text{TiO}_3/\text{Sr}_{0.75}\text{Y}_{0.25}\text{TiO}_{2.875}\text{N}_{0.125}$  redox pairs.

In order to gain some basic understanding on the possible mechanism that leads to the observed ‘cooperative’ effect, we resolve to the electronic structures of  $\text{Sr}_{0.875}\text{Y}_{0.125}\text{TiO}_3/\text{Sr}_{0.875}\text{Y}_{0.125}\text{TiO}_{2.875}\text{N}_{0.125}$  (cooperative) and  $\text{Sr}_{0.75}\text{Y}_{0.25}\text{TiO}_3/\text{Sr}_{0.75}\text{Y}_{0.25}\text{TiO}_{2.875}\text{N}_{0.125}$  (weak anticooperative) pairs. The calculated electronic density-of-states (DOS) at PBE level of theory for these materials are shown in Fig. 4.7. It can be seen from the left-hand-side of Fig. 4.7 that yttrium behaves as an *n*-type dopant in cubic  $\text{SrTiO}_3$ , which pins its Fermi level at the conduction band edge. Since the Y-*d* state contributes to extra conduction band states at around  $\sim 3$  eV, and the conduction band edge is predominately of Ti-3*d* character, it suggests that the extra electrons contributed by the Y-dopant occupy the 3*d* electronic states of multivariant Ti cation. Additional N-intermixing into  $\text{Sr}_{0.875}\text{Y}_{0.125}\text{TiO}_3$  and  $\text{Sr}_{0.75}\text{Y}_{0.25}\text{TiO}_3$  changes the electronic structures differently, whereby  $\text{Sr}_{0.875}\text{Y}_{0.125}\text{TiO}_{2.875}\text{N}_{0.125}$  converts back to an intrinsic semiconductor with Fermi level located at the valence band edge, but not for  $\text{Sr}_{0.75}\text{Y}_{0.25}\text{TiO}_{2.875}\text{N}_{0.125}$ . This shows that charge transfer between Y and N dopant occurs in  $\text{Sr}_{0.875}\text{Y}_{0.125}\text{TiO}_{2.875}\text{N}_{0.125}$  that may be the dominant electronic origin for the observed cooperative effects in the  $\text{Sr}_{0.875}\text{Y}_{0.125}\text{TiO}_3/\text{Sr}_{0.875}\text{Y}_{0.125}\text{TiO}_{2.875}\text{N}_{0.125}$  redox pair. Surprisingly, albeit the fact that N in  $\text{SrTiO}_3$  is directly bonded to the B-site Ti cation, there is little orbital interaction between the N-*p* state and Ti-*d* state, meaning that Ti-N interaction is unlikely to be playing the most critical role in facilitating the catalytic conversion from  $\text{N}_2$  to  $\text{NH}_3$ .

## 4.4 Conclusions

Compositional engineering of solid solutions is an important pathway to enhance the existing, as well as introduce new, functionalities in solids and it plays a critical role in developing thermal redox materials for ammonia synthesis with renewable energies as one of the feasible solutions for the hydrogen economy. However, there is pressing need to develop more concrete understanding on why such a strategy works. Here, we systematically investigated the temperature- and compositional-dependent TAS reaction thermodynamics of rare earth-metal-alloyed perovskite oxides by combining

random samplings, high-throughput DFT and machine-learning expedited free-energy calculations together with the concept of ‘cooperative enhancement’. We found that interconversion between perovskite oxides ( $\text{ABO}_3$ ) and their rarely explored, partially nitrated oxynitrides ( $\text{ABO}_{2.875}\text{N}_{0.125}$ ) is the most feasible pathway to drive TAS. In this work, we used Y/Ru-intermixed  $\text{SrTiO}_3/\text{SrTiO}_{2.875}\text{N}_{0.125}$ , which is of profound technological importance in modern material science, physics, and electronic engineering, as an example to reveal how stable oxides can be activated as redox materials through composition engineering. The results demonstrate that, on one hand, cation intermixing, in particular,  $\text{Sr}_{1-x}\text{Y}_x\text{RuO}_{2.875}\text{N}_{0.125}$  is the only system where the oxynitride is more stable than the oxide, making the nitridation of perovskites more favorable. On the other hand, effective generation of ammonia via hydrolyzing oxynitrides means the oxynitrides cannot be too stable. This is fundamentally required by the two competing reactions in the chemical looping process. As such, our screening suggests that  $\text{Sr}_{1-x}\text{Y}_x\text{RuO}_3/\text{Sr}_{1-x}\text{Y}_x\text{RuO}_{2.875}\text{N}_{0.125}$ , and  $\text{Sr}_{1-x}\text{Y}_x\text{TiO}_3/\text{Sr}_{1-x}\text{Y}_x\text{TiO}_3$  with low Y content can effectively balance the reaction free energies for both the nitridation and hydrolysis steps and they are the best redox materials for TAS in the as-investigated system. The competing nature of the chemical cycle also resulted in cooperative enhancements of the redox performances introduced by cation intermixing being rare in this case.

The present work has established a universal theoretical approach to dissect the role of complex compositional engineering in perovskites for designing advanced redox pairs for ammonia synthesis, which can also be applied to other synthetic chemical processes alike. On the methodological side, the Gibbs free energy descriptors are applied as originally formulated, to keep our conceptual framework simple. This has inevitably ignored two important contributions to the thermodynamic properties. The first one is the configurational entropies in solid solutions, which may further stabilize metastable reaction intermediates, particularly oxynitrides, thus lowering the reaction free energy. The second one is more specifically related to the perovskite, which is known to possess strong vibrational anharmonicities [103, 104]. As such, free-energy descriptor



developed based on quasiharmonic approximations will need to be further extended to achieve higher accuracy in predicting the free energies of perovskites[105]. Solving these problems is subjected to our future investigations to further advance high-throughput physics-inspired design of solid-state redox materials.

## Chapter 5 Reaction thermodynamic screening for the formation of perovskite oxynitrides

### 5.1 Introduction

ABO<sub>3</sub> perovskite is a versatile class of crystalline materials that can be adopted by a wide range of compounds. Perovskites have been intensively studied for a wide range of practical applications, such as perovskite light emitting diode LED, perovskite solar cell, and hydrogen storage, etc. Many innovative materials and creative concepts have been generated and proposed because of the exotic physical properties that exist in perovskites originated from the ubiquitous couplings among charge, spin and orbital degrees-of-freedom in these materials. In this regards, chemical substitutions will further change the electronic structures and chemical bonding in the materials significantly, that may further improve the physical properties of perovskites for different applications. So far, the majority of work on oxide perovskites have been concentrating on cationic substitutions on either A-site or B-site, whereas the investigations on the anionic sites are mainly focusing on the formation of oxygen vacancies, which can occur either randomly or as ordered structures (such as those in the renowned Brownmillerites ABO<sub>2.5</sub> structures [106]). However, investigations on perovskites with mixed anions are rare, and to-date, most studies on mixed anion perovskites focus on only a few elements which can substitute oxygen ions ( $r_{O^{2-}} = 1.4$  Å), such as fluorine ( $r_{F^{-}} = 1.3$  Å) and nitrogen ( $r_{N^{3-}} = 1.5$  Å). Substituting oxygen ions by larger anions often resulted in the formation of layered compounds such as Ruddlesden-Popper perovskites[107].

Nitrogen-substituted perovskites (including other multiple oxides) are usually named oxynitride. In 1986, Marchand et al. first proposed the perovskite oxynitrides[108]. The B-site of perovskite oxynitrides (ABO<sub>3-x</sub>N<sub>x</sub>) usually are main group metals like Mg, Al and early transition metals such as Mo, Nb, Ti, Ta, V, W and Zr. In terms of their

physical properties, the vast majority of perovskites oxynitrides are in a cubic crystal structure and exhibit bright colors, even though their corresponding perovskite oxides are usually black or colourless. These compounds are generally very stable against chemical decomposition at high temperature, even when treated with boiling aqua regia. Some of them will not decompose even when the temperature is increased to hundreds Celsius [109]. Due to their unique properties, perovskite oxynitride are used to produce inorganic pigments such as  $\text{CaTaO}_2\text{N}$  and  $\text{LaTaO}_2\text{N}$  [110]. In addition,  $\text{LaTiO}_2\text{N}$  is used as photocatalyst for water splitting [111]. In our previous work (Chapter 4) on perovskites for thermal ammonia synthesis, we investigated the potential of interconverting between four particular pairs of perovskite oxides and their perovskite oxynitride ( $\text{ABO}_{2.875}\text{N}_{0.125}$ ) as redox pairs during a two-step chemical looping for ammonia production. The key rationale behind this choice is the high energetic propensity to fully convert oxide perovskites into nitrides, which makes them poor as redox pairs, but partially converting the oxides into oxynitrides can be feasible. Till date, research in perovskites oxynitride is rather limited, and not many perovskite oxynitrides have been synthesized experimentally. Therefore, inspired by our previous work, there exists an urgency to further explore the structures, stabilities and physical properties of oxynitrides across a wide chemical space, particularly in the context of the present thesis, as redox intermediates for thermal ammonia synthesis.

Traditional material discoveries based on trial-and-error approach are both expensive and time consuming. With the continuous development of accurate computational methods, efficient numerical algorithms and increasingly available supercomputing powers, many new materials and their associated properties can be reliably predicted before they are synthesized in the laboratory. Hence, Density Functional Theory (DFT) based high-throughput computation screening for materials innovation has become pivotal in material research over the past decade [89, 112]. Simultaneously, many materials databases have also emerged such as Materials Project. The goal of materials project as a materials database is to use high-throughput calculation to predict the properties of the inorganic materials [42, 113], in the application of functional materials,

from electrodes, photocatalysts, photovoltaics to thermoelectric all benefit from this database[1, 114].

Comparing perovskite oxynitrides to oxides, due to nitrogen possible ordering, which will lead an additional degree of freedom in the structures, incorporation nitrogen into perovskite oxides result in a reduction of local symmetry of the cations[109]. With this, we combine high-throughput DFT-based modeling and Crystal Orbital Hamilton Population (COHP) to discover how nitrogen intermixing changes the chemical bondings in perovskite oxides and the correlations between the changes of chemical bondings and thermodynamical stabilities. A total of 430 cubic perovskite oxides ( $\text{ABO}_3$ ) are obtained from our previous work obtained by pymatgen, through configurational sampling, 430 perovskite oxynitrides ( $\text{ABO}_{2.875}\text{N}_{0.125}$ ) are generated. We systematically investigate their formation enthalpies according to lattice strains affected by different settings of structural relaxations, tolerance factors and chemical bonding.

## 5.2 Methodologies

### Structure sampling and DFT calculation

In this work, all perovskites are modelled in a  $2 \times 2 \times 2$  supercell containing 8 A-/B-site cations and 24 oxygen atoms in total. According to our previous research on solid solutions of mixed halide perovskites[95], we substitute one O with N in the perovskite lattice to generate the configurations of perovskite oxynitrides  $\text{ABO}_{2.875}\text{N}_{0.125}$ .

### DFT Calculations

All DFT calculations are performed by Vienna ab-initio Simulation Package (VASP)[75]. Exchange-correlation is approximated with the Perdew-Burke-Ernzerhof (PBE)[96] functional. The electron density are expanded with standard PAW (projector augmented wave method)[97], with energy cut-off of 400eV. Monkhorst-Pack[98]  $k$ -point sampling is set to  $6 \times 6 \times 6$  in the Brillouin zone for all structures.

Optimizations are terminated when the total energy between two electronic steps are smaller than  $2.5 \times 10^{-4}$  eV/Å. In this work, structural optimizations were performed with two different settings. In the first case, only the cell volume is optimized by preserving the  $Pm\bar{3}m$  symmetry of the system, whereas in the second case, all degrees-of-freedom (cell shape, volumes and atomic positions) are freely optimized. Comparing the results from these two optimizations will enable us to measure the degree of lattice strains introduced by N-intermixing in the perovskite oxides. The formation enthalpy  $\Delta H_f$  of the optimized structures is given by:

$$\Delta H_f^{Pm\bar{3}m}(ABO_3) = \frac{1}{N}[E_{ABO_3} - E_A - E_B - 3E_O] \quad (5.1)$$

for oxides, and

$$\Delta H_f^{Pm\bar{3}m}(ABO_{2.875}N_{0.125}) = \frac{1}{N}[E_{ABO_{2.875}N_{0.125}} - E_A - E_B - 2.875E_O - 0.125E_N] \quad (5.2)$$

for oxynitrides, where E represent the total energy of the corresponding compound or atom, N is the total number of atoms in the simulation supercell.

## Perovskites tolerance factor engineering

Tolerance factor was introduced by V.M. Goldschmidt in 1926, which is used to predict the stability of perovskite ( $ABO_3$ ) by using the ionic radii  $R_A$ ,  $R_B$  and  $R_O$ . The Goldschmidt tolerance factor can be calculated as:

$$t = \frac{[(R_A) + (R_O)]}{\sqrt{2}[(R_B) + (R_O)]} \quad (5.3)$$

when  $t > 1$ , the perovskites prefer to adopt either a hexagonal or tetragonal structure, because the A ion is too large or B ion is too small to adopt a close packed cubic structure. When  $0.9 < t < 1$ , the A ion and B ion are of ideal sizes for a cubic perovskite structures. When  $0.71 < t < 0.9$ , the preferred structure is either orthorhombic or rhombohedral, because the A ion is too small to fit into the B interstices. Finally, when  $t < 0.71$ , it means both the A ion and B ion have the same radii and the compound will tend to adapt a structure that is different from the ones mentioned above.

Under the assumption of ideal solid solution formation with randomly distributed dopants, we can calculate the tolerance factor of perovskite oxynitride ( $\text{ABO}_x\text{N}_{3-x}$ ) as:

$$t = \frac{[(R_A) + x(R_O) + (3 - x)(R_N)]}{\sqrt{2}[(R_B) + x(R_O) + (3 - x)(R_N)]} \quad (5.4)$$

## Crystal Orbital Hamilton Population

Crystal Orbital Hamilton Population (COHP) is a theoretical tool for analyzing the electronic band structures of solids, from which the nature of chemical bondings in a solid may be rationalized to facilitate the understanding of its chemical stabilities. By projecting the plane wave basis set onto the localized basis set, this tool divides the band-energy into orbital-pair interaction, which separates covalent interactions into bonding and antibonding contributions to illustrate the band-structure energy between two adjacent atoms in a given structure. Here, COHP analysis is performed to assess the chemical bonding characteristic change from perovskite oxides to perovskite oxynitrides whose perovskite oxynitrides possess more negative formation enthalpies. By analyzing the results of COHP to the bonding relationships between the structures which makes it possible to reveal why the perovskites oxynitrides may be even more stable than its parent oxides.

## 5.3 Results and discussion

### Thermodynamic stabilities of perovskite oxides and oxynitrides

The formation enthalpies,  $\Delta H_f$ , of the oxide and oxynitride are shown in FIG. 5.1 for all 430 pairs considered in our work. Here,  $\Delta H_f$  calculated for optimized structures with and without space group symmetry constraint are plotted separately in order to identify the possible (de)stabilization effects caused by the dopant-induced mechanical strains.

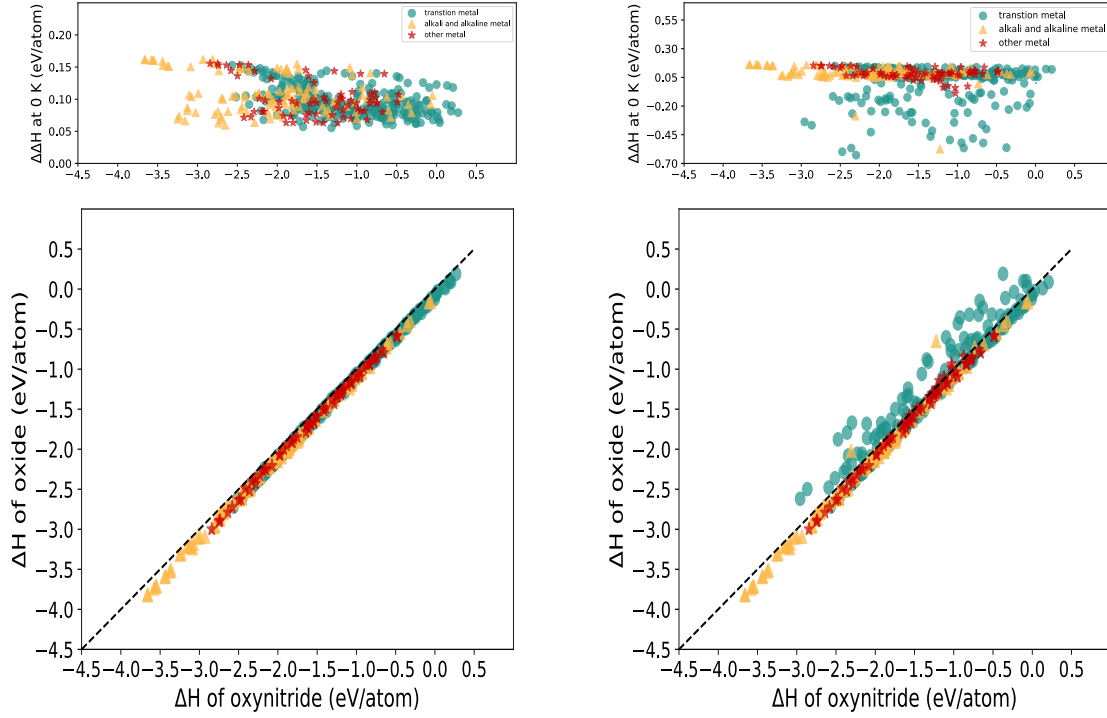


Fig. 5.1 The formation enthalpies  $\Delta H$  at 0 K, for perovskite oxides and oxynitrides. The left figure compares the  $\Delta H$  of structures relaxed under symmetry constraints, whereas the right figure corresponds to  $\Delta H$  calculated for fully relaxed structures.  $\Delta\Delta H$  is the enthalpy difference between an oxide and its corresponding oxynitride. The markers are categorized by the elemental identity of the A-site metal, being either the transition metal (green), alkali and alkaline metal (yellow), or others (red).

The formation enthalpy determines whether a given compound can thermodynamically exist in principle. As shown in Fig 5.1, most oxides and oxynitrides have negative  $\Delta H_f$  at 0 K, which suggest that they are enthalpically stable. First of all, it is clearly that the formation enthalpy landscapes are sensitive to how the atomistic structures are optimized. In Fig .5.1(a), the formation enthalpies of oxynitrides all fall below the dash line, which demonstrates that the oxides are all more stable than oxynitrides. However, in Fig. 5.1(b) it shows that, upon full structural optimization, most oxynitrides with A-site being the transition metal, becomes more stable than their corresponding oxides. To our knowledge, compared to the pure oxides, the possible ordering of oxygen atom and nitrogen atom in oxynitrides will lead to an additional degree-of-freedom. The

stability of the oxynitrides may be associated with that, due to extra degree-of-freedom, the structure will be unstable, which is to say the oxides should be more stable than the oxynitrides in principle. To the partially relaxation (pr) case (Fig. 5.1(a)), they followed this rule, but to the fully relaxation (Fig. 5.1(b)) case, there is a different picture, that is because different relaxation degree will lead to different total energy calculated by VASP, the greater the degree of relaxation, the more negative the total energy and the more stable the structure. According to VASP optimization, regardless the degree of optimization, it is a local minimization. Hence, for the cubic perovskite oxides, they are basically true local minimum, so even with further relaxation in all degree-of-freedom, their formation enthalpies almost unchanged. Whereas for the perovskite oxynitrides, partially relaxation can only land it onto a saddle point, which is approximately close to the local minimum of perovskite oxides. With further relaxation, it will go to their true local minimum state, their formation enthalpies will change with the relaxation degree. The formation enthalpies comparison between two different settings of structural relaxations are shown in Fig. 5.2.

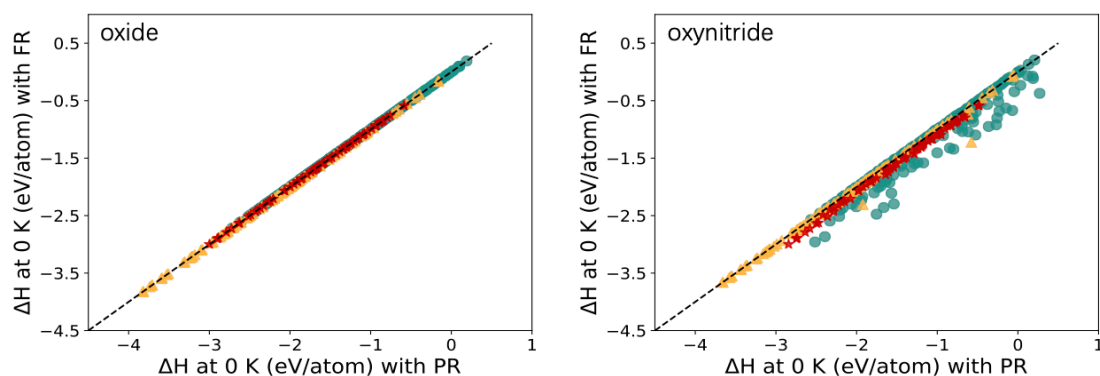


Fig. 5.2 The formation enthalpies of perovskite oxides and oxynitrides calculated with two different settings for structural relaxations. PR stands for partially relaxation, FR represents fully relaxation.

As shown in Fig. 5.2, for the perovskite oxides, their formation enthalpies basically maintained on the dotted line (function  $y = x$ ), which demonstrates full relaxation did not change the formation enthalpies much compared to constrained relaxation, this also proved our previous inference. For the oxynitrides, it is obviously that quite a few structures gained extra enthalpic stabilities upon full structural relaxation, and most of



these structures contain transition metals as the A-site cation. In addition, transition metal A-site perovskite oxides/oxynitrides have relatively less negative formation enthalpies than the other two kinds of perovskites whose A-site is alkali and alkaline metal or other metal. To understand this behavior, we first examine the relationship between the formation energies and the tolerance factors for perovskite oxides/oxynitrides to identify the possible geometric factors that govern their enthalpic stabilities.

### Relationships between tolerance factors and formation enthalpies of the perovskite oxides/oxynitrides

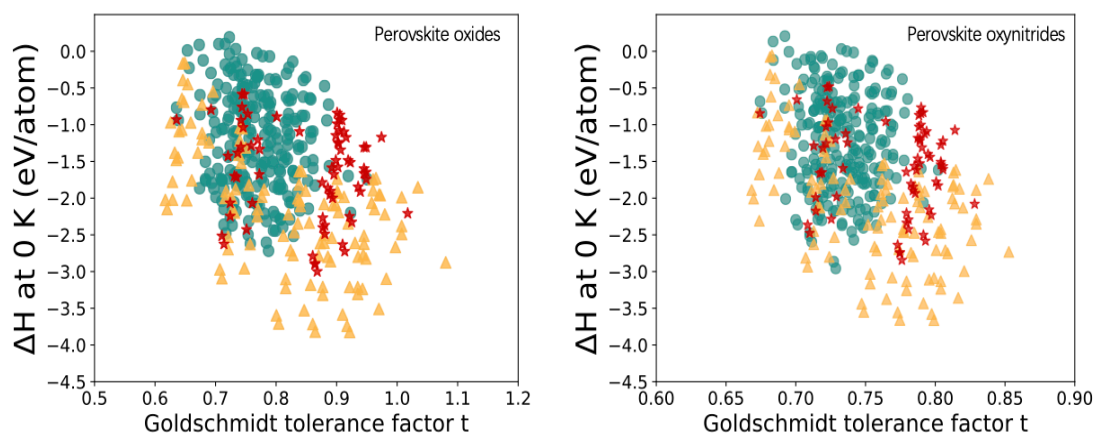


Fig. 5.3 Tolerance factors for all the 430 perovskite oxides and oxynitrides (optimized by fully relaxation) are shown as a function of their formation enthalpies at 0 K. The legend is the same as in the Fig. 5.1.

As Fig. 5.3 shows, it is obviously that there is a trend for the formation enthalpies to decrease as the tolerance factor increases, i.e. the formation enthalpy is relatively more negative when the compound possesses a larger tolerance factor. Generally, ions that will perfectly fit into a close-packed cubic perovskite will lead to a tolerance factor of 1.0, and any deviations from this value will lead to a distorted perovskite crystal

structure. If a structure distorts (has a small tolerance factor), it means that the cubic perovskite phase is less stable and will have a more positive formation energy. In Fig .5.3, for the structures which have close tolerance factor, for example, structures possess tolerance factor around  $0.9 < t < 1$ , they have distinct formation enthalpies, the largest formation enthalpy difference is near 3 eV/atom, their stabilities vary accordingly, and when it comes to structures which have close formation enthalpies, their tolerance factors are also different, which demonstrates the relationship between the tolerance factor and formation enthalpy is uncertain. Additionally, from our data analysis, we found when using the eq.(5.3) to calculate tolerance factor of perovskite oxides,  $t = 0.71$  is a turning point. Perovskite oxides which have tolerance factors smaller (larger) than 0.71, the tolerance factors for their corresponding perovskite oxynitrides increases (decreases). Combining Figs. 5.2 and 5.3, here, for perovskite oxynitrides whose A-site is transition metal, we plot their formation enthalpies and corresponding tolerance factor in Fig. 5.4, in order to find out if perovskite oxynitrides which have more negative formation enthalpies than their corresponding perovskite oxides is caused by the change in the tolerance factor.

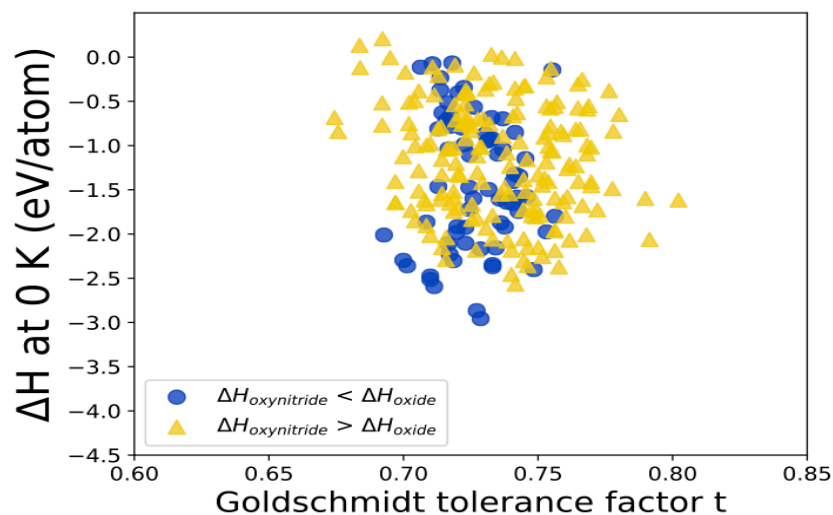


Fig. 5.4 The formation enthalpies of the perovskite oxynitrides whose A-site is transition metal. The tolerance factors are calculated for oxynitrides.

As shown in FIG. 5.4, perovskite oxynitrides which have smaller formation enthalpies than their corresponding perovskite oxides are marked blue. For these structures, the tolerance factors for the perovskite oxides are approximately between 0.68 and 0.77. There is no obvious critical tolerance factor at which perovskite oxynitrides become more stable than their corresponding perovskite oxides, or vice versa. This shows that simple geometric measure of crystal packing efficiency (i.e. the tolerance factor), is insufficient to determine the thermodynamic stabilities of perovskite oxides/oxynitrides. In this case, one needs to resolve to the electronic structures of the materials, from which the electronic characteristics of their chemical bonding that subsequently determines their material stabilities, can be better understood. This is the focus of the next section.

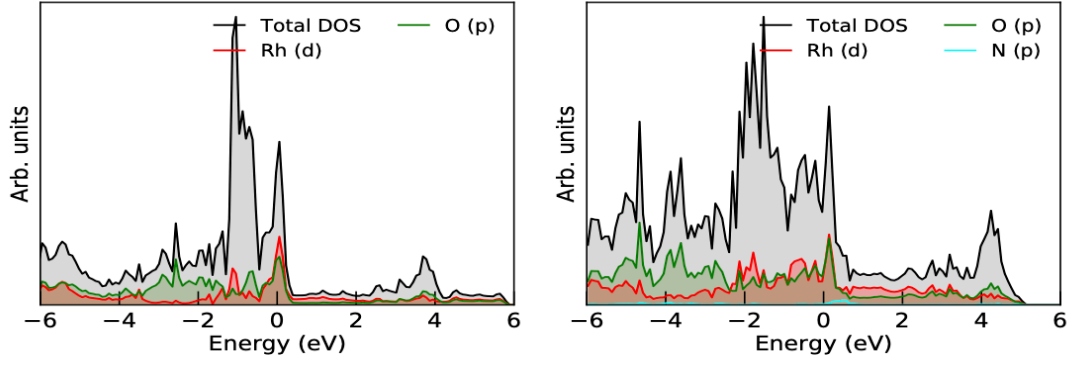
## Theoretical study of electronic structures and chemical bonding change

Since perovskite oxide/oxynitride pairs which have more stable perovskite oxynitrides are almost structures with A-site as transition metals. Through our analysis, there are 243 pairs of perovskite oxides and perovskite oxynitrides whose A-site are transition metal. 68 out of their perovskite oxynitrides have more negative formation enthalpies than their corresponding perovskite oxides. Hence, here, we examine the electronic structures of 3 pairs of oxides and oxynitrides (list in Table 5.1), where the oxynitride is more stable than its oxide with relative low, medium, and high difference of formation energies, in order to understand the origins behind the observed trends of thermodynamic stabilities.

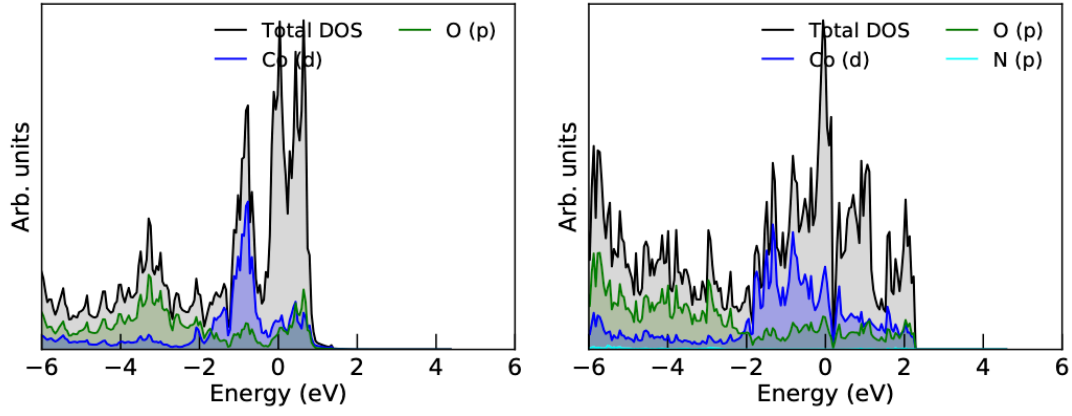
Types	$\Delta H_{f,ABON}(0\text{ K})$	$\Delta H_{f,ABO}(0\text{ K})$
CuRhO <sub>3</sub> /CuRhO <sub>2.875</sub> N <sub>0.125</sub>	-0.566	-0.467
CrCoO <sub>3</sub> /CrCoO <sub>2.875</sub> N <sub>0.125</sub>	-1.042	--0.700
ZnZrO <sub>3</sub> /ZnZrO <sub>2.875</sub> N <sub>0.125</sub>	-2.513	-2.363

Table 5.1. The formation enthalpies of the chosen 3 perovskite oxides and perovskite oxynitrides.

(a) DOS of  $\text{CuRhO}_3$  and  $\text{CuRhO}_{2.875}\text{N}_{0.125}$



(b) DOS of  $\text{CrCoO}_3$  and  $\text{CrCoO}_{2.875}\text{N}_{0.125}$



(c) DOS of  $\text{ZnZrO}_3$  and  $\text{ZnZrO}_{2.875}\text{N}_{0.125}$

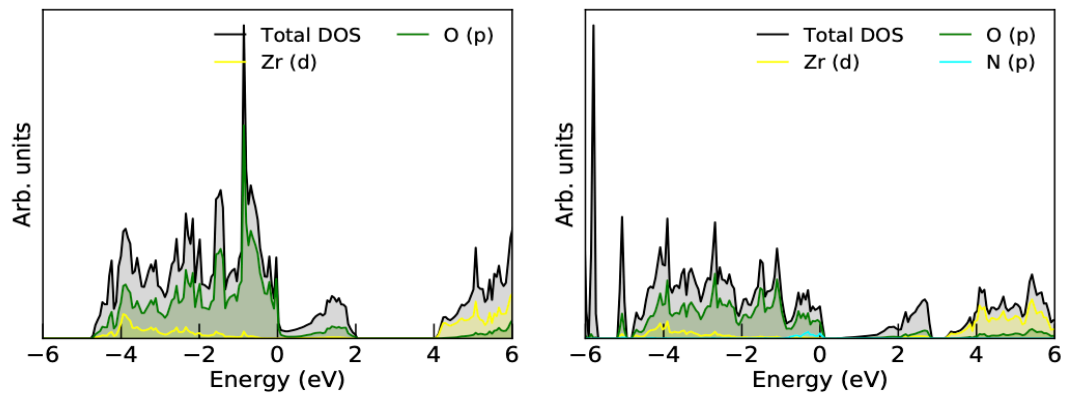
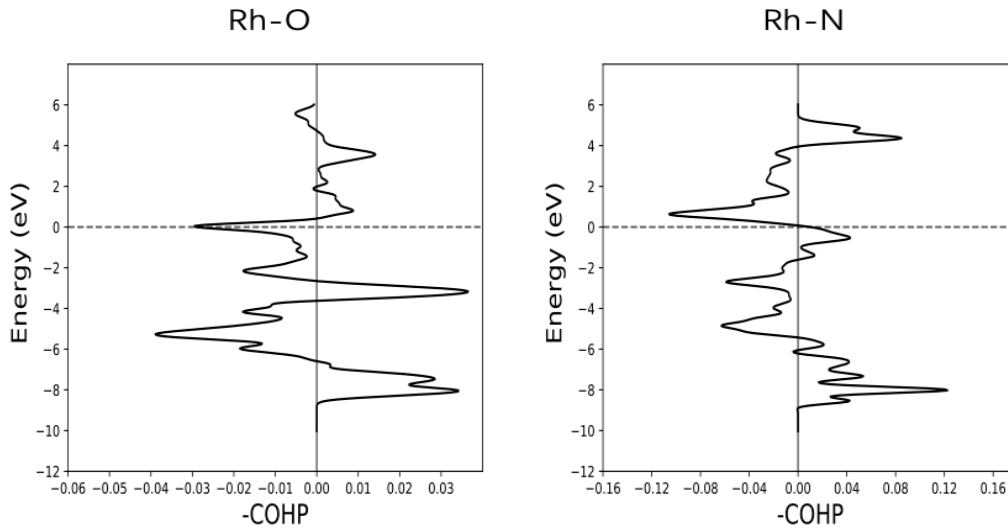


Fig .5.5 Atom- and orbital-resolved electronic density of states for  $\text{CuRhO}_3/\text{CuRhO}_{2.875}\text{N}_{0.125}$ ,  $\text{CrCoO}_3/\text{CrCoO}_{2.875}\text{N}_{0.125}$  and  $\text{ZnZrO}_3/\text{ZnZrO}_{2.875}\text{N}_{0.125}$ . Here, we plot dos of the B-site, oxygen, and nitrogen which are directly involved in bonding.

As Fig. 5.5 shows, from the top (a) and middle (b) panels, the electronic structures of these two perovskite oxides/oxy-nitride pairs do not show obvious band gaps, which illustrates these two pairs show metallic conductivity. However, for the bottom panel (c), the Fermi level for  $\text{ZnZrO}_3$  is located in the valence band, from which we conclude it is a p-type semiconductor. Upon the incorporation of N, forming  $\text{ZnZrO}_{2.875}\text{N}_{0.125}$ , the Fermi level becomes pinned at the valence band edge, which converts it into an intrinsic semiconductor. It can be seen the conduction band are predominately of B-site-3d character, which suggests the extra electrons contributed by the O occupy the 3d electronic states of B-site element cations. From the right-hand side of Fig. 5.5, since there is only one nitrogen atom in the structures, it doesn't have significantly contribution to the density of states. Combining Table 5.1, although there is little orbital interaction between the B-site-d state and N-p state, the difference between formation enthalpies of  $\text{CrCoO}_3$  and  $\text{CrCoO}_{2.875}\text{N}_{0.125}$  are relatively high, so the N-p state overlaps more with Co-d state, for the other two pair, according to their formation enthalpies difference, their orbital interaction between the N-p state and B-site-d are comparatively subtle.



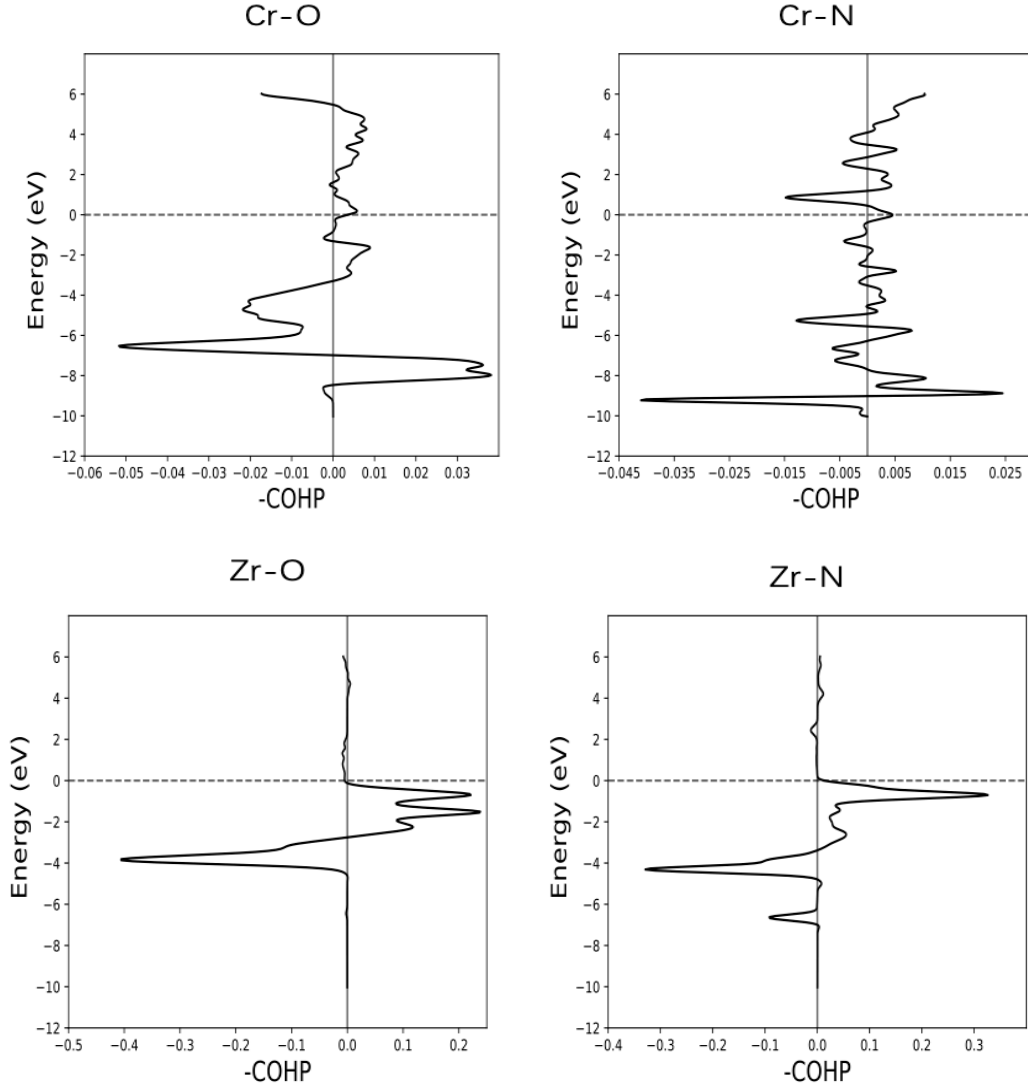


Fig .5.6 Crystal Orbital Hamilton Population (COHP) for the metal-O bond and metal-N bond (the B-site metal connected to the O atom which is replaced by N in the structure sampling) for the three pairs of perovskites oxide/oxynitride. The Fermi level is given as the energy zero, bonding and antibonding interactions are given by COHP spikes to the right/left.  $-p\text{COHP} < 0$  indicates antibonding interaction,  $-p\text{COHP} > 0$  stands for bonding interaction[115].

Through our structure sampling, one nitrogen atom replaced one oxygen atom in a  $2 \times 2 \times 2$  supercell. Here, we systematically investigate the bonding difference between O/N and B-site metal. Combining the density of state of each structure in Fig .5.5 and COHP of each structure in Fig .5.6, we found for the  $\text{CrCoO}_3$  and  $\text{CrCoO}_{2.875}\text{N}_{0.125}$ , due to the overlaps between N-p state and Co-d state are relatively

large, in the right-hand of Fig .5.6, their COHP peaks show in both bonding and antibonding states densely. Moreover, their stabilizing bonding interactions are stronger than the destabilizing interactions. For the other two pairs, the overlaps between N-p state and B-site-d state are small, their COHP peaks are sparsely, the stabilising bonding interactions are cancelled out by the destabilising ones. Hence, the difference of formation enthalpies between  $\text{CrCoO}_3$  and  $\text{CrCoO}_{2.875}\text{N}_{0.125}$  are larger than the other two pairs. In addition, for  $\text{ZnZrO}_3/\text{ZnZrO}_{2.875}\text{N}_{0.125}$ , there cation-anion interactions are predominantly bonding character, which explains why they have the most negative formation enthalpies among the three perovskite oxide/oxyntiride pairs. For the other two pairs, their bonding interactions are weaker compared to  $\text{ZnZrO}_3/\text{ZnZrO}_{2.875}\text{N}_{0.125}$ , which results their formation enthalpies are comparatively less negative.

## 5.4 Conclusion

Perovskite oxynitrides highly attracted the attention of scientists both for their structural challenge and physical/chemical properties. Due to the difficulties in synthesis of perovskite oxynitrides, with the help of high-performance computer simulation, scientists are endowed with great opportunities to investigate perovskite oxynitrides before they are synthesized experimentally to explore their properties. Here we systematically investigated the relationships between the formation enthalpies and lattice strains influenced by two different relaxation degree, tolerance factors and chemical bonding of 430 pairs of perovskites oxide/oxyntiride. We found different relaxation degree will lead to different lattice strains, which will affect the formation enthalpies of the perovskite oxide/oxyntiride. When it comes to fully relaxation, some perovskite oxynitrides (most of them are structures contain transition metal as A-site) gain extra enthalpic stabilities, this is caused by further relaxation, it will go to their true local minimum state. In addition, we investigate formation enthalpies and corresponding tolerance factor of each structures, through our analysis, we found there

is no distinct clue which shows the relation between the tolerance factor and the thermodynamic stabilities of the perovskite oxynitrides. Furthermore, we evaluated the density of state and chemical bonding of the pairs which have more negative perovskite oxynitrides, our analysis suggests if the N-d state has more overlaps with the B-site-d state, the difference of the formation enthalpies between a given pair will become larger, which means the perovskite oxynitrides are more stable than the corresponding perovskite oxides. Here, we conclude some perovskite oxynitrides contain transition metal as the A-site are thermodynamically stable than their perovskite oxides, the stability are mainly influenced by the interactions between the nitrogen atom and B-site atoms.

In this present work, it gives a theoretical approach to investigate nitrogen-intermixing perovskites, we distinguish the perovskites by their A-site element, actually in perovskite oxides (oxynitrides) the oxygen (nitrogen) atoms are directly connected to the B-site atom, in our future work, we will focus more on the effects of B-site element of the properties of perovskite oxides/oxynitrides. Additionally, for the 430 perovskite oxides/oxynitrides pairs, we can thermodynamically investigate their performance as active materials for solar thermal ammonia synthesis in our future work, which we will discuss in the next chapter.



## **Chapter 6 High-throughput screening of perovskites as active materials for solar thermal ammonia synthesis**

### **6.1 Introduction**

In the past decades, ammonia has been widely used as a chemical or precursor to manufacture various products. After nearly one hundred years of development, industrial ammonia production is quite mature now, and is currently based on the Haber–Bosch cycles, combining  $\text{N}_2$  and  $\text{H}_2$  at high temperatures and pressures and using Fe-based alloys as catalysts to yield ammonia[79]. However, 1–2% of the world’s annual energy production is used to obtain the two elemental precursors, hydrogen and nitrogen, and a large amount of  $\text{CO}_2$  is generated during the process. Hence, alternative ammonia synthesis methods that avoid the shortcomings of the traditional Haber–Bosch process are needed. Recently, thermochemical redox cycles have promoted the synthesis of renewable chemicals at an atmospheric pressure using solar thermal energy, turbine engines, geothermal energy, or waste heat from thermal power plants as sources of high-temperature heat. One such application is STWS, which produces  $\text{H}_2$  from steam without catalysts in a two-step chemical-looping process. In a previous study, researchers first reduced one metal oxide with high oxygen exchange capacity at a high temperature to generate oxygen vacancies, which were filled with steam in the second oxidation step to generate hydrogen[31]. Using the STWS as a reference, STAS has been proposed as a potential strategy for green ammonia production, using thermal redox materials to generate  $\text{NH}_3$  in two- or three-step chemical looping.

Since its development, research related to STAS has continued to evolve. So far, most studies have focused on exploring binary metal oxides with low Gibbs reaction energies for interconversion to their corresponding metal nitrides as redox pairs. However, only 35 pairs of binary oxides/nitrides have proven to be feasible redox pairs for STAS because of the sparse number of metal nitrides with experimental Gibbs formation

energies. To overcome such limitations, DFT-based, high-throughput computational screening has become crucial in discovering new materials and predicting material properties. Yet calculating the formation enthalpies of binary metal oxides/nitrides at 0 K is challenging. Moreover, when calculating the temperature-dependent free energies of formation, a large number of additional calculations are required because of entropic contributions from phonon vibrations. Bartel *et al.* thus developed a descriptor using machine learning [41] to predict the Gibbs formation energies based on the DFT-calculated formation enthalpies. Thus, even if the number of Gibbs formation energies of metal nitrides obtained experimentally is small, those of thousands of metal nitrides or other inorganic crystalline solids can be obtained quickly and accurately by relying upon the descriptor. In their study, Bartel *et al.* used a descriptor to assess the thermodynamic feasibility of 1148 binary metal oxides/nitrides as redox pairs for STAS[91], and found that only redox pairs based on B, Ce, Fe, and V show promising potential for STAS. However, the discovery of more promising redox pairs with other compositions is urgently needed.

A recent study by Michalsky and Steinfeld focused on perovskites ( $ABO_3$ )[116], where A and B sites are metal cations in 12- and 6-coordinated interstices of the metal oxide. Electronic structure calculations to evaluate the stability and surface activity of oxygen vacancies demonstrated that perovskite redox energetics can be tuned by their compositions. Structures containing Co or Mn at the surface and Co doped with Mo or W in bulk are promising redox materials for STAS, such as  $CaCoO_3$ -terminated  $La_{0.5}Ca_{0.5}Mo_{0.5}Co_{0.5}O_3$ ,  $SrCoO_3$ -terminated  $Sr_{0.5}La_{0.5}Co_{0.5}W_{0.5}O_3$ , and  $CaMnO_3$ -terminated  $Sr_{0.5}Ca_{0.5}MnO_3$ . In addition, our previous research on metal intermixing perovskite oxides/oxy-nitrides for use as redox materials for STAS showed that one A-site perovskite pair,  $Sr_{0.875}Y_{0.125}TiO_3/Sr_{0.875}Y_{0.125}TiO_{2.875}N_{0.125}$ , demonstrated a slight cooperative enhancement relative to the pristine perovskite structures of  $SrTiO_3/SrTiO_{2.875}N_{0.125}$  and  $YTiO_3/YTiO_{2.875}N_{0.125}$  in reducing the limiting reaction energy in a two-step chemical-looping process. Perovskites are promising materials for fuel cells, high-temperature oxygen separation, and solar-driven thermochemical

splitting of CO<sub>2</sub> and H<sub>2</sub>O[117-119], for example, because of their stable crystal phase, tunable oxygen vacancy concentrations, and high conductivities owing to oxygen vacancies.

However, studies on perovskites as redox materials for STAS are still lacking. In light of the aforementioned progress, in this chapter, we apply DFT-based structural sampling, high-throughput DFT calculations, and the Gibbs formation energy machine-learning descriptor to obtain  $\Delta G_f(T)$  to systematically investigate the performance of 430 perovskite oxides/oxynitrides as redox pairs for STAS. By evaluating the Gibbs formation energies, reaction energies, and limiting reaction energies, we conclude that one of the 430 perovskite oxides/oxynitrides redox pairs, BeTiO<sub>3</sub>/BeTiO<sub>2.875</sub>N<sub>0.125</sub>, is the most promising active material for STAS. In addition, we assess the reliability of the descriptor by comparing it with the phonon-based QHA to calculate the Gibbs free energy. We find that the descriptor shows a high accuracy when compared to the QHA.

## 6.2 Methodologies

### Structure sampling and DFT calculation

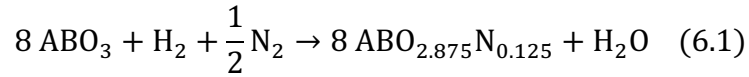
In this work, we used 430 perovskite oxide/oxynitride pairs, which were modelled using a  $2 \times 2 \times 2$  supercell containing a total of 8 A-/B-site cations and 24 X-site anions. In our previous research on intermixing perovskite oxides/oxynitrides for STAS, we found that perovskite oxynitrides ABO<sub>y</sub>N<sub>3-y</sub> with  $3-y = 0.125$  are the only structures viable for structural sampling because most perovskite oxynitrides become unstable as the stoichiometry of N increases. Therefore, in this study, we generated perovskite oxynitrides in the same way to form ABO<sub>2.87</sub>N<sub>0.125</sub> structures. In total, 860 solid-state configurations (430 perovskite oxides and 430 perovskite oxynitrides) were sampled in this study.

Both the atom positions and lattice parameters are fully relaxed by VASP[75] with the exchange–correlation energy approximated by the Perdew–Burke–Ernzerhof functional[96]. The electron densities were expanded using the standard projector augmented wave method (PAW)[97], and the energy cut-off for the PAW pseudopotential was set to 400 eV. Monkhorst–Pack  $k$ -point sampling was set to  $6 \times 6 \times 6$  in the Brillouin zone for all structures. Optimisations were terminated when the total energy change between two ionic steps was lower than  $2.5 \times 10^{-4}$  eV/atom.

## Two-step chemical looping in STAS

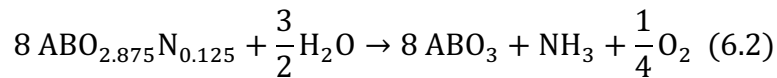
In this project, STAS is a two-step process. The first step is a nitridation reaction at high temperatures (1200–1800 K) to convert perovskite oxide to its corresponding perovskite oxynitride by exposure to  $N_2$  and reducing agent  $H_2$ :

1. Nitridation reaction:



Then, a hydrolysis reaction at 600–1200 K follows to hydrolyse the perovskite oxynitride back to the perovskite oxide and thus yield ammonia:

2. Hydrolysis reaction:



To evaluate the viability of each STAS reaction, we must obtain the Gibbs formation energies of the products and reactants.

## Calculation of the Gibbs formation energies

Through DFT calculations and using the total energy of each optimised structure, the formation enthalpy  $\Delta H_f$  is calculated with respect to its constituent atoms. For example,

Perovskite oxides:

$$\Delta H_f[\text{ABO}_3] = E[\text{ABO}_3] - E[\text{A}] - E[\text{B}] - \frac{3}{2}E[\text{O}_2] \quad (6.3)$$

Perovskite oxynitrides:

$$\Delta H_f[\text{ABO}_{2.875}\text{N}_{0.125}] = E[\text{ABO}_{2.875}\text{N}_{0.125}] - E[\text{A}] - E[\text{B}] - \frac{2.875}{2}E[\text{O}_2] - \frac{0.125}{2}E[\text{N}_2] \quad (6.4)$$

where  $E$  represents the total energy of the corresponding compound or atom. All the  $\Delta H_f$  values in this work are normalised by the total number of atoms in the structure.

After we obtain the formation enthalpies of all the structures, the temperature-dependent Gibbs formation energies  $\Delta G_f(T)$  can be calculated as refs[3], [4] by integrating the descriptor. The  $\Delta G_f$  for materials in the gaseous phase are obtained from FactSage[99]; the  $\Delta G_f$  of  $\text{H}_2$ ,  $\text{N}_2$ , and  $\text{O}_2$  are zero by definition.

## Calculation of reaction free energies

We can evaluate the reaction energies of each reaction in the STAS process by using the results of the Gibbs formation energy calculations. Analysis of the reaction energies will help us determine whether a given redox pair is suitable for STAS. The reaction energies are calculated as follows:

$$\Delta G_r(T) = \sum_i^{\text{products}} v_i \Delta G_{f,i}(T) - \sum_i^{\text{reactants}} v_i \Delta G_{f,i}(T) \quad (6.5)$$

where  $v_i$  is the stoichiometry of species  $i$ , which indicates that 1 mol of ammonia is generated in one complete reaction cycle.

## 6.3 Results and discussions

## Gibbs formation energies of redox materials

The Gibbs formation energies of the 430 redox pairs are shown as a function of temperature in Fig. 6.1. One of the essential requirements for a given redox pair to be viable for the STAS process is that the redox materials must possess negative Gibbs formation energies – that is, they have to be stable at the current reaction temperature. To our knowledge, negative Gibbs formation energy is an insufficient condition to determine the stability of one structure, and decomposition energy[101, 102] also plays an important role here. However, in our work, the thermodynamic evaluation relies on reaction free energies, which are directly calculated from Gibbs formation energies. As such, we chose Gibbs formation energies to judge the stability of the redox pairs. As shown in Fig. 6.1, most  $\Delta G_{f,ABO}(T) < \Delta G_{f,ABON}(T)$  where  $\Delta G_{f,ABO}(T)$  values fall below the  $y = x$  dashed line, except for the redox pairs whose A-sites are transition metals, of which some have a more negative  $\Delta G_{f,ABON}(T)$ . In addition, the difference in Gibbs formation energies between one redox pair is relatively subtle because, in our structural sampling process, we only replace one O by N in the supercell; therefore, when we calculate the formation enthalpies using Equations 6.3 and 6.4, the value difference is small.

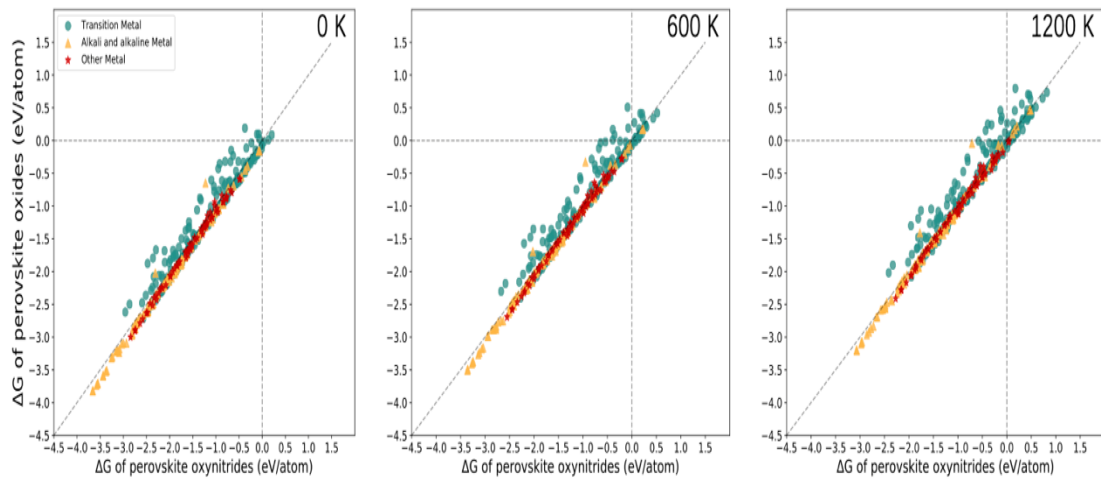


Fig. 6.1. Gibbs formation energies of each perovskite oxides/oxynitrides redox pairs with temperature increasing from 0 K to 600 K then 1200 K. The legends of the markers are distinguished

by the A-site metal of the redox pairs, transition metal (green), alkali and alkaline metal (yellow), and other metal (red).

Moreover, temperature has a critical influence on the Gibbs formation energies: when the temperature is 0 K, only eight pairs of perovskite oxide/oxy-nitride have a positive  $\Delta G_f$ . As the temperature increases, this number increases to 28 pairs at 600 K and 65 pairs at 1200 K. Furthermore, the Gibbs formation energy of each structure also increased, illustrating that the active materials became more unstable. In total, 377 pairs of redox materials (88 %) satisfied the condition that they have a negative  $\Delta G_f$  at 0 K, 600 K, and 1200 K. After obtaining the Gibbs formation energies of the redox pairs, we analyse their thermodynamic performance for STAS by calculating their reaction energies in chemical looping.

## Reaction thermodynamic assessment

In our two-step STAS process, the perovskite oxide and perovskite oxy-nitride mutually convert cyclically to yield ammonia. Both reactions are directly affected by the Gibbs formation energies of the reactants and products; however, only the reaction energy is negative, and the reaction can occur spontaneously. Hence, a systematic evaluation of the reaction energies will help us to identify promising redox pairs for this process. From Equations 6.1 and 6.2, it is clear that, during the reaction, the Gibbs formation energy differences of the redox pairs compete with the formation energies of  $\text{NH}_3$  and  $\text{H}_2\text{O}$  at the reaction temperature. Here, we plot the reaction energies against the Gibbs formation energy differences of each reacting redox pair shown in Fig. 6.2 to investigate the competing effects.

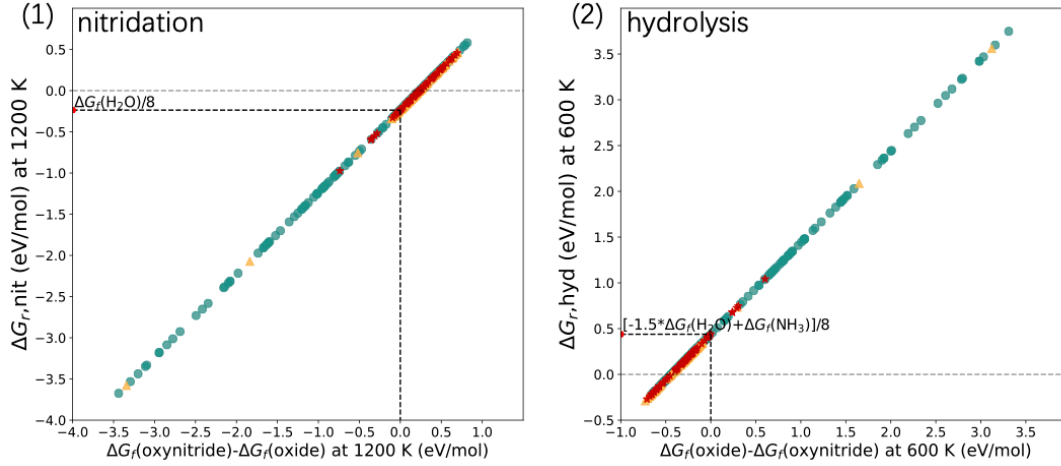


Fig. 6.2. Reaction energies of nitridation (1) and hydrolysis (2) at 1200 K and 600 K in the STAS process. Reaction energies and the Gibbs formation energies are normalised at 1 mol redox pairs per reaction. The dashed lines represent the free energies for the competing reactions, which the conversion between the redox pairs must exceed to make the reaction energies negative. The legend is the same as in Fig. 6.1.

For the nitridation reaction at 1200 K, 112 out of 430 redox pairs (26 %) had a negative  $\Delta G_{r,nit}$ , indicating that the conversion from perovskite oxide to perovskite oxynitride is thermodynamically more favourable than the formation of water.  $\Delta G_f(\text{H}_2\text{O}) = -0.189$  eV/mol at 1200 K, and this value changed to -0.236 eV/mol when we normalised the reaction energies as per mol redox pairs per reaction, indicating that if  $\Delta G_f(\text{oxynitride}) - \Delta G_f(\text{oxide}) < -0.236$ , the nitridation reaction will occur spontaneously. As shown in Fig. 6.2(1), most of the redox pairs that satisfy this condition are transition metal A-site perovskite oxides/oxynitrides, which is in line with the results shown in Fig. 6.1 because for the transition metal A-site perovskite redox pairs, the oxynitrides typically have more negative  $\Delta G_f$  than their corresponding oxides, which promotes nitrogen fixation. Once the nitridation step has been completed, the hydrolysis reaction occurs at 600 K. To the best of our knowledge,  $\Delta G_f(\text{H}_2\text{O}) < \Delta G_f(\text{NH}_3)$  at any temperature, thus thermodynamically guarantees that the reaction occurs spontaneously. Moreover, the conversion from oxynitrides to oxides should occur more easily than in the Gibbs formation energy difference between  $\text{H}_2\text{O}$  and  $\text{NH}_3$ ; 351 out of 430 redox pairs (82 %)



possess negative  $\Delta G_{r,hyd}$ . Separate analysis of each reaction in the STAS process reveals the relationship between the  $\Delta G_f$  and  $\Delta G_r$ . However, some of the redox pairs may meet the criteria for one reaction, but not the other. We found that only 33 out of 430 redox pairs fulfilled the requirements of the competing effects for both reactions. Here we list the 33 redox materials with their reaction energies in Table 6.1.

TABLE 6.1 The 33 redox materials which fulfilled the requirements of the competing effects for both nitridation and hydrolysis reaction.

Redox materials	$\Delta G_{r,hyd}$ (eV/mol)	$\Delta G_{r,nit}$ (eV/mol)
BeCrO <sub>3</sub> /BeCrO <sub>2.875</sub> N <sub>0.125</sub>	0.251	-0.275
BeIrO <sub>3</sub> /BeIrO <sub>2.875</sub> N <sub>0.125</sub>	0.299	-0.302
BeMnO <sub>3</sub> /BeMnO <sub>2.875</sub> N <sub>0.125</sub>	0.255	-0.257
BeMoO <sub>3</sub> /BeMoO <sub>2.875</sub> N <sub>0.125</sub>	0.259	-0.277
BeReO <sub>3</sub> /BeReO <sub>2.875</sub> N <sub>0.125</sub>	0.338	-0.339
BeRhO <sub>3</sub> /BeRhO <sub>2.875</sub> N <sub>0.125</sub>	0.265	-0.274
BeRuO <sub>3</sub> /BeRuO <sub>2.875</sub> N <sub>0.125</sub>	0.322	-0.339
BeTcO <sub>3</sub> /BeTcO <sub>2.875</sub> N <sub>0.125</sub>	0.307	-0.314
BeWO <sub>3</sub> /BeWO <sub>2.875</sub> N <sub>0.125</sub>	0.255	-0.265
CaReO <sub>3</sub> /CaReO <sub>2.875</sub> N <sub>0.125</sub>	0.343	-0.251
CaWO <sub>3</sub> /CaWO <sub>2.875</sub> N <sub>0.125</sub>	0.347	-0.263
CrReO <sub>3</sub> /CrReO <sub>2.875</sub> N <sub>0.125</sub>	0.329	-0.264
CrRuO <sub>3</sub> /CrRuO <sub>2.875</sub> N <sub>0.125</sub>	0.298	-0.252
CrWO <sub>3</sub> /CrWO <sub>2.875</sub> N <sub>0.125</sub>	0.299	-0.242
GeReO <sub>3</sub> /GeReO <sub>2.875</sub> N <sub>0.125</sub>	0.335	-0.253
GeWO <sub>3</sub> /GeWO <sub>2.875</sub> N <sub>0.125</sub>	0.400	-0.329
MgOsO <sub>3</sub> /MgOsO <sub>2.875</sub> N <sub>0.125</sub>	0.348	-0.286
MgWO <sub>3</sub> /MgWO <sub>2.875</sub> N <sub>0.125</sub>	0.330	-0.269
MnOsO <sub>3</sub> /MnOsO <sub>2.875</sub> N <sub>0.125</sub>	0.322	-0.241

PbOsO <sub>3</sub> /PbOsO <sub>2.875</sub> N <sub>0.125</sub>	0.422	-0.245
PdIrO <sub>3</sub> /PdIrO <sub>2.875</sub> N <sub>0.125</sub>	0.408	-0.299
PdMoO <sub>3</sub> /PdMoO <sub>2.875</sub> N <sub>0.125</sub>	0.359	-0.279
PdNbO <sub>3</sub> /PdNbO <sub>2.875</sub> N <sub>0.125</sub>	0.349	-0.264
PdTaO <sub>3</sub> /PdTaO <sub>2.875</sub> N <sub>0.125</sub>	0.418	-0.310
PdVO <sub>3</sub> /PdVO <sub>2.875</sub> N <sub>0.125</sub>	0.392	-0.325
PtOsO <sub>3</sub> /PtOsO <sub>2.875</sub> N <sub>0.125</sub>	0.413	-0.281
PtVO <sub>3</sub> /PtVO <sub>2.875</sub> N <sub>0.125</sub>	0.328	-0.247
SnCoO <sub>3</sub> /SnCoO <sub>2.875</sub> N <sub>0.125</sub>	0.411	-0.286
SnReO <sub>3</sub> /SnReO <sub>2.875</sub> N <sub>0.125</sub>	0.422	-0.270
TiFeO <sub>3</sub> /TiFeO <sub>2.875</sub> N <sub>0.125</sub>	0.377	-0.314
TiGeO <sub>3</sub> /TiGeO <sub>2.875</sub> N <sub>0.125</sub>	0.401	-0.341
VTcO <sub>3</sub> /VTcO <sub>2.875</sub> N <sub>0.125</sub>	0.353	-0.285
ZnIrO <sub>3</sub> /ZnIrO <sub>2.875</sub> N <sub>0.125</sub>	0.387	-0.267

Nevertheless, as shown in Fig. 6.2(1), some redox pairs have a negative  $\Delta G_r$ , but they are not in the area framed by the dashed line; similarly, as shown in Fig. 6.2(2), although some dots are inside the dashed line, they have positive  $\Delta G_r$ . These figures demonstrate that the competing effects are not sufficient to determine whether a given redox pair is viable for STAS, which prompted us to use investigate reaction energies.

## Analysis of limiting reactions

In the discussion of the reaction free energies of each step in the previous chapter, it is clear that a more comprehensive descriptor is needed to find suitable redox pairs for STAS. Here, we introduce the concept of a limiting reaction. The limiting reaction is that with the highest reaction free energy in a multi-step reaction process. In this study, we define the limiting reaction as  $\Delta G_{r,\text{lim}} = \max [\Delta G_{r,\text{hyd}}, \Delta G_{r,\text{nit}}]$  for one redox pair

in the chemical looping if  $\Delta G_{r,\text{lim}} < 0$ , which ensures that all the reactions occur spontaneously. The limiting reaction energies are plotted in Fig. 6.3.

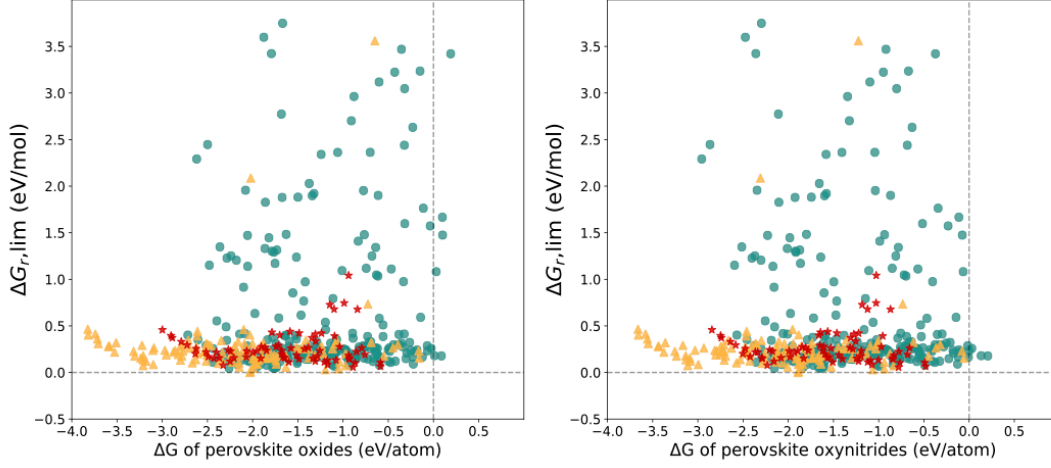


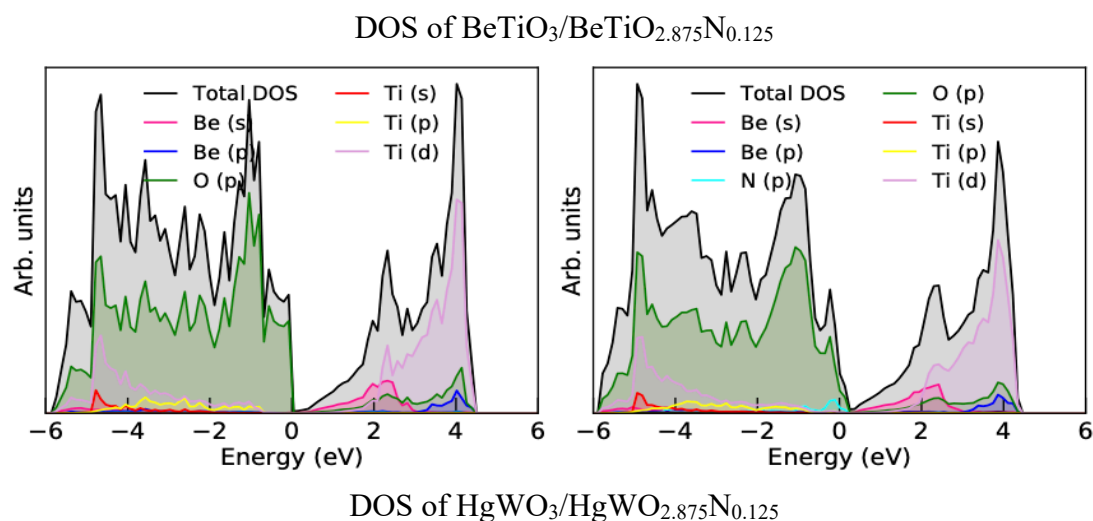
Fig. 6.3. Limiting reaction energies in STAS with respect to the  $\Delta G_f$  at 0 K of perovskite oxides (left) and perovskite oxynitrides(right). The legend is the same as Fig. 6.1.

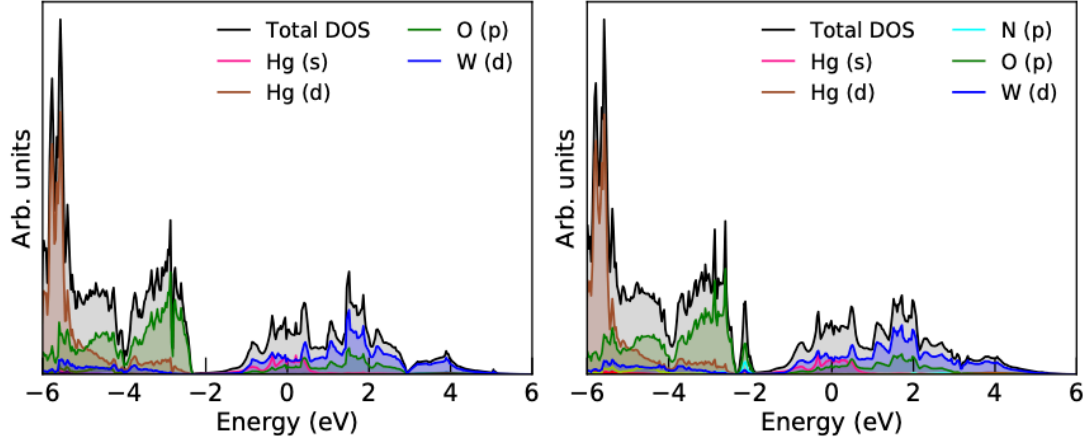
For 312 out of 430 redox pairs (72 %), the limiting reaction was the hydrolysis reaction. The hydrolysis step is thermodynamically challenging because of two essential factors. Firstly, the notably energetically uphill formation of  $\text{NH}_3$  from  $\text{H}_2\text{O}$  is stronger than the uphill from oxynitrides to oxides; 79 out of 312 (25 %) redox pairs have a more negative  $\Delta G_{f,ABON}(T)$  at 600 K. Secondly, although the interconversion of redox pairs is thermodynamically more downhill than the uphill from  $\text{NH}_3$  to  $\text{H}_2\text{O}$ , their hydrolysis reaction energies occur less easily than their nitridation reaction – 233 out of 312 (75 %) redox pairs fit this condition. For redox pairs that have a more negative  $\Delta G_{f,ABO}(T)$ , the limiting reaction of most is the nitridation reaction. As shown in Fig. 6.3, almost no redox pairs have negative limiting reaction energies, except for one yellow triangle with  $\Delta G_{f,ABO}(0\text{ K}) \sim -2\text{ eV/atom}$ , and  $\Delta G_{f,ABON}(0\text{ K}) \sim -1.9\text{ eV/atom}$ . Through data analysis, we found that they belong to one redox pair,  $\text{BeTiO}_3/\text{BeTiO}_{2.875}\text{N}_{0.125}$ , the limiting reaction energy is  $-0.0016\text{ eV}$ . To our knowledge, using  $\text{BeTiO}_3/\text{BeTiO}_{2.875}\text{N}_{0.125}$  as thermal redox materials has not been reported, and no other properties on the  $\text{BeTiO}_3/\text{BeTiO}_{2.875}\text{N}_{0.125}$  have also been reported literatures. Since the main goal of this thesis is to employ a DFT-based high-throughput thermodynamics analysis to search for promising

redox pairs for thermal ammonia synthesis, the discussions on other promising properties related to this pair of materials is beyond the scope of the present thesis. Hence, based on the above discussions, we regard  $\text{BeTiO}_3/\text{BeTiO}_{2.875}\text{N}_{0.125}$  as a promising perovskite redox pair for STAS.

## Electronic structure analysis of representative redox pairs

To obtain a better understanding of the reason why a given redox pair may be a promising active material for STAS, we conduct PBE-level calculations to obtain the electronic density of states of the three redox pairs for the STAS process:  $\text{BeTiO}_3/\text{BeTiO}_{2.875}\text{N}_{0.125}$ ,  $\text{HgWO}_3/\text{HgWO}_{2.875}\text{N}_{0.125}$ , and  $\text{MnZrO}_3/\text{MnZrO}_{2.875}\text{N}_{0.125}$ , which are suitable, unsuitable, and very unsuitable, respectively, according to their limiting reaction energies. The density of states of these three redox pairs is shown in Fig. 6.4.





DOS of  $\text{MnZrO}_3/\text{MnZrO}_{2.875}\text{N}_{0.125}$

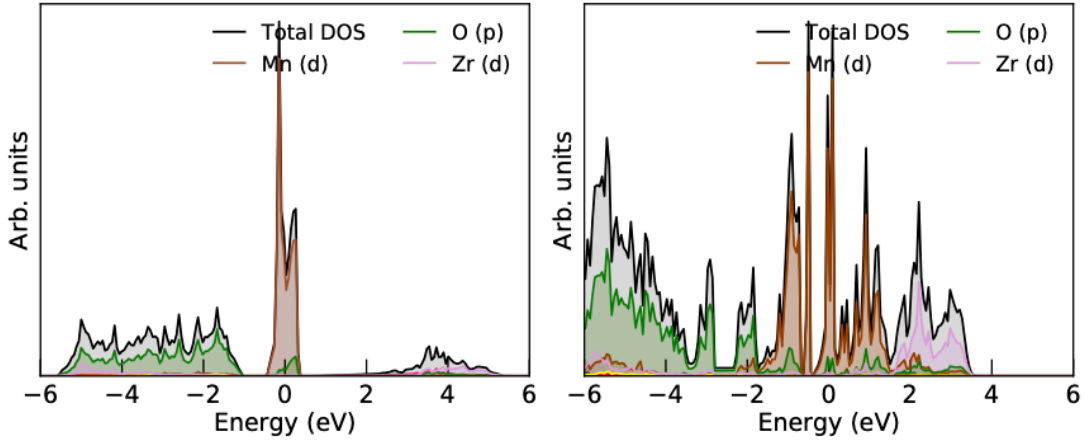


Fig. 6.4 Atom- and orbital-resolved electronic density of states in  $\text{BeTiO}_3/\text{BeTiO}_{2.875}\text{N}_{0.125}$ ,  $\text{HgWO}_3/\text{HgWO}_{2.875}\text{N}_{0.125}$ , and  $\text{MnZrO}_3/\text{MnZrO}_{2.875}\text{N}_{0.125}$  redox pairs.

Here, it can be seen in the top panel that  $\text{BeTiO}_3/\text{BeTiO}_{2.875}\text{N}_{0.125}$  are P-type semiconductors, where the conduction band edge is predominantly Ti-3d, Be-2s, and Be-2d states that contribute to extra conduction band states at approximately 2 eV and 4 eV. Around the Fermi level, the DOS of  $\text{BeTiO}_3$  shows a distinctive slope, and the valence and conduction bands are connected, which demonstrates its strong metallicity. With N-intermixing into  $\text{BeTiO}_3$ , it pins the slope to the conduction band edge. However, N-intermixing had no obvious effect on the distribution of electrons in each orbital. The middle panel showing  $\text{HgWO}_3/\text{HgWO}_{2.875}\text{N}_{0.125}$  demonstrates the Fermi level located in the conduction band, which shows these are N-type semi-conductors.

The distinctive slope located in the valence band around -2.2 eV, due to substitution of N, and it pins the slope to -2 eV. In  $\text{MnZrO}_3/\text{MnZrO}_{2.875}\text{N}_{0.125}$ , as the bottom panel of the figure shows, when N is intermixed in the perovskite oxide, the electronic structure shows a notable change.

In conclusion, the formation enthalpy differences between the corresponding redox pairs become smaller from  $\text{BeTiO}_3/\text{BeTiO}_{2.875}\text{N}_{0.125}$  to  $\text{HgWO}_3/\text{HgWO}_{2.875}\text{N}_{0.125}$  to  $\text{MnZrO}_3/\text{MnZrO}_{2.875}\text{N}_{0.125}$ , until the latter has a more negative formation enthalpy than  $\text{MnZrO}_3$ . Combined with the density of states of these three redox pairs, we determined that N-intermixing in different perovskites has different effects on the electronic structure. If it has a subtle effect on the electronic structure, the formation enthalpy of the perovskite oxynitrides will change relatively less; however, if it has a significant effect on the electronic structure, the formation enthalpy will vary.

### **Comparison of the machine-learned descriptor and quasiharmonic approximation (QHA)**

For 427 out of the 430 perovskite oxides, 7686 Gibbs free energies were calculated by QHA and the descriptor from 100 K to 1800 K. The results are shown in Fig. 6.5.

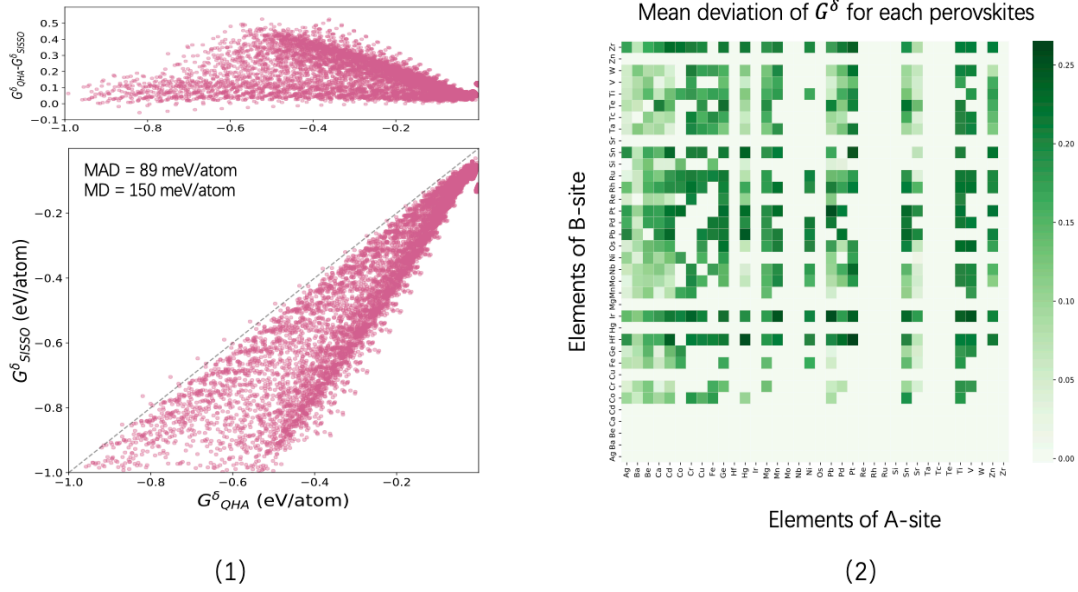


Fig. 6.5 Benchmarking descriptor against QHA. (1). Comparison of the descriptor to QHA for 427 perovskites. (2). A map of mean deviation of  $G^{\delta}$  for each perovskite.

We compared the results of  $G^{\delta}$  calculated by QHA and the descriptor to determine the relationship between them. As shown in Fig. 6.5(1), the descriptor agrees well with the values calculated by QHA, with a mean absolute deviation of 89 meV/atom, and for most perovskites, there is an underestimation of QHA-calculated  $G^{\delta}$  compared to the descriptor i.e.  $G^{\delta}(QHA) < G^{\delta}(SISSO)$ . However, the underestimation is relatively small (100 to 500 meV/atom), and the mean deviation of underestimation is 150 meV/atom. Through our data analysis, we found that, no matter which calculation method is used, as temperature increases,  $G^{\delta}$  has a trend of becoming more negative. That is shown in the top panel of Fig. 6.5(1), where the distribution of dots presents the shape of a mountain, thus illustrating that the  $G^{\delta}$  deviation between the descriptor and QHA is small when temperature is at low or high temperatures, but relatively larger for the medium temperatures. In Fig. 6.5(2), we map out the mean deviation of  $G^{\delta}$  for each perovskite, all of which are concentrated in the range of 0–250 meV/atom. Notably, for both methods, several factors contribute to the deviations, such as DFT functional, approximation anharmonic vibrations, calculated  $\Delta H_f$ , and configurational entropies. Hence, because the deviations of  $G^{\delta}$  between the descriptor and QHA are subtle and

have little effect on calculating the Gibbs formation energies, we conclude that the descriptor is reliable.

## 6.4 Conclusion

Solar thermal ammonia synthesis is a promising method of producing ammonia and, as such, has attracted the attention of researchers. This chapter describes how we used materials, random structure, density functional, and machine-learning descriptors to screen the thermodynamic feasibility of 430 perovskite oxides/oxy-nitride redox materials for use in STAS. Using DFT and descriptors, we obtained the Gibbs formation energies of these redox pairs. Then, using both, we calculated the reaction energies during chemical looping and established that there were limiting reaction energies with respect to the perovskite oxides and oxynitrides. Our screen thus suggests that  $\text{BeTiO}_3/\text{BeTiO}_{2.875}\text{N}_{0.125}$  is the only promising redox pair for STAS because it has negative limiting reaction energies during the process, which guarantees that the reactions can occur spontaneously. In addition, we compared the  $G^\delta$  calculated by the machine-learning descriptor and QHA to determine the reliability of the descriptor. According to our analysis, the  $G^\delta$  calculated by these two methods agreed well despite some subtle deviations. As such, it is practical to use the descriptor to predict the temperature-dependent Gibbs formation energies for perovskites.

In this project, we only focused on 430 perovskites, yet thousands of other materials may be suitable for STAS as redox pairs (quaternary compounds, etc.) and investigating these materials are beyond the scope of the present work. Nevertheless, by evaluating a broad range of candidates, we can establish a database of promising redox pairs for STAS, which provides researchers with new insights into finding feasible solutions for the hydrogen economy. This method can also be used to discover suitable materials for thermochemical applications and makes it possible to predict novel compounds using thermal-controlled solid-state reactions.



## **Chapter 7 Conclusion and Outlook**

### **7.1 Conclusions**

By using structural sampling, DFT-based computational calculations, and machine-learning descriptors, this thesis examined metal-alloyed perovskite oxides/oxy-nitrides (Chapter 4), interactions from formation enthalpies to chemical bonding when oxygen atoms in perovskite oxides are replaced by nitrogen atoms (Chapter 5), and 430 perovskite oxides/oxy-nitrides (Chapter 6) as redox materials for the STAS process. We

have systematically evaluated the thermodynamic performance of these candidates, offering a universal approach for discovering novel active materials for ammonia production. This approach can also be applied to other important chemical synthesis processes.

Ammonia is a crucial chemical for producing daily necessities or manufacturing products applied on an industrial scale, and plays a significant role today. Traditional ammonia production is based on the century-old Haber-Bosch process, which is an energy- and carbon-intensive process. As such, scientists have been searching for high-performance redox materials for ammonia synthesis powered by renewable energy. Chapter 4 explains how we investigated the temperature- and composition-dependent thermodynamics of metal-intermixed perovskite redox pairs. The results show that one A-site-alloyed perovskite redox pair  $\text{Sr}_{0.875}\text{Y}_{0.125}\text{TiO}_3/\text{Sr}_{0.875}\text{Y}_{0.125}\text{TiO}_{2.875}\text{N}_{0.125}$  is activated via cooperative enhancement in contrast to the pristine perovskite  $\text{SrTiO}_3$  and  $\text{YTiO}_3$ . We concluded that not only are these promising redox materials for STAS, but also that metal alloying to change the bonding state of pristine perovskites is a potential method to find additional redox pairs.

Chapter 5 sets out how we systematically studied the formation enthalpies of 430 perovskite oxide/oxy-nitride pairs from lattice strains, tolerance factors, and chemical bonding to explore their thermodynamic stabilities. The results indicate that different VASP relaxation degrees lead to different lattice strains, causing some perovskite oxynitrides to be more thermodynamically stable. We then tried to investigate the relationship between formation enthalpies and tolerance factors; however, there is no obvious connection showing that the tolerance factor is a prerequisite for perovskite oxynitrides to become more stable. Most of the perovskite oxynitrides that become more stable are structures containing transition metal as A-site, so we investigated the bonding interactions of these structures. We found that, if the N-d state overlapped more with the B-site-d state, then the difference in formation enthalpies between the

perovskite oxide and perovskite oxynitride will become larger, and the perovskite oxynitride will become more stable.

With many different schemes that have been proposed for discovering promising active materials for STAS, we were inspired to use high-throughput screening to predict potential redox pairs in large material spaces. Chapter 6 details how we focused on perovskite, combined high-throughput screening and a machine-learning descriptor, and evaluated the performance of the 430 perovskite redox pairs identified in Chapter 5 as potential redox pairs for STAS. Through a series of thermodynamic analyses, the results show that, among the 430 redox pairs,  $\text{BeTiO}_3/\text{BeTiO}_{2.875}\text{N}_{0.125}$  is the only pair that satisfies the requirements for feasibility. In addition, we compared the performance of the descriptor and QHA when they are used to calculate the Gibbs free energies, and the results illustrate that, while there are small underestimations in QHA, the deviation is relatively subtle. Hence, we concluded that using a machine-learning descriptor to calculate the Gibbs formation energy is reliable.

## 7.2 Outlook

Our present work indicates that future research on developing advanced functional materials for energy applications can combine DFT calculations and machine learning to obtain the targeted properties. Previous research has reported that combining high-performance computer science and material science, various properties of materials that are difficult to obtain from experiments can be predicted and simulated before they are synthesised and tested in the laboratory. In addition, due to the rapid development of high-throughput screening and computer science, a new field “materials informatics” has been established. With the assistance of informatics and data science, materials design, selection, development, and discovery are provided with a new method that significantly reduces the time required for and the risk related to the traditional process.

In future research, we will first evaluate the reaction thermodynamics of the 430 oxide/oxy-nitride perovskites when using QHA to calculate their Gibbs formation energies and further reaction energies to compare with the results presented in Chapter 6. A thermodynamic database of perovskite oxides/oxy-nitrides was established in our present work, which enables us to solve the problem of obtaining the temperature-dependent solid-state thermodynamic properties of perovskite, which is difficult to do experimentally. Furthermore, in this thesis, the targeted materials were exclusively perovskites. Yet these comprise only a small portion of available materials, and others that are more complex may be explored as potential active materials for STAS. The current methodology we used in the STAS process can also be applied to other synthetic processes such as water splitting, air separation, and hydrogen production. The findings in this thesis thus pave the way for future work.

## **Appendix: Supporting information of Chapter 4**

### **Can Metal-Intermixing Cooperatively Improve Perovskite as Redox Material for Thermochemical Ammonia Synthesis? A Case Study on (Sr, Y)(Ti, Ru)O<sub>3</sub>**

**Qianli Si<sup>a,\*</sup>, Jack Yang<sup>a,\*</sup>, Jiaxin Fan<sup>a</sup>, Liang Qiao<sup>b</sup>, Sean Li<sup>a,\*</sup>**

*a. Materials and Manufacturing Futures Institute, School of Material Science and Engineering, University of New South Wales, Sydney, NSW 2052, Australia*

*b. School of Physics, University of Electronic Science and Technology of China, Chengdu 610054, China*

## Supporting information

To validate the machine-learned Gibbs free energy descriptor  $G_{\text{SISSO}}^{\delta}$  [63], here, we calculate the temperature-dependent Gibbs free energy for one configuration of  $\text{Sr}_{0.875}\text{Y}_{0.125}\text{TiO}_3$  and  $\text{Sr}_{0.875}\text{Y}_{0.125}\text{TiO}_{2.875}\text{N}_{0.125}$ , respectively, using DFT-based quasiharmonic approximation (QHA) as implemented in PHONOPY, and compared the results obtained with  $G_{\text{SISSO}}^{\delta}$ , which is shown in Fig. S1.

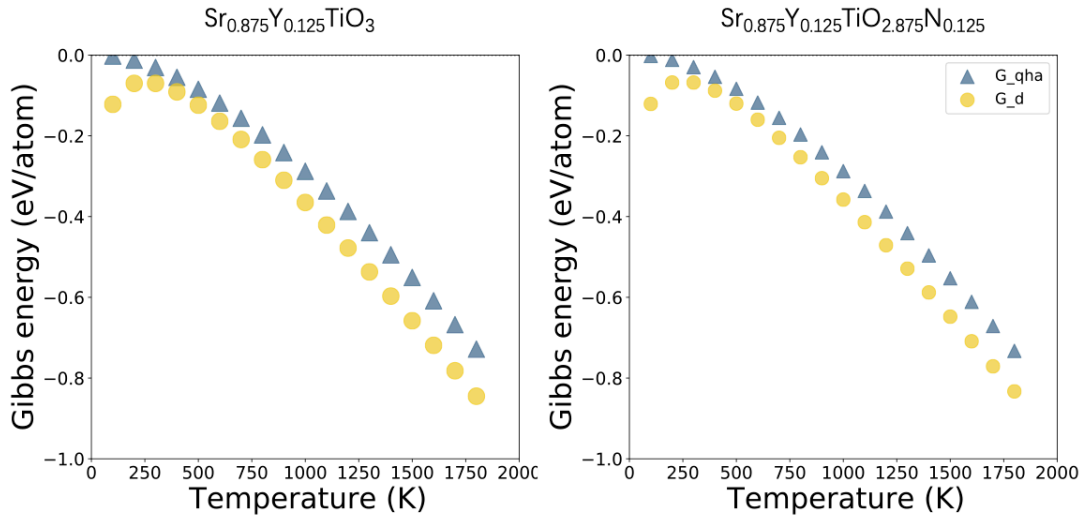


Fig. S1 comparison of the Gibbs energy calculated in QHA and ML descriptor.

As Fig. S1 shows, when temperature increases, the  $G_{\text{QHA}}^{\delta}$  decrease monotonically, but for the  $G_{\text{SISSO}}^{\delta}$ , it first increases from 100 K to 200 K, then decreases as temperature increase further. Through our calculation, we find that  $G_{\text{QHA}}^{\delta} > G_{\text{SISSO}}^{\delta}$  at any temperatures which is in line with Bartel *et al.* work [41]. The deviation becomes bigger from 300 K to 1800 K i.e. as the temperature continues to increase, the accuracy of the machine learned descriptor decreases compared to quasiharmonic approximation. The maximum deviation is about 0.1 eV/atom. Nevertheless, since the underestimation of Gibbs free energies by  $G_{\text{SISSO}}^{\delta}$  is systematic across different temperatures and materials, it should not affect the discussions on the overall trends of material stabilities in the main results.

## Bibliography

1. Jain, A., Y. Shin, and K.A. Persson, *Computational predictions of energy materials using density functional theory*. Nature Reviews Materials, 2016. **1**(1): p. 1-13.
2. Yan, Q., et al., *Solar fuels photoanode materials discovery by integrating high-throughput theory and experiment*. Proceedings of the National Academy of Sciences, 2017. **114**(12): p. 3040-3043.
3. Wenk, H.-R. and A. Bulakh, *Minerals: their constitution and origin*. 2016: Cambridge University Press.
4. Pena, M. and J. Fierro, *Chemical structures and performance of perovskite oxides*. Chemical reviews, 2001. **101**(7): p. 1981-2018.
5. Sachdev, S., *Handbook of magnetism and advanced magnetic materials*. 2006.

6. Petrović, M., V. Chellappan, and S. Ramakrishna, *Perovskites: solar cells & engineering applications - materials and device developments*. Solar Energy, 2015. **122**: p. 678-699.
7. Moszyński, M., et al., *Properties of the new LuAP: Ce scintillator*. Nuclear Instruments and Methods in Physics Research Section A: Accelerators, Spectrometers, Detectors and Associated Equipment, 1997. **385**(1): p. 123-131.
8. Dereń, P., et al., *Laser action in La Al O<sub>3</sub>: Nd<sup>3+</sup> single crystal*. Journal of Applied Physics, 2008. **103**(4): p. 043102.
9. Stranks, S.D. and H.J. Snaith, *Metal-halide perovskites for photovoltaic and light-emitting devices*. Nature nanotechnology, 2015. **10**(5): p. 391-402.
10. Luo, J., et al., *Water photolysis at 12.3% efficiency via perovskite photovoltaics and Earth-abundant catalysts*. Science, 2014. **345**(6204): p. 1593-1596.
11. Yamazoe, N. and Y. Teraoka, *Oxidation catalysis of perovskites--relationships to bulk structure and composition (valency, defect, etc.)*. Catalysis Today, 1990. **8**(2): p. 175-199.
12. Müller, K.A. and H. Burkard, *SrTi O<sub>3</sub>: An intrinsic quantum paraelectric below 4 K*. Physical Review B, 1979. **19**(7): p. 3593.
13. Koonce, C., et al., *Superconducting transition temperatures of semiconducting SrTi O<sub>3</sub>*. Physical Review, 1967. **163**(2): p. 380.
14. Randall, J.J. and R. Ward, *The preparation of some ternary oxides of the platinum metals*, 2. Journal of the American Chemical Society, 1959. **81**(11): p. 2629-2631.
15. Mackenzie, A., et al., *Observation of quantum oscillations in the electrical resistivity of SrRuO<sub>3</sub>*. Physical Review B, 1998. **58**(20): p. R13318.
16. Klein, L., et al., *Transport and magnetization in the badly metallic itinerant ferromagnet*. Journal of Physics: Condensed Matter, 1996. **8**(48): p. 10111.
17. Maeno, Y., et al., *Superconductivity in a layered perovskite without copper*. nature, 1994. **372**(6506): p. 532-534.
18. Gaudon, M., *Out-of-centre distortions around an octahedrally coordinated Ti<sup>4+</sup> in BaTiO<sub>3</sub>*. Polyhedron, 2015. **88**: p. 6-10.
19. Erisman, J.W., et al., *How a century of ammonia synthesis changed the world*. Nature Geoscience, 2008. **1**(10): p. 636-639.
20. Ertl, G., *Reactions at surfaces: From atoms to complexity (Nobel lecture)*. Angewandte Chemie International Edition, 2008. **47**(19): p. 3524-3535.
21. Van der Ham, C.J., M.T. Koper, and D.G. Hetterscheid, *Challenges in reduction of dinitrogen by proton and electron transfer*. Chemical Society Reviews, 2014. **43**(15): p. 5183-5191.

22. Rafiqul, I., et al., *Energy efficiency improvements in ammonia production—perspectives and uncertainties*. Energy, 2005. **30**(13): p. 2487–2504.
23. Luo, Y.-R., *Comprehensive handbook of chemical bond energies*. 2007: CRC press.
24. Jennings, J.R., *Catalytic ammonia synthesis: fundamentals and practice*. 2013: Springer Science & Business Media.
25. Twigg, M.V., *Catalyst handbook*. 2018: Routledge.
26. Gálvez, M., M. Halmann, and A. Steinfeld, *Ammonia production via a two-step Al<sub>2</sub>O<sub>3</sub>/AlN thermochemical cycle. 1. Thermodynamic, environmental, and economic analyses*. Industrial & engineering chemistry research, 2007. **46**(7): p. 2042–2046.
27. Vojvodic, A., et al., *Exploring the limits: A low-pressure, low-temperature Haber - Bosch process*. Chemical Physics Letters, 2014. **598**: p. 108–112.
28. Abild-Pedersen, F., et al., *Scaling properties of adsorption energies for hydrogen-containing molecules on transition-metal surfaces*. Physical review letters, 2007. **99**(1): p. 016105.
29. Michalsky, R., et al., *Departures from the adsorption energy scaling relations for metal carbide catalysts*. The Journal of Physical Chemistry C, 2014. **118**(24): p. 13026–13034.
30. Michalsky, R., et al., *Chemical looping of metal nitride catalysts: low-pressure ammonia synthesis for energy storage*. Chemical Science, 2015. **6**(7): p. 3965–3974.
31. Muhich, C.L., et al., *A review and perspective of efficient hydrogen generation via solar thermal water splitting*. Wiley Interdisciplinary Reviews: Energy and Environment, 2016. **5**(3): p. 261–287.
32. Chueh, W.C., et al., *High-flux solar-driven thermochemical dissociation of CO<sub>2</sub> and H<sub>2</sub>O using nonstoichiometric ceria*. Science, 2010. **330**(6012): p. 1797–1801.
33. McDaniel, A.H., et al., *Sr-and Mn-doped LaAlO<sub>3-δ</sub> for solar thermochemical H<sub>2</sub> and CO production*. Energy & Environmental Science, 2013. **6**(8): p. 2424–2428.
34. Muhich, C.L., et al., *Predicting the solar thermochemical water splitting ability and reaction mechanism of metal oxides: a case study of the hercynite family of water splitting cycles*. Energy & Environmental Science, 2015. **8**(12): p. 3687–3699.
35. Gálvez, M., et al., *Ammonia production via a two-step Al<sub>2</sub>O<sub>3</sub>/AlN thermochemical cycle. 2. Kinetic analysis*. Industrial & engineering chemistry research, 2007. **46**(7): p. 2047–2053.
36. Michalsky, R. and P.H. Pfromm, *Chromium as reactant for solar thermochemical synthesis of ammonia from steam, nitrogen, and*



- biomass at atmospheric pressure*. Solar Energy, 2011. **85**(11): p. 2642–2654.
37. Heidlage, M.G., et al., *Thermochemical synthesis of ammonia and syngas from natural gas at atmospheric pressure*. Industrial & Engineering Chemistry Research, 2017. **56**(47): p. 14014–14024.
  38. Michalsky, R. and P.H. Pfromm, *Thermodynamics of metal reactants for ammonia synthesis from steam, nitrogen and biomass at atmospheric pressure*. AIChE journal, 2012. **58**(10): p. 3203–3213.
  39. Kodama, T., *High-temperature solar chemistry for converting solar heat to chemical fuels*. Progress in energy and combustion science, 2003. **29**(6): p. 567–597.
  40. Raccuglia, P., et al., *Machine-learning-assisted materials discovery using failed experiments*. Nature, 2016. **533**(7601): p. 73–76.
  41. Bartel, C.J., et al., *Physical descriptor for the Gibbs energy of inorganic crystalline solids and temperature-dependent materials chemistry*. Nature communications, 2018. **9**(1): p. 1–10.
  42. Jain, A., et al., *Commentary: The Materials Project: A materials genome approach to accelerating materials innovation*. APL materials, 2013. **1**(1): p. 011002.
  43. Bartel, C.J., et al., *High-Throughput Equilibrium Analysis of Active Materials for Solar Thermochemical Ammonia Synthesis*. ACS Appl Mater Interfaces, 2019. **11**(28): p. 24850–24858.
  44. Greiner, W., L. Neise, and H. Stöcker, *Thermodynamics and statistical mechanics*. 2012: Springer Science & Business Media.
  45. Perrot, P., *A to Z of Thermodynamics*. 1998: Oxford University Press on Demand.
  46. Atkins, P. and L. Jones, *Chemical principles: The quest for insight*. 2007: Macmillan.
  47. Butler, K.T., et al., *Machine learning for molecular and materials science*. Nature, 2018. **559**(7715): p. 547–555.
  48. Medford, A.J., et al., *Extracting knowledge from data through catalysis informatics*. ACS Catalysis, 2018. **8**(8): p. 7403–7429.
  49. Schlexer Lamoureux, P., et al., *Machine learning for computational heterogeneous catalysis*. ChemCatChem, 2019. **11**(16): p. 3581–3601.
  50. Fey, N., *Lost in chemical space? Maps to support organometallic catalysis*. Chemistry Central Journal, 2015. **9**(1): p. 1–10.
  51. Zakutayev, A., et al., *An open experimental database for exploring inorganic materials*. Scientific data, 2018. **5**(1): p. 1–12.
  52. Larsen, A.H., et al., *The atomic simulation environment—a Python library for working with atoms*. Journal of Physics: Condensed Matter, 2017. **29**(27): p. 273002.

53. Jain, A., et al., *Commentary: The Materials Project: A materials genome approach to accelerating materials innovation*. APL Materials, 2013. **1**(1): p. 011002.
54. Pizzi, G., et al., *AiiDA: automated interactive infrastructure and database for computational science*. Computational Materials Science, 2016. **111**: p. 218-230.
55. Sculley, D. *Web-scale k-means clustering*. in *Proceedings of the 19th international conference on World wide web*. 2010.
56. Pakhira, M.K. *A linear time-complexity k-means algorithm using cluster shifting*. in *2014 international conference on computational intelligence and communication networks*. 2014. IEEE.
57. Ringnér, M., *What is principal component analysis?* Nature biotechnology, 2008. **26**(3): p. 303-304.
58. Kohonen, T., *Self-organized formation of topologically correct feature maps*. Biological cybernetics, 1982. **43**(1): p. 59-69.
59. Baum, L.E. and T. Petrie, *Statistical inference for probabilistic functions of finite state Markov chains*. The annals of mathematical statistics, 1966. **37**(6): p. 1554-1563.
60. Günay, M.E. and R. Yildirim, *Analysis of selective CO oxidation over promoted Pt/Al<sub>2</sub>O<sub>3</sub> catalysts using modular neural networks: Combining preparation and operational variables*. Applied Catalysis A: General, 2010. **377**(1-2): p. 174-180.
61. Jacobsen, T., M. Jørgensen, and B. Hammer, *On-the-fly machine learning of atomic potential in density functional theory structure optimization*. Physical review letters, 2018. **120**(2): p. 026102.
62. Curtarolo, S., et al., *The high-throughput highway to computational materials design*. Nature materials, 2013. **12**(3): p. 191-201.
63. Stoffel, R.P., et al., *Ab Initio Thermochemistry of Solid - State Materials*. Angewandte Chemie International Edition, 2010. **49**(31): p. 5242-5266.
64. Hohenberg, P. and W. Kohn, *Inhomogeneous electron gas*. Physical review, 1964. **136**(3B): p. B864.
65. Kohn, W. and L.J. Sham, *Self-consistent equations including exchange and correlation effects*. Physical review, 1965. **140**(4A): p. A1133.
66. Cohen, A.J., P. Mori-Sánchez, and W. Yang, *Challenges for density functional theory*. Chemical reviews, 2012. **112**(1): p. 289-320.
67. Perdew, J.P. and K. Schmidt. *Jacob's ladder of density functional approximations for the exchange-correlation energy*. in *AIP Conference Proceedings*. 2001. American Institute of Physics.

68. von Barth, U. and L. Hedin, *A local exchange-correlation potential for the spin polarized case. i.* Journal of Physics C: Solid State Physics, 1972. **5**(13): p. 1629.
69. Langreth, D.C. and M. Mehl, *Beyond the local-density approximation in calculations of ground-state electronic properties.* Physical Review B, 1983. **28**(4): p. 1809.
70. Becke, A.D., *Density-functional exchange-energy approximation with correct asymptotic behavior.* Physical review A, 1988. **38**(6): p. 3098.
71. Perdew, J.P., et al., *Atoms, molecules, solids, and surfaces: Applications of the generalized gradient approximation for exchange and correlation.* Physical review B, 1992. **46**(11): p. 6671.
72. Becke, A.D., *Density - functional thermochemistry. I. The effect of the exchange - only gradient correction.* The Journal of chemical physics, 1992. **96**(3): p. 2155-2160.
73. Proynov, E., et al., *Determining and extending the domain of exchange and correlation functionals.* International Journal of Quantum Chemistry, 1995. **56**(S29): p. 61-78.
74. Levy, M., *Asymptotic coordinate scaling bound for exchange - correlation energy in density - functional theory.* International Journal of Quantum Chemistry, 1989. **36**(S23): p. 617-619.
75. Kresse, G. and J. Furthmüller, *Efficient iterative schemes for ab initio total-energy calculations using a plane-wave basis set.* Physical review B, 1996. **54**(16): p. 11169.
76. Makov, G. and M. Payne, *Periodic boundary conditions in ab initio calculations.* Physical Review B, 1995. **51**(7): p. 4014.
77. Grimme, S., *Accurate description of van der Waals complexes by density functional theory including empirical corrections.* Journal of computational chemistry, 2004. **25**(12): p. 1463-1473.
78. Schwerdtfeger, P., *The pseudopotential approximation in electronic structure theory.* ChemPhysChem, 2011. **12**(17): p. 3143-3155.
79. Gamble, A., *Ullmann' s Encyclopedia of Industrial Chemistry.* The Charleston Advisor, 2019. **20**(4): p. 46-50.
80. Soloveichik, G., *Electrochemical synthesis of ammonia as a potential alternative to the Haber - Bosch process.* Nature Catalysis, 2019. **2**(5): p. 377-380.
81. Liu, C., et al., *Ambient nitrogen reduction cycle using a hybrid inorganic - biological system.* Proceedings of the National Academy of Sciences, 2017. **114**(25): p. 6450-6455.
82. Peng, P., et al., *Atmospheric pressure ammonia synthesis using non-thermal plasma assisted catalysis.* Plasma Chemistry and Plasma Processing, 2016. **36**(5): p. 1201-1210.

83. Zhu, D., et al., *Photo-illuminated diamond as a solid-state source of solvated electrons in water for nitrogen reduction*. Nature materials, 2013. **12**(9): p. 836–841.
84. Guo, W., et al., *Electrochemical nitrogen fixation and utilization: theories, advanced catalyst materials and system design*. Chemical Society Reviews, 2019. **48**(24): p. 5658–5716.
85. Singh, A.R., et al., *Electrochemical Ammonia Synthesis—The Selectivity Challenge*. ACS Catalysis, 2016. **7**(1): p. 706–709.
86. McEnaney, J.M., et al., *Ammonia synthesis from N<sub>2</sub> and H<sub>2</sub>O using a lithium cycling electrification strategy at atmospheric pressure*. Energy & Environmental Science, 2017. **10**(7): p. 1621–1630.
87. Zeng, L., et al., *Metal oxide redox chemistry for chemical looping processes*. Nature Reviews Chemistry, 2018. **2**(11): p. 349–364.
88. Michalsky, R., et al., *Solar thermochemical production of ammonia from water, air and sunlight: Thermodynamic and economic analyses*. Energy, 2012. **42**(1): p. 251–260.
89. Kirklin, S., B. Meredig, and C. Wolverton, *High - throughput computational screening of new Li - ion battery anode materials*. Advanced Energy Materials, 2013. **3**(2): p. 252–262.
90. Zhang, X., A. Chen, and Z. Zhou, *High-throughput computational screening of layered and two-dimensional materials*. Wiley Interdisciplinary Reviews: Computational Molecular Science, 2019. **9**(1).
91. Bartel, C.J., et al., *High-Throughput Equilibrium Analysis of Active Materials for Solar Thermochemical Ammonia Synthesis*. ACS applied materials & interfaces, 2019. **11**(28): p. 24850–24858.
92. Doh, H., et al., *Influence of Cation Substitutions Based on AB<sub>3</sub> Perovskite Materials, Sr<sub>1-x</sub>Y<sub>x</sub>Ti<sub>1-y</sub>Ru<sub>y</sub>O<sub>3-δ</sub>, on Ammonia Dehydrogenation*. ACS Sustainable Chemistry & Engineering, 2017. **5**(10): p. 9370–9379.
93. Mahadevi, A.S. and G.N. Sastry, *Cooperativity in noncovalent interactions*. Chemical reviews, 2016. **116**(5): p. 2775–2825.
94. Zhu, X., et al., *Perovskites as geo-inspired oxygen storage materials for chemical looping and three-way catalysis: a perspective*. Acs Catal., 2018. **8**(9): p. 8213.
95. Yang, J., et al., *Correlating the Composition-Dependent Structural and Electronic Dynamics of Inorganic Mixed Halide Perovskites*. Chemistry of Materials, 2020. **32**(6): p. 2470–2481.
96. Perdew, J.P., K. Burke, and M. Ernzerhof, *Generalized gradient approximation made simple*. Physical review letters, 1996. **77**(18): p. 3865.

97. Kresse, G. and D. Joubert, *From ultrasoft pseudopotentials to the projector augmented-wave method*. Physical review b, 1999. **59**(3): p. 1758.
98. Monkhorst, H. J. and J. D. Pack, *Special points for Brillouin-zone integrations*. Physical review B, 1976. **13**(12): p. 5188.
99. Bale, C.W., et al., *FactSage thermochemical software and databases*. Calphad, 2002. **26**(2): p. 189–228.
100. Yang, J. and M.P. Waller, *A Systematic Approach to Identify Cooperatively Bound Homotrimers*. The Journal of Physical Chemistry A, 2013. **117**(1): p. 174–182.
101. Zunger, A., *Inverse design in search of materials with target functionalities*. Nature Reviews Chemistry, 2018. **2**(4): p. 1–16.
102. Bartel, C.J., et al., *The role of decomposition reactions in assessing first-principles predictions of solid stability*. npj Computational Materials, 2019. **5**(1): p. 1–9.
103. Zhou, J.J., O. Hellman, and M. Bernardi, *Electron-Phonon Scattering in the Presence of Soft Modes and Electron Mobility in SrTiO<sub>3</sub> Perovskite from First Principles*. Phys Rev Lett, 2018. **121**(22): p. 226603.
104. Knoop, F., et al., *Anharmonicity measure for materials*. Physical Review Materials, 2020. **4**(8).
105. Tadano, T. and S. Tsuneyuki, *Ab initio prediction of structural phase-transition temperature of SrTiO<sub>3</sub> from finite-temperature phonon calculation*. Journal of the Ceramic Society of Japan, 2019. **127**(6): p. 404–408.
106. Colville, A. and S. Geller, *The crystal structure of brownmillerite, Ca<sub>2</sub>FeAlO<sub>5</sub>*. Acta Crystallographica Section B: Structural Crystallography and Crystal Chemistry, 1971. **27**(12): p. 2311–2315.
107. Sharma, I.B. and D. Singh, *Solid state chemistry of Ruddlesden-Popper type complex oxides*. Bulletin of Materials Science, 1998. **21**(5): p. 363–374.
108. Marchand, R., F. Pors, and Y. Laurent, *Préparation et caractérisation de nouveaux oxynitrides à structure perovskite*. Revue internationale des hautes températures et des réfractaires, 1986. **23**(1): p. 11–15.
109. Ebbinghaus, S.G., et al., *Perovskite-related oxynitrides - recent developments in synthesis, characterisation and investigations of physical properties*. Progress in Solid State Chemistry, 2009. **37**(2–3): p. 173–205.
110. Jansen, M. and H.-P. Letschert, *Inorganic yellow-red pigments without toxic metals*. Nature, 2000. **404**(6781): p. 980–982.

111. Kasahara, A., et al., *Photoreactions on LaTiO<sub>2</sub>N under visible light irradiation*. The Journal of Physical Chemistry A, 2002. **106**(29): p. 6750–6753.
112. Zhang, X., A. Chen, and Z. Zhou, *High - throughput computational screening of layered and two - dimensional materials*. Wiley Interdisciplinary Reviews: Computational Molecular Science, 2019. **9**(1): p. e1385.
113. Jain, A., et al., *A high-throughput infrastructure for density functional theory calculations*. Computational Materials Science, 2011. **50**(8): p. 2295–2310.
114. Vieten, J., et al., *Materials design of perovskite solid solutions for thermochemical applications*. Energy & Environmental Science, 2019. **12**(4): p. 1369–1384.
115. Wang, X., et al., *Bonding nature and optical contrast of  $\text{TiTe}_2/\text{Sb}_2\text{Te}_3$  phase-change heterostructure*. arXiv preprint arXiv:2103.13583, 2021.
116. Michalsky, R. and A. Steinfeld, *Computational screening of perovskite redox materials for solar thermochemical ammonia synthesis from N<sub>2</sub> and H<sub>2</sub>O*. Catalysis Today, 2017. **286**: p. 124–130.
117. Geffroy, P.-M., et al., *Rational selection of MIEC materials in energy production processes*. Chemical engineering science, 2013. **87**: p. 408–433.
118. Ezbiri, M., et al., *Design principles of perovskites for thermochemical oxygen separation*. ChemSusChem, 2015. **8**(11): p. 1966.
119. Demont, A., S. Abanades, and E. Beche, *Investigation of perovskite structures as oxygen-exchange redox materials for hydrogen production from thermochemical two-step water-splitting cycles*. The Journal of Physical Chemistry C, 2014. **118**(24): p. 12682–12692.